Charge transport and mechanical property study of high mobility conjugated polymers

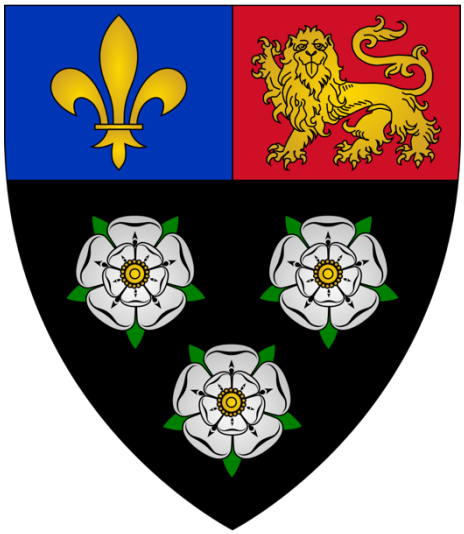

Mingfei Xiao

King's College Cavendish Laboratory

University of Cambridge

This dissertation is submitted for the degree of

Doctor of Philosophy

September 2019

Declaration

This thesis is the result of my own work and includes nothing which is the outcome of work done in collaboration except as declared in the preface and specified in the text.

It is not substantially the same as any that I have submitted, or, is being concurrently submitted for a degree or diploma or other qualification at the University of Cambridge or any other University or similar institution except as declared in the Preface and specified in the text. I further state that no substantial part of my dissertation has already been submitted, or, is being concurrently submitted for any such degree, diploma or other qualification at the University of Cambridge or any other University or similar institution except as declared in the Preface and specified in the text.

It does not exceed the prescribed word limit for the relevant Degree Committee. The number of words in this thesis does not exceed 60,000.

Collaborators which have made specific contributions to this work include Professor Guoming Liu at Institute of Chemistry, Chinese Academy of Science, Yutian Wu at the Cavendish Laboratory, University of Cambridge, Dr. Sarah Rogers and Dr. Najet Mahmoudi at ISIS Facility, STFC, Rutherford Appleton Lab (small-angle neutron scattering (SANS) and data analysis), Professor Giovanni Costantini, Dr. Luís M. A. Perdigão, Dr. Alex Luci of Department of Chemistry, University of Warwick (high-resolution scanning tunneling microscopy (STM) measurements and data analysis), Dr. Boseok Kang, Seon Baek Lee of Department of Chemical Engineering, Pohang University of Science and Technology and Professor Chris McNeill, Dr. Xuechen Jiao of Department of Materials Science and Engineering, Monash University (Grazing-Incidence Wide-Angle X-ray Scattering (GIWAXS)), Dr. Boseok Kang, Seon Baek Lee of Department of Chemical Engineering, Pohang Univeristy of Science and Technology (Near Edge X-Ray Absorption Fine Structure (NEXAFS) spectroscopy), Dr. Tao Zhang of Chair of Functional Molecular Materials Center for Advancing Electronics Dresden, Technische Universität Dresden (High-resolution transmission electron microscopy (HRTEM) and data analysis), Dr. Wan Yue, Cameron Jellet, Ada Onwubiko, Dr. Hung-Yang Chen of Department of Chemistry, Imperial College London, Dr. Hu Chen, Dr. Balaji Purushothaman, Dr. Rawad Hallani, Maryam Alsufyani at KSC, King Abdullah University of Science and Technology, and Hailiang Liao of School of Engineering, University of Sun Yat-Sen (conjugated polymer synthesis and characterisation), Dr. Deepak Venkateshvaran, Dr. Leszek Spalek, Dimitrios Simatos at the Cavendish Laboratory, Univeristy of Cambridge (helped with devices fabrication and devices measurements), Shijie Zhan at the Department of Engineering, the University of Cambridge ((Indium Tin Oxide) ITO sputter-coating), Dr. Sanyang Han, Qifei Gu, Dr. Sachin Dev Verma at the Cavendish Laboratory, University of Cambridge (helped with photophysics experiments), Dr. Aditya Sadhanala, Dr. Mojtaba Abdi Jalebi at the Cavendish Laboratory, University of Cambridge (photothermal deflection spectroscopy (PDS) measurements), Lianglun Lai at the Cavendish Laboratory, University of Cambridge (helped with the charge accumulation spectroscopy (CAS) measurements), Hailiang Liao of School of

Engineering, University of Sun Yat-Sen (Atomic Force Microscopy (AFM) measurements). Wherever these measurements and calculations are presented, they are acknowledged in the corresponding figure captions.

Mingfei Xiao

September 2019

Acknowledgements

First, I would like to thank Professor Henning Sirringhaus for offering me the precious chance to study at the world-renowned Cavendish Laboratory five years ago. I genuinely believe this precious opportunity is a tremendous gift for my life and future career. During these five years, I received lots of help from my supervisor, both in terms of academic supervision and support in everyday lives. Support from Henning helps me regain courage and interest in science during some toughest times. I hold the highest respect and appreciation for all the support and help received.

Then I want to thank my parents and all my family members for your endless trust and love. Paramount thanks for my parents for their endless love and supports. I am so lucky to have such understanding parents who would always support me in doing the right things. Also, thank other family members for all the help and support in these five years. Support and help from family members are some of the most significant sources of strength during my Ph.D., which I would hold huge appreciation and always be grateful in my life.

I would also like to thank Tsinghua University, the Chinese Scholarship Council, and Cambridge Trust to support the application and finally offered me the joint scholarship, which supported me financially for all these years. Cambridge Philosophy Society and the King's College, University of Cambridge also offered me additional funding, which I would acknowledge it here as well. I want to thank King's College for all the support during these five years. Special thanks would go to Dr. Bert Vaux (my college tutor) and Mrs. Caroline White for all the lovely and timely help. It is my honor to be selected into King's College, University of Cambridge five years ago, and it would be one of the best parts in my memory of seeing the King's Chapel every morning in the sunshine during my third year's college accommodation at King's Parade 20-21.

I want to thank all the friends, colleagues, and collaborators mentioned in the declaration, who helped to complete this exciting, however complicated work. Some colleagues and collaborators showed me supports and trust during very harsh periods or offered me very precious materials which I heartly appreciate it. Here I would like to thank Sir. Richard Friend, Professor. Iain McCulloch, Dr. Deepak Venkateshvaran, Dr. Mark Nikolka, Dr. Leszek Spalek, Dimitrios Simatos, Dr. Hu Chen, and Cameron Jellet.

Finally, I would like to thank the supporting staff, Dr. Radoslav Chakalov, Roger Beadle, Steve Haws, Thomas Sharp, etc., for their dedicated attitude, innovative approach, and fantastic crafting skills of maintaining our lab. Also, I would appreciate all the lovely memories with our kindest staff in the mechanical and electronics workshop at the Cavendish Laboratory. Your excellent craftsmanship turns my alignment setup into real.

Table of Contents

Contents

1. Introduction

In 1977 three scientists from the University of Pennsylvania, Alan Heeger, Alan MacDiarmid, and Hideki Shirakawa published their groundbreaking results of high conductivity above 100 $\Omega^{-1}cm^{-1}$ measured from doped polyacetylene film[1]. Through introducing controlled amounts of dopants like iodine, electrical conductivity could be modulated by more than five orders of magnitude compared with the pristine film; also, an insulator to metal transformation at certain doping concentration was observed by various techniques. This was a huge breakthrough in the field of polymer science and won them the Nobel Prize in Chemistry later on[2]. Their discovery not only changed people's opinion regarding the electronic property of polymers but also initiated the research of electronic and optoelectronic properties of these conjugated systems, which later on enabled various application markets.

Conjugated polymers are carbon-based van der Waals solids with inherent flexibility. By functionalizing polymer backbones with solubilizing side chains, these soft solids behave as appealing candidates for low-temperature, large-area printable[3], flexible[4], and even stretchable[5][6] electronic applications, hitherto not achievable through traditional inorganic semiconductor technology. For example, organic field-effect transistor (OFET) technology[7] based on these conjugated materials has been commercialized by spin-off companies like Plastic Logic/FlexEnable in certain niche applications which do not have demanding switching speeds or drive requirements, including backplanes of certain Liquid Crystal Display (LCD), simple logic circuits and organic sensors/sensor arrays [8–11]. More importantly, due to better biocompatibility compared with inorganic counterparts, plastic implants integrating OFETs such as amplifiers and sensors show massive potential for in-vivo bioelectronics applications.

Great efforts have been made to improve the performance and stability of OFETs over the past years. The field-effect mobility μ_{FET} informs how fast charge moves within OFETs under applied lateral electric field, and has long been regarded as the figure-of-merit parameter of device performance. Structural disorder, weak electronic

coupling, and significant charge-phonon interaction limit μ_{FET} of polymer-based OFETs, leading to inferior performance of OFETs compared with inorganic FETs like monocrystalline[12] or polycrystalline silicon[13] devices. However, several orders of magnitude improvements have happened in the past three decades, and now μ_{FET} in state-of-the-art conjugated polymer devices have gone beyond the value of amorphous silicon (a-Si)[14–17]. Besides μ_{FET}, industrial applications also impose strict requirements on the stability of OFETs. In this respect, the loosely-bonded and disordered nature of conjugated polymers is not favorable as well, since nanovoids[18] within these materials are prone to degradation caused by the infiltration of environmental species, which act as trap states within the bandgap. Recently, various strategies have been developed to improve devices' stability to a remarkable level. Two outstanding approaches would be addressed here, namely, molecular additive and composite dielectric strategy. For example, certain molecular additives prove to be very efficient to passivate water-related traps and thus increase the threshold voltage stability of OFETs. Combining with a state-of-the-art, near amorphous donor-acceptor copolymer indacenodithiophene-co-benzothiadiazole (IDT-BT)[19], p-channel OFETs measured in the nitrogen atmosphere demonstrate impressive operational stability and uniformity to a level approaching the requirement for industrial applications[20]. For another approach which focuses on optimization of device's architecture and encapsulation, a composite (atomic layer deposition deposited) dielectric strategy has proven to be successful in reducing operational voltage, blocking ingress of environmental species, and compensating threshold voltage shift during continuous stress at the same time, rendering devices with superior environmental and operational stability, even surpassing the level of certain commercial inorganic thin film transistor (TFT) technologies[21]. With the joint efforts of further developed material systems[22] and rapid improvement of device fabrication, encapsulation, and integration, OFET technology might have a chance to satisfy more mainstream markets such as current-driven displays in the foreseeable future, which impose a more demanding requirement on device performance and stability[23].

In terms of the development of new materials, a series of semicrystalline polythiophene derivatives featuring significant π–π stacking and long-range order has been developed in the last three decades. Successful demonstrations of poly (3-hexylthiophene) (P3HT)[24], poly(3,3-dialkyl-quaterthiophene) (PQT)[25],[26] and poly (2,5-bis (3-alkylthiophen-2-yl) thieno-[3,2-b]thiophene) (PBTTT)[27] achieved moderate mobilities approaching or above 0.1 $cm^2V^{-1}s^{-1}$. Crystalline and amorphous regions generally coexist in thin films of conjugated polymers, bringing in significant disorder at the energetic landscape and bottlenecking charge transport property of materials. For instance, in Figure 1-1, a scanning tunneling microscope(STM) image for semi-crystalline polymer poly(3-dodecylthiophene-2,5-diyl) (P3DDT) is demonstrated, showing the coexistence of ordered and disordered regions within the scanned region[28]. Consequently, by intuition one would expect that high crystallinity is favorable for high mobility, which holds true for inorganic or small molecular organic semiconductors. The design strategy chasing high crystallinity hence has been established with PBTTT as the most convincing validation, showing the size of a crystalline domain above 100 nm with optimized processing and annealing protocols[27]. However, this idea has been challenged recently by the observation of high mobility in polymer films with very low crystallinity[29], which brings up a vivid debate regarding the design criteria for high-performance polymeric semiconductors. For example, it has been argued that short-range order[30][31] is enough to guarantee fast macroscopic charge transport in certain state-of-the-art systems[29][32]. To solve this long-standing problem, Salleo *et al.* did a systematic study on the relationship between disorder, aggregation and charge transport in conjugated polymers, and they found that the key to high mobility is not high crystallinity but high tolerance to disorder[33]. In other words, a rigid polymer backbone is beneficial for efficient charge transport. Following this new strategy, more complex donor-acceptor (D-A) copolymers with low torsional backbones [29][34][35], ideal in-plane orientation [36] and long persistence length[37][38] have exhibited $\mu_{FET} > 1$ $cm^2V^{-1}s^{-1}$ in several cases [8], including polymers with nearly amorphous structure[19].

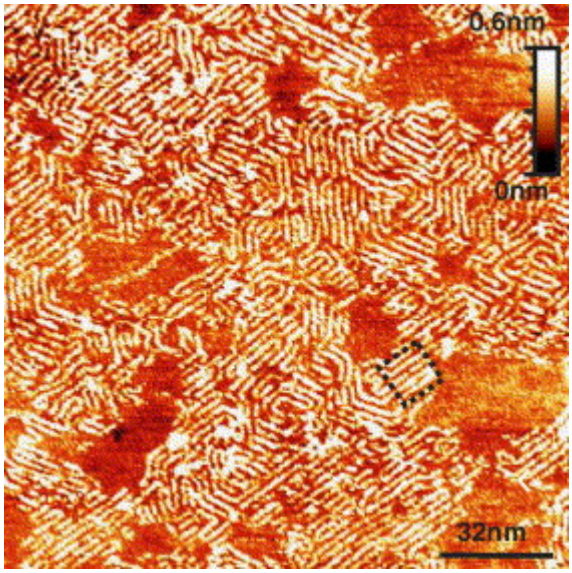

Figure 1-1 159.1 nm × 159.1 nm (pitch = 0.7 nm, VS = 1 V, It = 0.15 nA) STM image of a P3DDT film with a ca. 75% surface coverage on HOPG. The dotted square indicates a 13 nm × 13 nm mono-domain. Image and caption adapted from R. Payerne[28].

Similar to the situation in inorganic integrated circuits[39], more complex logic building blocks such as inverters rather than isolated OFETs are essential to achieve multi-functional logic. In this respect, complementary architectures integrating both p- and n-channel OFETs are highly desirable and demonstrate advantages such as less power consumption and improved noise margins over unipolar architectures. However, the development of n-channel conjugated polymers with both high μ_{FET} and acceptable environmental/operational stability still lags behind the development of high-performance p-channel conjugated polymers[40]. Compared to p-channel materials, there is a relatively limited amount of electron-withdrawing building blocks available to make n-channel polymers[41]. More importantly, most n-channel polymers with shallow LUMO levels tend to form radical anions with high reducing power during positive device gating. The infiltrated environment species in the channel can be easily reduced by these anions, resulting in electron trapping[42], which weakens or inhibits stable electron transport, and leads to degradation of OFETs during continuous stress or long-term air-exposure. Thus it would be highly desirable if kinetic barriers could be formed against diffusion of environmental species into the devices[43–45] and if mechanisms could be introduced to mitigate and passivate their damaging effects[20,46–48]. From the energetic level point of view, theoretical calculations and empirical results

both demonstrate the requirement for an electron affinity(EA) of conjugated polymers above 4 eV to achieve stable electron transport within OFETs[40]. For example, the widely investigated high mobility n-channel material P(NDI2OD-T2)[49] has an EA of 3.9 eV, and degradation of top-gate bottom-contact (TGBC) P(NDI2OD-T2) OFETs in the air was studied utilising the charge accumulation spectroscopy(CAS) technique developed within the Cavendish Laboratory[50]. Redox reaction between charged polymers and environmental species penetrated into the device's channel was found to be responsible for the device degradation.[50] Aiming for more stable n-channel polymers might hence require exceptionally innovative material design able to achieve even higher electron affinity than P(NDI2OD-T2) and better environmental and operational stability.

In terms of the improvement of device fabrication, optimizing processing conditions is essential to realize ideal morphologies of polymer films, since the structure-property relationship study is arguably one of the most important topics of OFETs research[33][51][52]. It is widely accepted that charge transport property of devices is strongly related to microstructures of polymer layers, especially the regions close to dielectric interfaces where charge transport takes place[53]. Hence the appropriate choice of solvents[54][55], improved film deposition techniques[56], and optimized annealing strategies[44], etc. are important to achieve ideal morphologies and reduced structural and energetic disorder (especially true for certain semicrystalline polymers) for polymer films[57]. Fast-drying processes like spin-coating do not always lead to optimum microstructural order, which in return limits the exploitation of the full potential of these polymeric semiconductors. Therefore, more controlled film deposition techniques specially designed for conjugated polymers need to be developed, with meniscus-guided, directionally aligned deposition techniques standing out as promising approaches. These include several methods like zone casting, solution shearing, slot-die coating, dip coating, etc.[56][57], which not only allow the improvement of the charge transport property to a level that it can outperform certain inorganic semiconductors like amorphous silicon[8], but also demonstrate additional, while crucial

advantages such as improvement of high-frequency operation and reduction of devices' performance dispersion for large-area circuits[55][57].

Emerging applications such as artificial skin[58–60] require the deformability of OFETs (as building blocks) as never before. This demands the development of each stretchable component within devices, including stretchable dielectrics[61][62], semiconductors[5], and conductors (electrodes)[63]. Conjugated polymers may satisfy the need as devices' active layers due to their favorable mechanical properties. However, while most conjugated polymers demonstrate flexibility owing to the weak van der Waals bonding, good stretchability is a more demanding requirement. Conjugated polymers, especially the ones featuring long-range order and high crystallinity, tend to crack under strain. For example, in the case of highly crystalline polymer PBTTT, the crack onset strain of thin films is found to be less than 10%[64], while another typical semi-crystalline polymer DPPTT shows a similar crack formation threshold[65]. Based on these observations, it is deemed that long-range order within highly crystalline polymers generally causes the price of brittleness. Moreover, except for specific state-of-the-art near-amorphous polymers[66], it is rare for pure conjugated polymers to retain moderate mobility (comparable to amorphous silicon) under significant strain (>20 %). Hence certain strategies must be developed to improve the mechanical properties of conjugated polymers further, or more specifically, to introduce additional strain-dissipation mechanisms. Up to now, successful methods include molecular tailoring approaches such as incorporating specially designed moieties into backbones[67], and material engineering methods like encapsulating conjugated polymer networks inside an elastomer matrix[5] (illustrated in Figure 1-2). These strategies succeed in reducing the modulus of materials and hence preserve the mechanical integrity and electrical performance under stains, showing the potential of conjugated polymers for future skin-inspired electronics[68][69] and generating significant traction into the investigation of their mechanical properties.

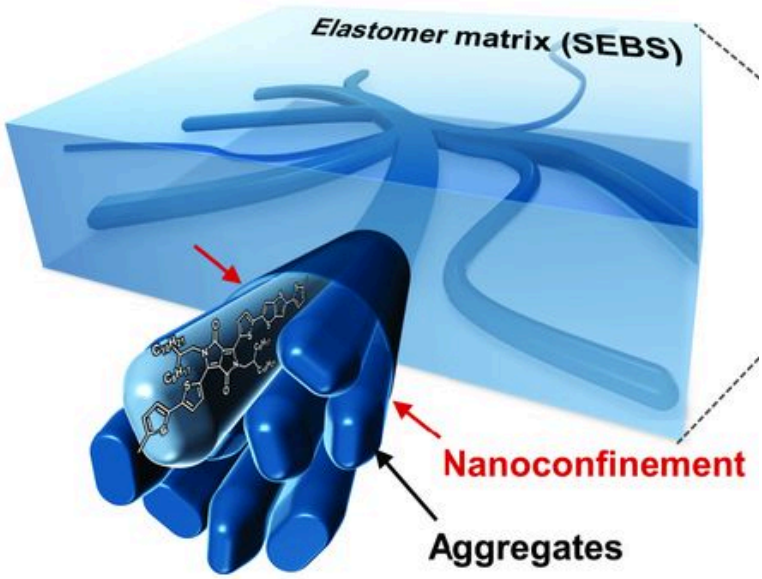

Figure 1-2 schematic of the embedded conjugated polymers networks inside an elastomer matrix. Image and caption adapted from J. Xu. [5]

Compared with the extensive efforts made in terms of polymer synthesis and device optimization, much fewer researches have focused on the mechanical property study of these conjugated polymers. Researches linking polymers' mechanical and electronic properties emerge recently, correlating these properties to their common microstructure origins[70]. Traditional characterization techniques in polymer physics, such as nanoindentation[71], tensile measurements[72], rheometry measurements[73], and dynamic mechanical analysis (DMA)[74], are hence applied to investigate mechanical properties of conjugated polymers. In the future, a comprehensive study of critical mechanical parameters on an extensive library of reprehensive materials would provide a novel angle into the structure-property relationship. New insights gained from mechanical measurements would hopefully provide updated design guidelines for the next-generation conjugated polymers targeting various promising applications.

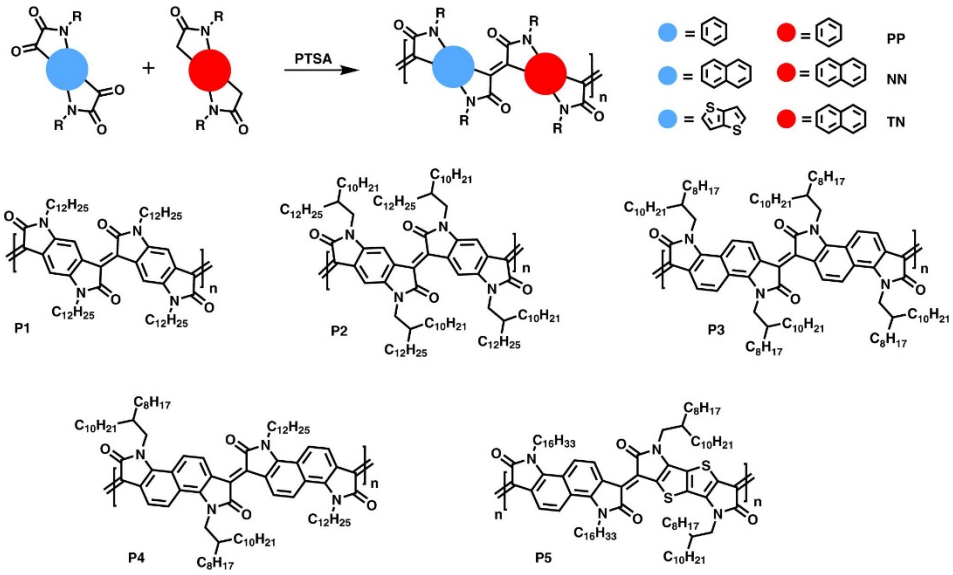

Figure 1-3 The generic scheme for the preparation of rigid polymers synthesised via aldol polymerisation. The polymers are made from bis-isatin and bis-oxindole monomers. The aldol condensation polymers reported here are P1, P2, P3, P4 and P5. The polymer repeat units are described as PP for phenyl homopolymer, NN for naphthalene homopolymer and TN for thieno[3,2-b]thiophene and naphthalene copolymer. R is a solubilising alkyl chain. Image and caption adapted from A. Onwubiko.[75]

In this work, I investigated a newly synthesized, unusual family of fused-core electron-deficient conjugated polymers, exploring their applications in air-stable n-channel charge transport within top-gate, bottom-contact OFETs. These materials are synthesized via an aldol condensation reaction between bis-isatin and bis-oxindole, with all the fused ring structures along backbones linked together purely by double bonds, which largely suppresses the rotational freedom at these linkages and reduces torsional disorder (Figure 1-3). Besides, since only electron-accepting groups are incorporated into the backbone, this family of materials comes with significantly deeper LUMO levels (≥4.2eV) compared with other more traditional conjugated polymers, implying the potential for air-stable electron transport.[75] To optimize the fabrication process of OFETs based on this newly developed material system, a home-made solution shearing setup (shown in Figure 1-4 **错误!未找到引用源。**) was used to deliver semiconducting film deposition in a more controlled manner, and potentially to introduce favorable crystallinity and microstructural anisotropy desirable for directional charge transport.

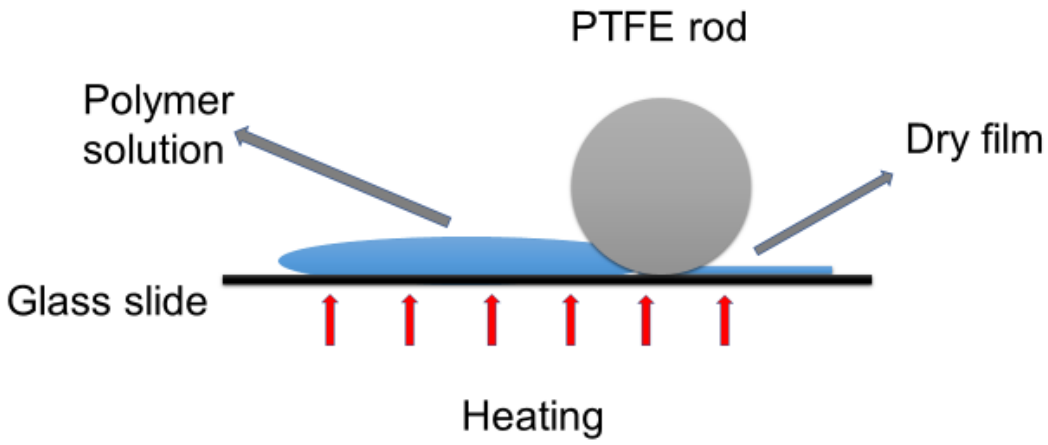

Figure 1-4 Sketch of home-made solution shearing setup used in this work.

Due to their unique double bonds-fused backbone structure, it is highly likely that these polymers would demonstrate a higher level of rigidity compared with more traditional single bonds-linked conjugated polymers. Therefore, two techniques are used to characterise the backbone rigidity of these fused polymers. From small-angle neutron scattering (SANS) experiments, the rigid-rod nature of isolated chains (dissolved within hot tetradeutero-1,2-dichlorobenzene solutions) is confirmed from the scattering patterns. Moreover, the glass transition temperature (T_g) measured from the DMA gives quantitative information about the rigidity of the polymer backbone. Furthermore, with the DMA technique, a range of high mobility and highly luminescent polymers is investigated and their mechanical and electronic/optoelectronic properties are correlated, from which empirical rules are established for better understanding and designing of next-generation conjugated polymers targeting different applications.

The outline of this thesis is presented below.

Chapter 1 provides a general background of organic semiconductors and organic electronics.

Chapter 2 provides an overview of the electronic structure and the charge transport physics of conjugated polymers within an OFET. Fundamental device physics, including the selection of appropriate dielectric, is analyzed.

Chapter 3 introduces the conjugated polymers and dielectrics investigated in this work, in addition to the device fabrication procedures and experimental

characterization techniques. Advanced UV-vis-NIR absorption, X-ray diffraction, and neutron scattering techniques relevant to this work are introduced as well.

Chapter 4 describes the characterization of a range of fused polymers. A detailed structure-property relationship study is performed to understand the influence of side-chain design, backbone extension, backbone flatness, etc., on the microstructure, energetic disorder, and charge transport behavior of these materials.

Chapter 5 explores the alignment of a fused electron-deficient polymer by a solution-shearing process and investigates the influence of the shearing process on crystallinity, charge transport, and optical anisotropy.

Chapter 6 explores the dynamic mechanical analysis technique, which proves to be a potent technique to understand charge transport and photophysical properties of certain conjugated polymers.

Chapter 7 presents the outlook about the development strategy to achieve high-performance, air-stable n-channel OFETs, and about the promising applications of the DMA technique for the material screening of conjugated polymers.

2. Theoretical background

2.1 Electronic structure of organic semiconductors

As their names indicate, organic semiconductors (OSCs) are carbon-based materials showing the semiconducting property. Depends on molecular structure, OSCs could be classified into small molecules and conjugated polymers. While small molecules have unified molecular weight, well-defined molecular structure, and could be processed into highly ordered, even single crystal structures with optimised recipes[76], conjugated polymers generally come with different degrees of polydispersity, and tend to be much more disordered in nature.[77] However, due to the solubilizing side chains attached to polymer backbones, conjugated polymers are easier to be solution-processed into large-area, uniform films, which is one of the key advantages of organic electronics.

Compared with saturated polymers, which are insulators in nature, within OSCs there are unsaturated double bonds, which is the key factor related to their semiconducting property. In other words, the semiconducting property of conjugated polymers originate from the conjugation structure, namely alternating single and double bonds within molecules as a result of the sp^2 hybridization of carbon atoms.

For sp^2 hybridization, one 2s orbital hybridizes with two 2p orbitals to form three co-planar sp^2 orbitals. These sp^2 orbitals overlap with each other or with other atomic orbitals to form the backbone of molecules. While the unhybridised p_z orbitals stay perpendicular to the sp^2 orbital (backbone) plane, the overlapping of neighboring p_z orbitals forms delocalised molecular orbitals deciding the material's semiconducting property. More specifically, when two p_z orbitals interact with the same phase, a lower energy, bonding π orbital is formed; when they interact out of phase, a higher energy, antibonding π^* orbital is formed. The gap between the π and the π^* orbitals is the material's bandgap. The simplest example to show the sp^2 hybridization and the

formation of atomic/molecular bonds in conjugated system is the electronic structure of the ethylene molecule, which is shown in Figure 2-1.

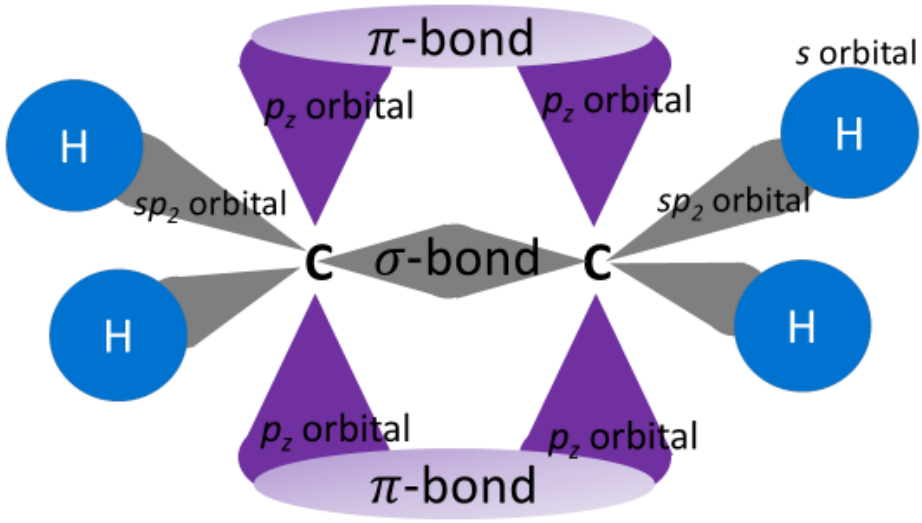

Figure 2-1 electronic structure of ethane

For the polyacetylene system (illustrated in Figure 2-2) with more extended backbone, molecular orbital (MO) theory, which is based on the linear combination of atomic orbitals (LCAO), needs to be used to accurately predict the shape and energy of all the possible molecular orbitals. According to the MO theory, increasing the conjugation to infinity would shrink the energy gap between neighboring states until quasi-continuous bands are formed, and the bandgap would vanish as well, turning polyacetylene into a conductor. However, with a similar mechanism of the Peierls' theorem of one-dimensional metals, an equivalent bond length along the polymer backbone is not the most energetically stable state, hence the self-dimerisation (i.e., alternating single-double bonds along polymer backbones) would naturally happen to lower the energy of the molecular orbitals further. From the energetic point of view, this would open up a bandgap around the Fermi level, turning polyacetylene into a semiconductor. Besides, in reality, microstructural defects and disorder are inevitable along polymer backbones, breaking the whole chains into conjugated segments with

various lengths and frontier orbital energy levels, which are reflected from the energetic disorder such as tails states around the band edges.

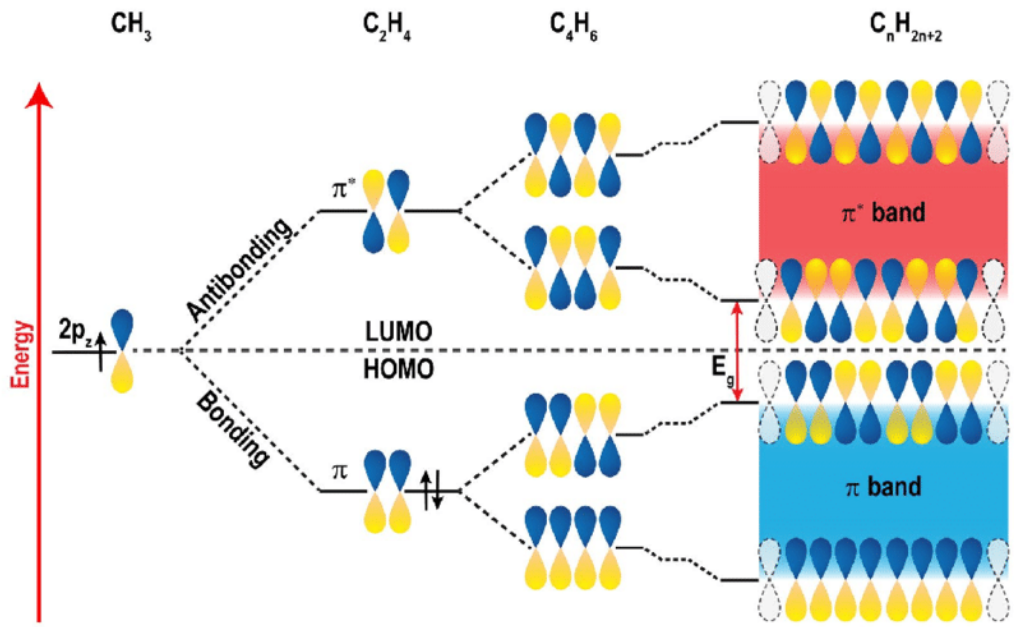

Figure 2-2 Energy diagram of polyacetylene. Image and caption adapted from K. Wijeratne[78].

Different from isotropic single-crystalline inorganic semiconductors such as silicon, another unique feature of conjugated polymers is the structural and electronic anisotropy caused by the elongated backbones[79]. As discussed above, the delocalised π orbital provides an efficient charge transport pathway along the polymer backbone. However, the macroscopic charge transport process is always bottlenecked by the time-consuming and energy-activated inter-chain hopping process. Hence it would be ideal if the directional chain alignment technique could be employed to explore the efficient intra-chain charge transport pathway fully while reducing the inter-chain hopping steps as much as possible. Toward this end, various meniscus-guided coating techniques[56] have been developed to align polymer chains by the shearing force applied. Sometimes additional benefits such as improved microstructural order or modified lattice strains[80] could also be induced, improving charge transport property further.

2.2 Neutral excited states

As shown in Figure 2-2, when a conjugated polymer is at its neutral state, all the states underneath the highest occupied molecular orbital (HOMO) are filled with opposite spins, while all the states above the lowest unoccupied molecular orbital (LUMO) are empty. The energy gap between the HOMO and the LUMO decides the bandgap of the conjugated polymer. Under excitation, such as lighting the polymer with photon energy larger than the bandgap, an electron would be promoted from the HOMO to the LUMO, thus leaves a hole in the HOMO level. Such an electron-hole pair is termed as an exciton, an electrically neutral quasiparticle. Within OSCs, the relative permittivity (ε_r) is much lower than inorganic semiconductors ($\varepsilon_r \approx 3$ for OSCs, while $\varepsilon_r = 11.68$ for silicon). This means that over distance electric fields decay much slower within organic semiconductors compared with inorganic semiconductors. Hence unlike excitons in inorganic semiconductors, within organic semiconductors, excitons are more tightly bonded together by the electrostatic forces with a smaller radius(~10 Å) and higher binding energy(~0.5 eV)[81] compared with the situations for inorganic semiconductors (exciton radius ~100 Å, exciton binding energy ~10 meV), and this type of tightly bonded exciton is known as the Frenkel exciton (Figure 2-3 right)[82–86], different from the Wannier exciton (Figure 2-3 left) typically observed within inorganic semiconductors.

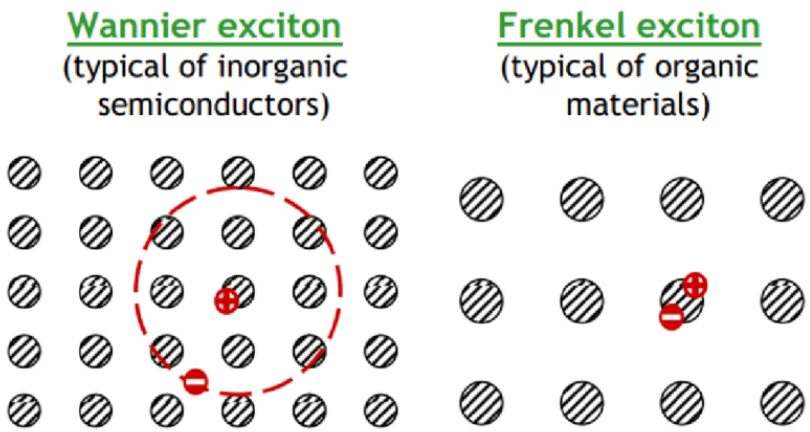

Figure 2-3 Frenkel exciton and Wannier exciton. Image and caption adapted from V. Bulovic[83].

Except for the excitation and recombination processes, vibrational relaxation is also a key factor deciding the dynamics between the ground and the excited states. More specifically, within an electronic state of a conjugated polymer, there exist various vibrational levels that are related to different geometries of individual chromophores. During light absorption and emission, transitions happen between vibrational levels within an electronic state or between two electronic states. The Frank-Condon principle[87] is widely used to calculate the intensity of each possible vibrational transition. In general, the intensity of the vibrational transition could be calculated based on the degree of the wave function overlapping between the initial and the terminate states involved. However, the unique feature about the fluorescence behavior within OSCs is that no matter what vibrational energy level the molecule is first excited to, it would soon relax into the lowest vibrational state of the excited state, before it radiatively decays to the ground state (Kasha's rule: "The emitting level of a given multiplicity is the lowest excited level of that multiplicity"[88]). Hence, the emission process always comes with lower energy than absorption (Stokes shift), and the spectra of absorption and emission process are the mirror to each other in the ideal case when no disorder effects are considered, as illustrated in Figure 2-4. Due to these reasons, the stokes shift could be viewed as the consequence of the geometry change of related excited states (backbone planarization, more specifically), and the more rigid the polymer, the smaller the Stokes shift would be[81][89][90]. For the highly planar, ladder-

type polymer such as MeLPPP[81], a very small stokes shift could be observed from the comparison between the absorption and the emission spectra, which shares an impressive similarity to the spectroscopic behavior of single-walled carbon nanotubes (SWCNTs). However, it is not always possible to resolve the theoretical predicted vibronic progression within absorption/emission spectra. For most of the time, energetic disorder within conjugated polymers would tend to blur these sophisticated vibronic features, and only broad peaks merging several vibronic progressions could be observed.

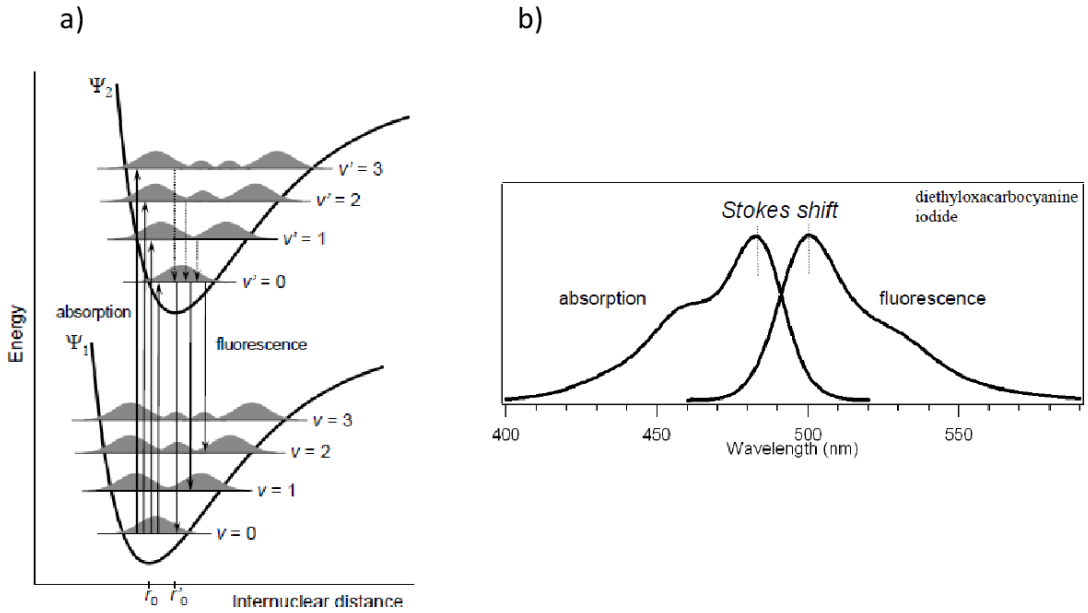

Figure 2-4. (a) Diagram wells representing the Franck-Condon principle and Kasha's rule for the absorption and fluorescence emission processes. (b) Example of an organic compound showing the mirror image of absorption and emission spectra and the Stokes shift. Image and caption adapted from A. Nano [91].

2.3 Charge transport model

In conjugated polymer OFETs, the charge transport mechanism is generally either described by hopping between localized states[92] or delocalized transport above a mobility edge[17]. However, there are recent attempts trying to unify the charge transport

mechanism in organic solids accounting for different density of states (DOS) and various extent of charge delocalization[93].

2.3.1 Hopping transport model

For a sufficiently disordered system, the picture of band-like transport through delocalised states breaks down due to high degrees of structural /energetic disorder, while hopping processes happen between localised states within DOS under applied electric fields, enabling charges to move across an OFET channel. There are two types of hopping, depending on the hopping range, namely the Miller-Abraham hopping[94], which is related to hopping merely happens to the nearest possible site, and variable range hopping (VRH, including Mott VRH and Efros-Shklovskii VRH)[95], during which longer hopping distances are possible. For certain polymers, at different conditions (e.g., different temperatures or doping levels), either model can dominate[96]. Both hopping models show thermally activated behaviours (the exact temperature dependence may be different for different models), since hopping across localised states need to overcome related energy barriers. The longest hopping distance (or charge diffusion length) was theoretically predicted to be on the order of ten backbone repeating units along an ideal conjugated polymer chain[97]; however, only until very recently, hopping process with such a large diffusion length has been experimentally confirmed from the field-induced electron spin resonance (FI-ESR) measurement of an ultra-low energetic disorder D-A copolymer IDT-BT at the 'motional narrowing' regime[98]. More specifically, from the temperature-dependent FI-ESR measurement, hopping distance and motional frequency of charge carriers could be decoupled through the Einstein relationship[99] at the motional narrowing regime, hence providing microscopic charge transport details free from artefacts such as contact resistance.

2.3.2 Multiple trapping and release (MTR) Model

Compared with the hopping transport process, the MTR model[17] assumes a delocalised band which is separated by a mobility edge from the underlying localised trap states. Intuitively, this model corresponds to charge transport systems with higher microstructural order and more delocalised charge transport pictures, however, from a phenomenological point of view, the charge transport process which is predicted by the MTR model is still a thermally activated process following the Arrhenius behaviour.

The MTR model was first developed by P. G. Le Comber and W. E. Spear to explain the temperature-dependent charge transport behaviour between 240K and 290K in amorphous silicon films deposited from silane gas by Plasma Enhanced Chemical Vapour Deposition (PECVD) technique[17]. Later on, Horowitz adopted the MTR model to explain charge transport behaviours within OSCs [100]. It is especially suitable to use this model to describe the charge transport process within highly ordered semi-crystalline polymers, where the co-existence of delocalised states and trap states induced by various sources of disorder contribute to the charge transport process simultaneously[101].

Back to the case of amorphous Si, from the temperature-dependent mobility measurements, it is observed that a critical temperature T_c (240 K) exists to separate the transport behaviour into two different regimes, characterized by the different gradients within mobility versus $1/T$ plots. Below T_c, the chance for charge carriers to be thermally activated into the delocalised band edge is negligible, thus transport within amorphous silicon is purely by tunnelling through localised states within the bandgap of materials, while above T_c, enough thermal energy exists to activate charge carriers into the higher-energy delocalised band for more efficient (higher mobility) charge transport process to happen. However, defects or impurities within materials would create trap states in their bandgaps. Charge carriers transporting through materials would get restrained by these traps, until subsequently thermally released into the delocalised band to move again. Hence the trapping and releasing process would

repeatedly occur during the whole charge transport process, slowing down the mobility of charge carriers compared with the "ideal" mobility at the delocalised band-edge. The similar Arrhenius-type behaviour to hopping transport manifests in the MTR model as well, due to the 'trapping and releasing' nature of charge transport process: namely at a lower temperature, the possibility for trapped charges to be thermally activated and released into the delocalised band within a fixed amount of time would decrease correspondingly. This longer trapping time would naturally slow down the charge transport process compared with the situation at a higher temperature, which is in turn reflected from the temperature-dependent mobility.

There are several assumptions within the MTR model, such as the probability for a charge carrier to falling into a trap state is one once it meets a defective site, and the transport merely happens at the delocalised band edge, while another less efficient (with one order of magnitude lower mobility) charge transport pathway of the slower tunnelling process through localised states is largely blocked and negligible within the interested temperature regime, and would not contribute to the transport process within the MTR model.

As mentioned above, the MTR model would show a thermal activation characteristic. For the simplest case, if there is only one trap energy level underneath the delocalised band, from the temperature-dependent measurements, the activation energy could be extracted, characterizing the energy gap between the trap state and the band edge of the delocalised states. Also, the mobility would be proportional to the ratio of the density of states at these two energy levels, since the higher the trap states density, the more likely a charge would get trapped during a fixed transport process, which means shorter effective mobile time and lower mobility. Hence the temperature-dependent mobility could be derived as[100]:

$$\mu = \mu_0 \cdot \alpha \cdot e^{\left(-\frac{Et}{k_B T}\right)},$$

where μ_0 is the trap-free mobility at the delocalised band edge, α is the ratio of the density of states between the delocalized band edge and the single trapping level

underneath, E_t is the energy difference between the trap states and the mobility edge, k_B is the Boltzmann constant, and T is the Kelvin temperature. Even the initial derivation of this model assumes a single energy level of trap states, it has been proved that for more complicated trap DOS the Arrhenius behaviour still holds, while a small modification to the model needs to be applied by changing E_t to the energy level of the lowest-lying trap states.

In the past, the charge transport models developed would generally assume a spatially uniform DOS, no matter it is band-like, hopping/tunneling, or the MTR model. However, for many semi-crystalline systems, inhomogeneity of the DOS would manifest within materials, due to the co-existence of highly crystalline and amorphous regions, for example. Correspondingly, unique electronic performance within specific systems needs to be explained by more detailed charge transport models, which take into account their microstructure features. For example, the Coulomb interaction enhanced charge transport mechanism has been developed to explain the intrinsic gate-voltage dependent field-effect mobility of the semi-crystalline P(NDI2OD-T2) system successfully[102].

2.4 Organic field effect transistors

2.4.1 OFET architecture

OFETs are three-terminal electronic switches like their inorganic counterparts. Within a specific device, the gate electrode is electrically insulated from the source and the drain electrodes by the dielectric layer. Charge transport happens at the interface between the semiconductor layer and the dielectric layer. For a specific device in-operando, charges are injected into the channel of devices due to the voltage difference between the gate and the source electrode, while a simple metal-insulator-semiconductor model could be used to calculate information such as charge density accumulated, as long as prerequisites such as the specific capacitance of the dielectric

layer are known. After injection, charge transport happens at the device channel, namely, the interface between the OSC and the dielectric layer, then collected at the drain electrode. Four commonly used OFETs architectures are shown in Figure 2-5, and could be classified into two categories, namely coplanar architectures (bottom-gate, bottom-contact (BGBC) and top-gate, top-contact (TGTC) devices), where electrodes and conducting channels are on the same plane or staggered architectures (top-gate, bottom-contact (TGBC) and bottom-gate, top-contact (BGTC) devices), where the semiconductor layer separates electrodes and conducting channels. The OFETs fabricated/ characterised within this work are TGBC devices. Within the staggered architecture devices, the process of carrier injection and collection (through the source and drain electrodes) would go through the semiconducting layer, which is different from the coplanar devices, within which such "vertical" transport process does not happen. However, due to the larger injection area, the contact resistance of the staggered device would be significantly reduced at high gate voltage when the channel becomes more conductive due to increased carrier density, the phenomenon of which is known as the current crowding effect[103]. Moreover, strong gate-voltage-modulated contact resistance at the low gate-voltage regime[104][105] may cause artefacts during mobility extraction, such as the notorious 'double slope' phenomenon[106].

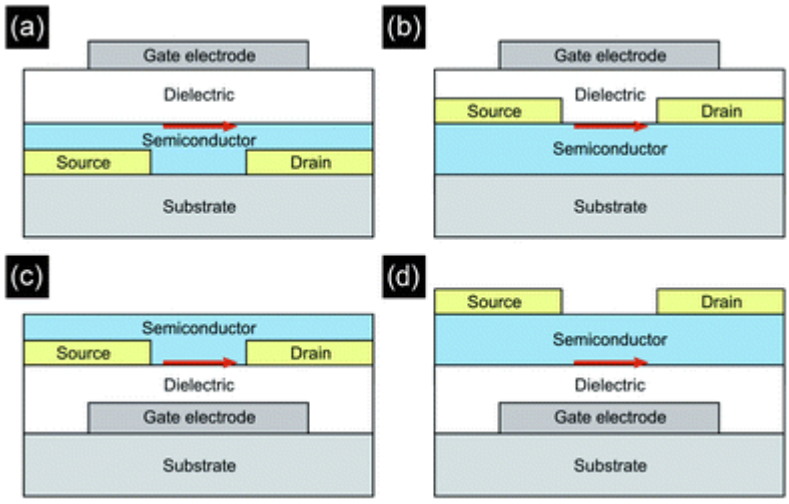

Figure 2-5 Schematic representations of field-effect transistor architectures, (a) top-gate bottom-contact, (b) top-gate top-contact, (c) bottom-gate bottom-contact, and (d) bottom-gate top-contact. The arrow shows the charge conduction interface. Image and caption from J. Smith[107].

2.4.2 Important interfaces in OFETs

Besides the performance and stability of polymeric semiconductors, important interfaces within OFETs also decide the device performance. Two importance interfaces within OFETs would be illustrated here, namely the metal-organic (MO) interface and the organic-dielectric interface.

The nature of the MO interface decides charge carriers' injection/extraction efficiency within OFETs. Not like inorganic FETs, within which ideal ohmic contact is achieved by contact doping and devices work in the inversion mode guaranteeing a low level of off-current, within OFETs, devices work in the accumulation mode, with ideal contact property mainly achieved by the matching of Fermi/HOMO or Fermi/LUMO levels and low off-current due to the negligible intrinsic charge carrier density within OSC films. To first order, the injection barrier is decided by the difference of metal work function with respect to the LUMO/HOMO level of the OSC (depending on which type of charge carriers, holes or electrons are injected/extracted). As shown in Figure 2-6, the mismatch of energy levels can hence lead to large injection barriers with significant contact resistances and non-ideal device behaviors (Schottky-Mott relationship[108]). Therefore, for certain applications which require to inject both

electron and hole effectively, such as ambipolar light-emitting FETs, unsymmetrical electrodes employing both relatively low and high work function metals need to be used to inject electrons and holes respectively[109][110].

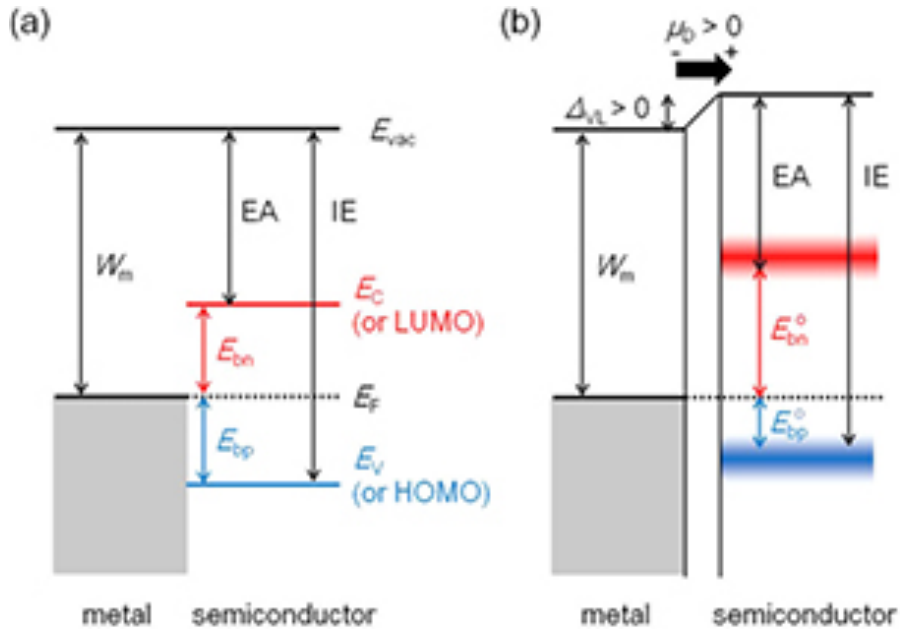

Figure 2-6 (a) Energy diagram for an ideal MO interface. (b) Energy diagram for a realistic MO interface featuring vacuum level mismatch Δ_{VL} and energetic disorder within OSC's HOMO and LUMO. Image and caption from S. Jung[111].

Another interface investigated in this work is the organic-dielectric interface, where charge transport within OFET happens. Geometrically, the charge carriers accumulated within an operating OFET generally distribute within 3 nm to the semiconductor-dielectric interface[112], and the charge carrier concentration is around 3–4 orders of magnitude higher than in a diode structure[113]. Thus, the roughness of the interface[114][115], static disorder[116], surface trap[117], etc., would unavoidably deteriorate charge transport performance. It is worth noting that the dipolar disorder within the gate dielectric also impacts OFET performance. Due to the lower relative permittivity of OSCs[118] compared with inorganic materials, the impact of such dipolar disorder is harder to be screened out over distance within materials, impeding the charge transport process at this critical OSC-dielectric interface. For example, Figure 2-7 illustrates the widening of the DOS at the charge transport interface due to the dipolar disorder within the gate dielectric. Such a change in DOS has been proved to

cause detrimental localization of charge carriers and reduction in field-effect mobility[116].

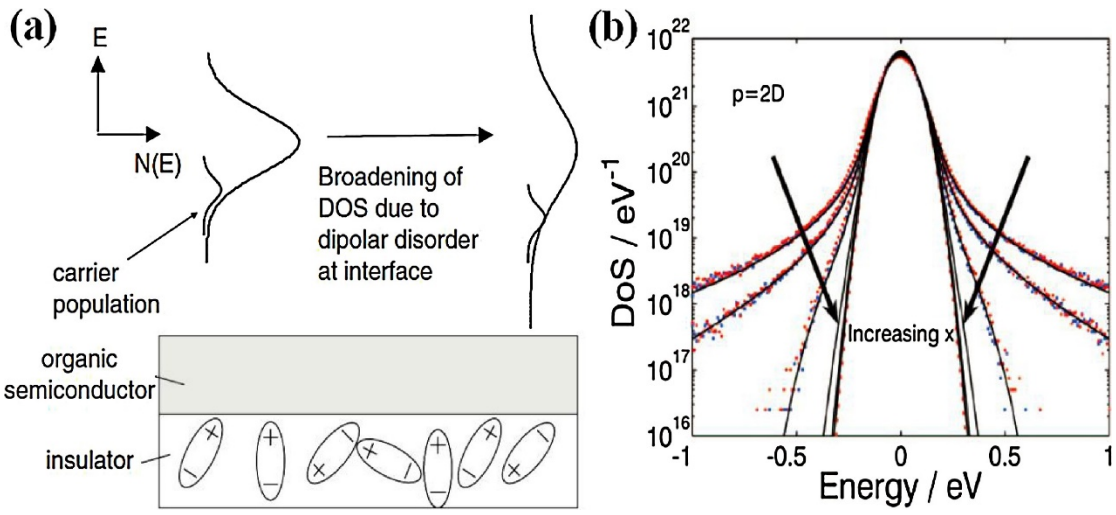

Figure 2-7 (a) Broadening of DOS due to polar disorder within OFETs' dielectrics. (b)Variation of DOS broadening with an increasing distance (step of 1 Å for each line from 0-5 Å) from OSC-dielectric interface into the bulk of semiconductor." Image and caption from T. Richards[119].

2.4.3 OFETs' working mechanism

Metal-insulator-semiconductor (MIS) model[120][121] could be applied to understand charge accumulation behaviour within OFETs. Not like inorganic FETs, OFETs always work in accumulation mode due to the negligible concentration of intrinsic charge carriers compared with inorganic semiconductors such as single-crystalline silicon (~$1 \cdot 10^{10}$ cm^{-3} [122]). For the study of the n-channel charge transport within this work, during the gating process, a positive voltage would be applied at the gate electrode, accumulating electrons within the channel (electrons are injected from source electrodes). Trap states at the OSC-dielectric interface need to be filled before mobile charge carriers could be accumulated, and this leads to a threshold voltage V_T during OFET operation. In terms of the gating technique, common solid dielectric materials used in the OFET technology are capable of reaching a carrier concentration

on the order of 10^{12}/cm^2. Accumulating higher charge carrier density would be challenging, since all the dielectric has a limited breakdown field (breakdown field for SiO_2: E_b = 10 MV/cm [123], for example). For commonly used polymer dielectrics including Cytop and electronic-grade polymethyl methacrylate (PMMA), the relative permittivity is between 2-4, with typical specific capacitances on the order of 10 nF/cm^2 (thickness on the order of 100 nm); the most commonly used inorganic dielectric, 300-nm thick thermal SiO_2, has a specific capacitance of very similar value (11.5 nF cm^{-2} [124]). In order to boost the specific capacitance further and accumulate higher density of charge carriers with the same or even smaller gate voltage, electrolyte gating technique could be used, the working mechanism of which is based on the formation of super thin (~1 nm) electrical double layers (EDLs) at the gate/electrolyte and electrolyte/semiconductor interfaces[123]. Since the specific capacitance is inversely related with the thickness of the dielectric layer, a much higher specific capacitance on the order of 1 μF/cm^2 could be achieved due to the super-thin EDLs, which means charge carrier concentration on the order of 10^{13} cm^{-2} can be easily accumulated by merely applying gate voltage within a few volts. Such low-voltage operation is very attractive for emerging applications such as wearable electronics.

In terms of the operation regions, when the drain voltage is much smaller than the gate voltage, devices work in the linear region, which could be thought of as gate-voltage controlled variable resistors, corresponding to Figure 2-8 (a). However, once the drain voltage increases to the level approaching gate voltage, pinch-off region starts to form close to the drain electrode, with the onset of drain current saturation with increasing drain voltage. Further increase of drain voltage would merely shift the pinch-off point and increase the length of depletion regions, without changing the saturated drain current, as shown in Figure 2-8 (c).

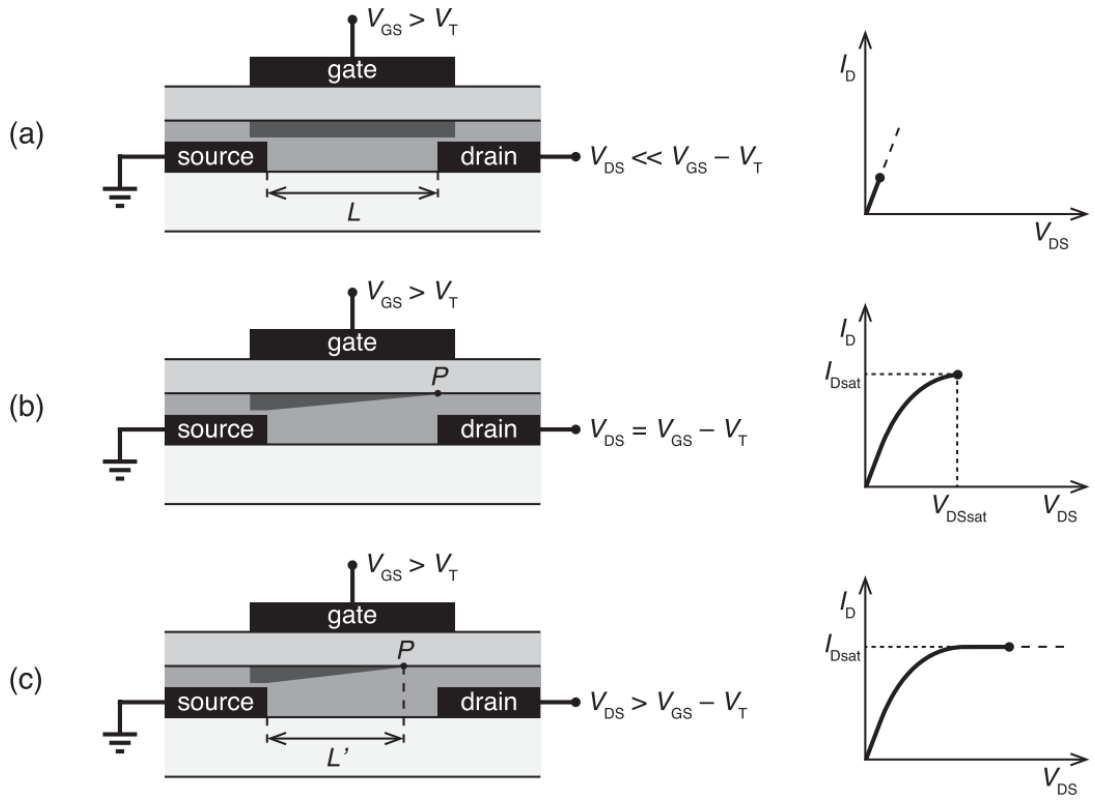

Figure 2-8 charge distribution in TGBC OFET's channel and current-voltage characteristics in the different regimes: (a) the linear regime; (b) starting of a channel's pinch-off; (c) the saturation regime. Image and caption from L. Herlogsson[125].

To quantitatively derive the I-V relationship within an OFET and calculate mobility of charge carriers, the gradual channel approximation[126] method is used within this work. This model is based on the assumption that the vertical dimension of the MIS structure is significantly smaller than the channel length of devices investigated, such that the vertical electric field dominates the profile of the electrical field within devices. Within this study, the dielectric thickness used is around 500 nm, while the channel length of devices investigated is either 20 μm or 100 μm. Hence at least one order of magnitude dimensional difference is guaranteed within devices' architecture, satisfying the requirement of gradual channel approximation.

Based on this model, drain current I_D could be expressed as:

$$I_D = \frac{W \cdot C_i}{L} \cdot \mu \cdot ((V_G - V_T) \cdot V_D - \frac{V_D^2}{2}),$$

where W is the channel width, L is the channel length, C_i is the specific capacitance of the dielectric layer with unit of F/cm^2, μ is the field effect mobility with unit of $cm^2V^{-1}s^{-1}$, V_T is the threshold voltage of the OFET.

From the equation above, linear mobility ($V_D << V_G$) could be calculated as:

$$\mu_{\mathrm{lin}} = \frac{\partial I_{\mathrm{D}}}{\partial V_{\mathrm{G}}} \cdot \frac{L}{W \cdot C_{\mathrm{i}} \cdot V_{\mathrm{D}}},$$

While saturation mobility ($V_D \geq V_G - V_T$) could be calculated as:

$$\mu_{\mathrm{sat}} = \left(\frac{\partial \sqrt{I_{\mathrm{D}}}}{\partial V_{\mathrm{G}}}\right)^2 \frac{2 \cdot L}{W \cdot C_{\mathrm{i}}}.$$

However, except for very few materials[20][29], it is generally rare to obtain ideal MOSFET like charge transport behaviors from OFETs. A few reasons contribute to such non-ideality, such as significant injection barriers originated from non-ohmic contact at source and drain electrodes[127] and energetic disorder at the OSC-dielectric interface. As a result, it is hard to obtain gate-voltage independent mobility with a negligible threshold voltage for non-optimized OFETs. More seriously, kinks within transfer curves obtained from certain devices would cause significant mobility extraction exaggeration[106] and mislead researchers within the field. Hence, models are proposed recently to examine the reliability of mobility extraction within OFETs in a uniform and quantitative method, with the reliability factor introduced to parameterize devices' non-ideality[124]. However, the reliability factor does not have a clear physics interpretation, because various reasons for non-ideality may give the same number of the reliability factor. Hence a deeper understanding to figure out the underlying reasons for various non-ideal behaviours is in need. Besides the previously mentioned ‘double slope’ caused by gate-modulated contact resistance at the low gate voltage range, the comparison between the linear and saturation mobility is also important and worth paying attention to. And the linear mobility would be much more reliable due to the more uniform distribution of charge carrier density across the whole channel, hence giving more accurate value for the normally reported gate voltage dependent mobility. With the consideration of these potential artefacts during mobility calculation, in this work we carefully compare the linear and saturation mobility to estimate the accuracy

of our mobility extraction, and pay careful attention to the related output curves to examine the influence of contact resistance on charge transport property.

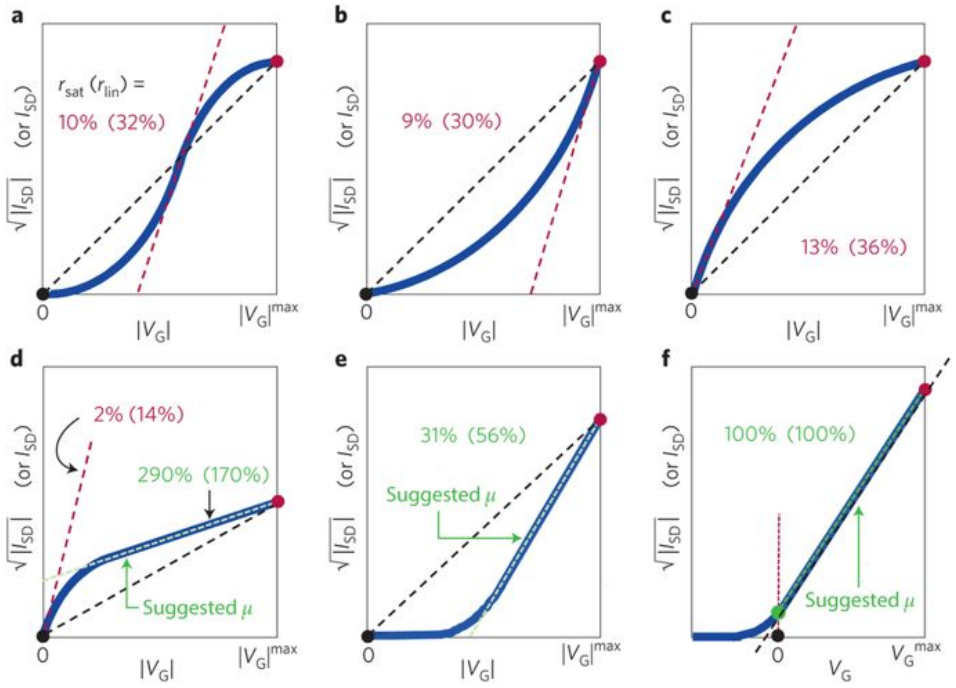

Figure 2-9 various non-linear transfer characteristics of OFETs, Image and caption from H. H. Choi[124].

2.5 Glass transition process and dynamic mechanical analysis of conjugated polymers

High mobility, stable charge transport at high temperature (above 100°C) is highly desirable for many semiconductor applications[128][129]. For hopping processes within OSCs, in principle, the transport would always be facilitated at elevated temperatures due to thermal activation, which could manifest as higher mobility for OFETs. However, in real systems, mobilities reach a plateau or even drop at certain temperatures[130], partly due to chain movements that lead to unfavorable effects such as the disruption of interchain contacts. In other words, thermally activated hopping behavior would be counteracted by adverse microstructural changes at higher temperatures[131][132]. For example, charge-carrier mobilities start to decline at above 100°C for most OFETs, except for very few cases[133]. Due to the mentioned reasons, to figure out the temperature regime around which significant chain movements happen would be very helpful to design annealing protocols and predict the morphology and performance

stability of OSC devices. A detailed study of the glass transition process within organic solids is thus needed.

2.5.1 Glass transition process

The glass transition temperature, T_g, is the temperature at which the amorphous regions change from a glassy to a rubbery state, reflecting the elevated mobility of individual polymer chains at higher temperatures[134][135]. It is not a well-defined, thermodynamic, structural phase transition but depends on experimental conditions; it is related to the temperature at which the timescale for the temperature-dependent structural relaxation of the polymer becomes comparable to the timescale of the experiment. For solution-processed conjugated polymer thin films, even the most crystalline ones tend to have a mixed microstructure composed of crystalline and amorphous domains[33]. Their relative proportions depend on the chemical design of the polymers[77] and processing details[56]. Investigation of glass transition behavior is hence uniformly relevant for all thin films of conjugated polymers. The glass transition process is sometimes referred to as the α-transition or relaxation, which is the main relaxation process for conjugated polymers and involves substantial coordinated backbone motion (including translational and rotational motion[136]). It is associated with a clear change in the materials' mechanical properties. There exist other relaxation processes for conjugated polymers as well, which occur typically at lower temperatures, namely the γ-and β-transitions with $T_\gamma \leq T_\beta \leq T_g$ [137]. These two relaxation processes involve smaller energy scales and structural relaxation over more localized length scales. More specifically, the γ-transition with the lowest temperature corresponds to the activation of highly localized motion or bond deformation such as stretching and bending[138], while at higher temperatures, T_β, larger-scale segment motion involving whole molecular units, such as the solubilizing side-chains, are expected to set in[137]. At temperatures above T_g, once the melting temperature T_m is reached, the polymer

chains within both amorphous and crystalline domains slide freely, causing a flow of the material[135].

In the literature, T_g has been used to quantify mechanical[65] and thermal properties[135][139] of an extensive library of materials used in a variety of electronic and optoelectronic devices. Knowing the T_g of conjugated polymers not only has practical implications for polymer processing like predicting morphological stability of materials[140][141] and optimizing annealing protocols[135] of films but also gives information about the polymers' basic properties at molecular levels, such as the backbone rigidity and interchain interaction[135] . Stiffer backbones tend to induce higher T_g, due to a higher barrier to translational and rotational motion. Thus, T_g has been well correlated with persistence length[142] and rotational volume[143][144] for different conjugated polymers. The strength of interchain interactions also affects molecular-level friction forces and the relative motion of chain segments and would change T_g accordingly. For example, in blends of poly[N-9'-heptadecanyl-2,7–carbazole–alt-5,5-(4',7'-di-2-thienyl-2',1',3'-benzothiadiazole)] (PCDTBT) with fullerens, which are widely studied in organic solar cells, a disruption of π-π stacking induced by annealing was correlated with a reduced T_g of these blends.[145] Additionally, it is well known that nanoscale confinement could reduce the motion of chain segments and increase T_g[146]. Another important consideration in these materials is the nature of the interfaces between crystalline and amorphous domains, which exert restrictions on the motion of polymer chains within the neighboring amorphous regions, making them more resistant to relaxation dynamics. This is widely used to explain the T_g elevation caused by increased crystallinity within a range of semi-crystalline materials[73][146].

2.5.2 Dynamic mechanical analysis (DMA)

Figure 2-10 (left) Triton DMA setup in Cavendish Lab (right) A clamped powder pocket in the DMA (note the furnace cover is removed). Image and caption from P. Royall [147]

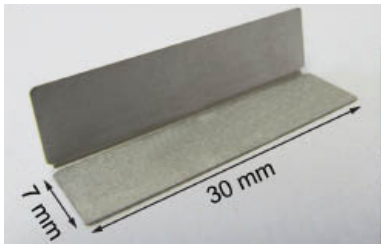

Figure 2-11 Photos of a material pocket. Image and caption from R. Ou[148].

DMA is one of the most sensitive experimental techniques for detecting glass transitions and structural relaxation processes. The specific model used in this work is a Triton 2000 DMA, which is a handy benchtop setup (Figure 2-10) located at the Cambridge Centre for the Physics of Medicine, University of Cambridge. It involves applying an oscillating strain $\gamma^* = \gamma_0 \cdot exp\,(i\omega t)$ with amplitude γ_0 and oscillation frequency ω to a sample of the polymer and measuring the resulting stress $\sigma^* = \sigma_0 \cdot exp\,[i(\omega t + \delta)]$ with amplitude σ_0 and a phase delay δ between the stress and strain. This allows determination of the complex modulus $G^* = G' + i \cdot G'' = \frac{\sigma^*}{\gamma^*}$ where $G' = \frac{\sigma_0}{\gamma_0} \cdot cos\,\delta$ is the storage modulus and $G'' = \frac{\sigma_0}{\gamma_0} \cdot sin\,\delta$ is the loss modulus. A plot of the damping factor $tan\,\delta = \frac{G''}{G'}$ gives information about the viscoelastic property of samples as a function of temperature and frequency. As a general trend, polymers lose elasticity (decrease of storage modulus) and gain viscosity (increase of

loss modulus) during β or α transition, resulting in a rise of the damping factor, which allows locating the related transition temperature. Compared with other commonly used methods to measure T_g, such as differential scanning calorimetry (DSC)[149] which is based on the measurements of variations in the polymer's heat capacity, DMA could demonstrate several orders of magnitude higher sensitivity to the detection of the glass transition[150], since it captures the large, associated changes of mechanical properties directly. Therefore, DMA offers a unique and detailed insight into the bulk property of the amorphous regions in these high mobility polymers and advances our understanding of the relationship between chemical design of the polymer and the microstructure of the amorphous domains that cannot be obtained from X-ray diffraction experiments. This is important since we can begin to link the elusive amorphous regions in these state-of-the-art conjugated polymers to the observed photophysical and charge transport properties.

In general, DMA mainly applies to the measurements of self-supporting samples, such as rubber and plastic bars/stripes. However, recently, this technique demonstrates its capacity for broader applications such as measuring powders or granules with material pockets(a folded sheet of stainless steel, **错误!未找到引用源。**)[147]. However, due to the unclear sample geometric, accurate modulus of materials could not be measured out directly, which is a significant drawback of the material pocket approach. In other words, the much stiffer stainless steel pockets would dominate modulus signal, masking the much weaker signals from softer polymer powders. During experiments, the material pocket clamped is subjected to a sinusoidal strain imposed by the driveshaft of the DMA machine (for all the measurements related to this work, a single-strain configuration is used), which in turn shears the polymer powder within it. Hence to a certain extent, DMA measures the response of polymer powders under pressurized interchain friction directly. In the meanwhile, DMA records the phase and the amplitude of the induced stress. Combined with strain parameters, the setup could calculate the modulus of the sample. Since conjugate polymers generally hold viscoelasticity, the strain would normally lag behind the stress by a phase angle δ.

Figure 2-12 illustrates the stress response of an elastic, a viscous, and a viscoelastic material under a sinusoidal strain.

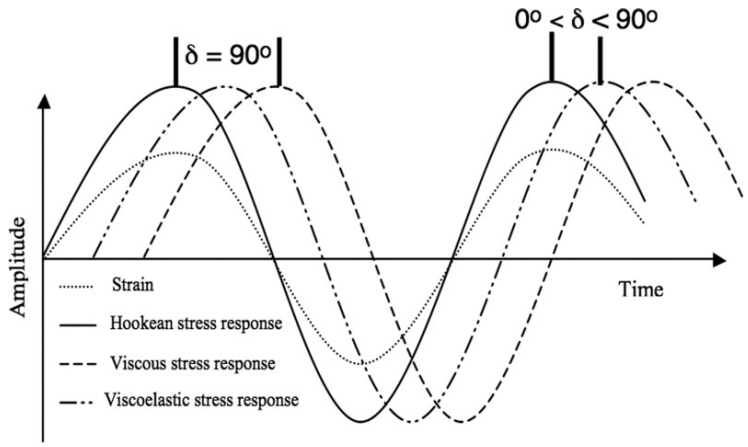

Figure 2-12 Stress response of an elastic, a viscous and a viscoelastic material following application of a sinusoidal strain. Image and caption from D. S. Jones [150].

3. Materials and experimental methods

In this chapter details about materials, processes and measurement techniques relevant to this work will be presented.

3.1 Conjugated polymers

3.1.1 single-bond linked polymer system

Various conjugated polymers are investigated in this work as semiconductor materials for OFET applications. Various homopolymers and donor-acceptor (D-A) conjugated polymers are included in this work, with aromatic units that are linked together by single bonds along polymer backbones. However, since the structural disorder in the Cartesian domain would lead to the energetic disorder in the energetic domain, in most traditional conjugated polymers single-bond linkages are the source of significant disorder in the chain conformations and electronic density of states that are caused by variations of the torsional angles between conjugated units linked by these single carbon-carbon bonds.

Lower energetic disorder could provide a more uniform energetic landscape for a more efficient charge transport process [32][151]. For example, fused, extended aromatic rings help to lower the energetic disorder of conjugated polymers significantly, like the case of IDT-BT[29] and TIF-BT[152]. For the case of IDT-BT, the extended electron-donor unit significantly reduces conformational and energetic disorder of polymers, showing record-low excitonic disorder with an Urbach energy of 24 meV measured from the photothermal deflection spectroscopy(PDS) technique, which is even smaller than the room-temperature thermal energy k_BT (ca. 25.9 meV), and achieving high μ_{FET} above 1 $cm^2V^{-1}s^{-1}$ within OFETs[29]. In the following work, Hu *et al*. expanded the successful design motif of IDT-BT, further extending the IDT moiety into a more rigidified and extended dithiopheneindenofluorene (TIF) unit, and hence achieve ultra-high hole mobility up to 3 $cm^2V^{-1}s^{-1}$.[152] A family of similar IDT-BT materials is included within this work, with chemical structures shown in Figure 3-1. This important

family of materials is investigated to correlate their mechanical property to their sub-bandgap absorption/photoluminescent property 错误!未找到引用源。, and the correlation between the nature of inter-chain short-contacts and their glass-transition behaviours is investigated in the Chapter 6.

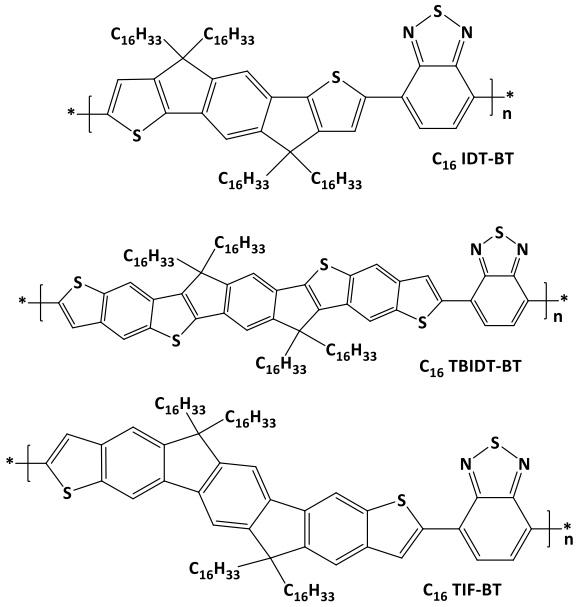

Figure 3-1 A series of IDT-BT like materials used in this work with different backbone structures but the same side-chain structure. (synthesized by Dr. Weimin Zhang from the Department of Chemistry and Centre for Plastic Electronics, Imperial College London and Dr. Hu Chen from KSC, King Abdullah University of Science and Technology (KAUST)).

Other high-mobility, single-bond linked conjugated polymers used in this thesis include two ambipolar DPP polymers, namely DPPBTz[153] and DPPSe-12[154], an n-type polymer p(NDI2OD-T2)[49], and a p-type polymer PBTTT, the chemical structure are shown below in Figure 3-2 错误!未找到引用源。.

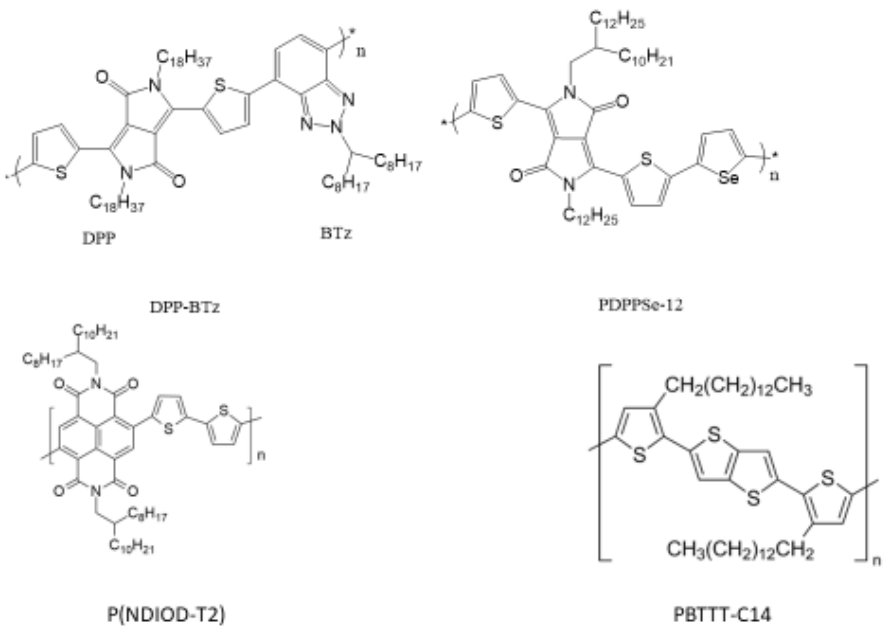

Figure 3-2 other high mobility semi-crystalline polymers used in this work.

3.1.2 double-bond fused polymer system

Torsional disorders at these single-bond linkages would introduce energetic disorders to the system, likely to degrade charge transport property of these materials. To reduce the torsional disorders, McCulloch *et al.* developed a family of rigid-rod, conjugated polymers comprising fused-ring units that are linked together merely by double as opposed to single, carbon-carbon bonds[75]. According to the DFT simulation, this unique backbone feature imparts these fused polymers with much higher torsional barriers compared with more traditional single-bond linked polymers[75]. While polymers with only double-bond linkages would be expected to behave as rigid rods but little is known about their electronic structure nor about their chain conformations and persistence lengths. In this work we investigate the structure-property relationship of a family of rigid-rod polymers to uncover their microstructure/electronic property. First we would show the chemical structures of these polymers as below.

Naphthalene-co-naphthalene fused polymers are the family of material explored mostly in this work due to relatively easy synthesis compared with other fused polymer structures. Side-chain engineering[155–157]as utilized to optimize the microstructure of polymer films and OFETs performance. More specifically, we designed derivatives in

which the branch-point is moved further away from the backbone[43][158] to promote crystallinity and charge transport property.

The first series of materials introduced here are four naphthalene-co-naphthalene fused polymers with different kinds and lengths of side-chains as shown below, typical strategies like purely branched or linear side-chains, alternating linear and branched side-chains[159] and strategy of adjusting alkyl chain branching positions[158][160] are explored to increase interchain π-π stacking and enhance charge transport properties. Chemical structures of these four polymers are shown in Figure 3-3.

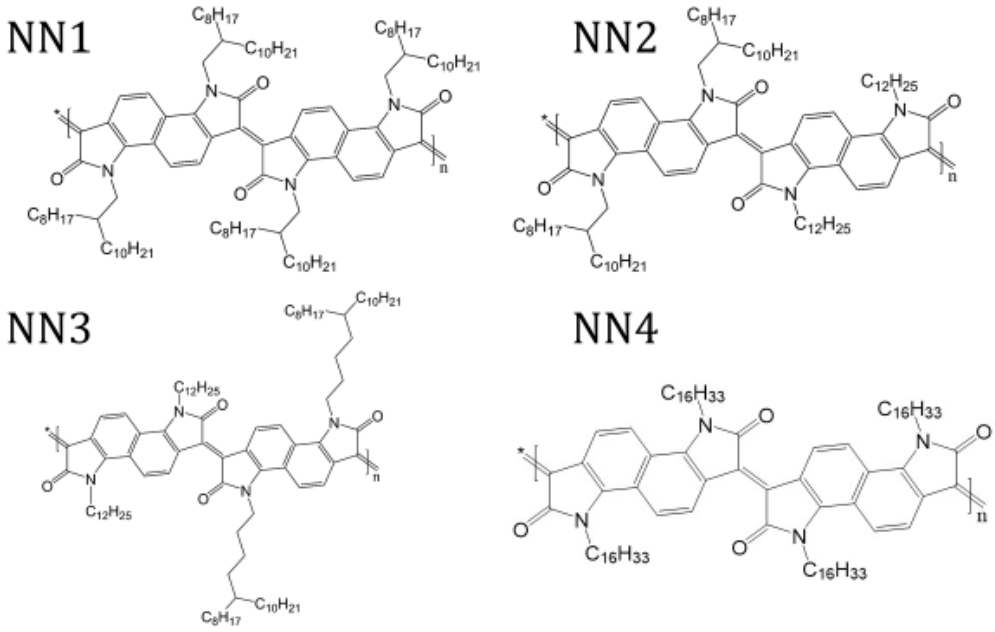

Figure 3-3 Four kinds of naphthalene-co-naphthalene fused polymers with different lengths and types of side chains, termed as NN1, NN2, NN3, NN4 respectively (synthesized by Dr. Wan Yue, Cameron Jellett, Ada Onwubiko, Dr. Hung-Yang Chen from Department of Chemistry, Imperial College London and Dr. Hu Chen, Dr. Balaji Purushothaman from KSC, King Abdullah University of Science and Technology (KAUST), Professor. Wan Yue, HaiLiang Liao from Sun Yat-Sen University, Guangzhou, China).

The second series of materials introduced here is naphthalene-co-naphthalene fused polymers with different lengths of the linear side chains, ranging from C8 linear chain to C16 linear chain, while the branching side-chain keeps the same as NN2. Chemical structures of these five polymers are shown below in Figure 3-4.

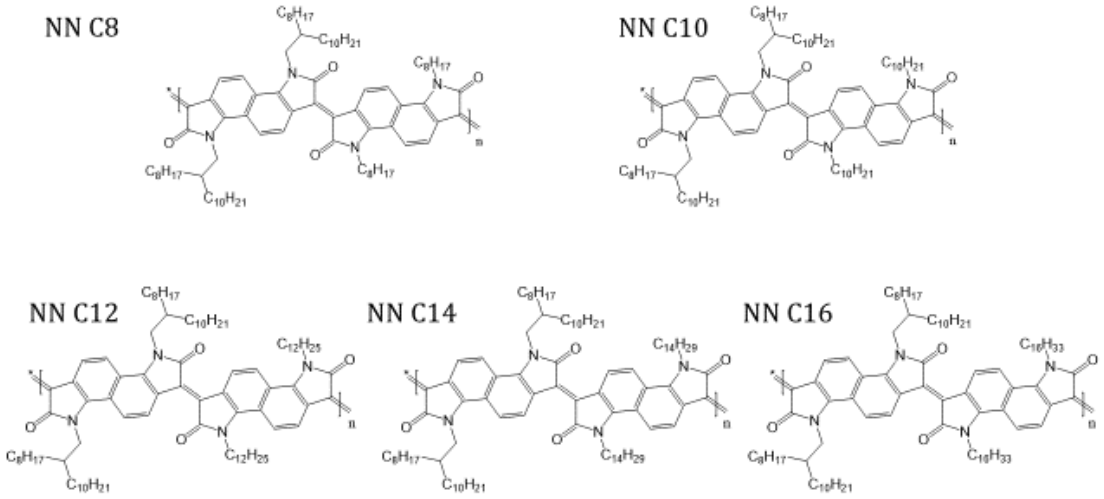

Figure 3-4 Five kinds of naphthalene-co-naphthalene fused polymers with different lengths of linear side chains, termed as NN C8, NN C10, NN C12, NN C14, NN C16 respectively (synthesized by Professor. Wan Yue, HaiLiang Liao from Sun Yat-Sen University, Guangzhou, China)

Based on the same optimisation strategy of backbone extension, our collaborators designed and synthesized further extended version of fused polymers, namely copolymer designs with some units extended from a naphthalene to an anthracene core to extend the conjugated backbone, which brings the anthracene-co-naphthalene polymer (termed as the AN polymer) and anthracene-co-anthracene polymer (termed as the AA polymer) designs, as shown in Figure 3-5.

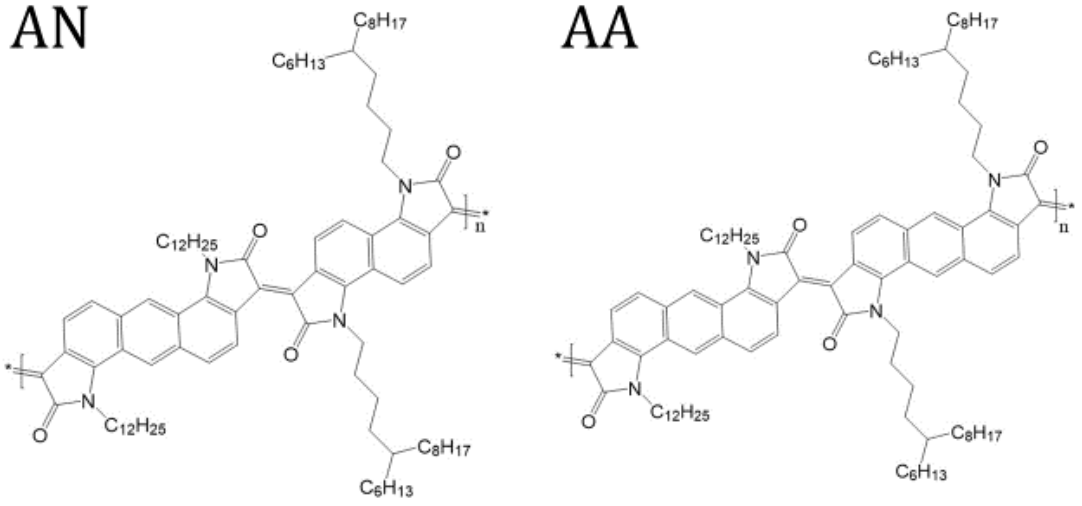

Figure 3-5 Anthracene-co-naphthalene fused polymer and anthracene-co-anthracene fused polymer(synthesized by Dr. Wan Yue, Cameron Jellett, Ada Onwubiko, Dr. Hung-Yang Chen from Department of Chemistry, Imperial College London and Dr. Hu Chen, Dr. Balaji Purushothaman from KSC, King Abdullah University of Science and Technology (KAUST)).

3.2 Dielectrics

In this work, OFET devices with TGBC architecture are used. Due to this, solution-processable, polymeric dielectrics are exploited to optimize the charge transport property of corresponding devices. The dielectric material used is electronic-grade poly (methyl-methacrylate), purchased from Polymer Source inc. Canada. The specific type of PMMA used is P8509-MMA, with a high number-average molecular weight of 300kDa and a small poly dispersity index (PDI) of 1.05, measured from size exclusion chromatography (SEC) in tetrahydrofuran (THF). The dielectric constant of this material is 3.6.

3.3 Device fabrication

In this work, Top-gate bottom-contact architectures are used to fabricate all the field-effect devices. 0.7 mm thick borosilicate glass (Corning 1737F) from Präzisions Glas & Optik were used as substrates. The substrates were cleaned in a sequence of ca. 2 ‰ volume ratio Decon 90 with DI water, pure DI water, acetone, and Isopropyl alcohol (IPA) for five minutes of each step by sonication. Then the substrates were blow-dried with nitrogen gas and plasma-ashed for 10 minutes with the power of 300 watts. After these processes, glass substrates are clean and ready for the next photolithography steps.

Patterns of source and drain electrodes were defined by photolithography. LOR 5B and S1813 are used as interlayer and positive photoresist, respectively. More specifically, LOR 5B is used as an interlayer in direct contact with glass substrates and is responsible for creating undercuts during the developing processes(with the MF319 as the developer). This undercut, in conjunction with metal evaporation, will produce a discontinuity in the deposited layer allowing following lift-off process in N-Methyl-2-pyrrolidone (NMP). The spin-coating speed of LOR 5B is 5000 rpm giving a film thickness of ca. 400 nm. After spin-coating, the substrates are baked at 190 °C for 5 minutes. After this step, positive photoresist S1813 was spun on top of the solidified LOR5B layer with the same spin-coating parameter, and the sample was baked again for another 2 minutes in air at 120 °C to dry out the S1813 layer thoroughly. Then in the following step, the substrates were exposed with UV light through a patterned mask to define the inter-digitated electrodes (channel length L = 20 μm, channel width W = 1000 μm). After this step, MF-319 developer is used to getting rid of all the LOR 5B and S1813 in photolithography defined electrodes' region due to the change of materials' solubility during the photolithography process.

A double or triple layer structure is used to deposit the metallic electrode contact, in order to optimize adhesion and injection. A first 3 nm layer of chromium is evaporated directly on top of the glass to improve adhesion of the following gold electrode, then on top of it, 25nm gold is evaporated. The whole process is done at a pressure less than 6×10^{-6} mBar and rate of 0.5-1 Å/s. For certain devices, in order to improve electron injection, another Indium tin oxide (ITO) injection layer is used. The

additional ITO layer (3nm) was sputter-coated on top of gold electrodes (ITO sputtering done by ShiJie Zhan, Department of Engineering, University of Cambridge), to fully utilize its lower work function to help electron injection into the LUMO orbitals of conjugated polymers used.

After evaporation steps, substrates were put into 1-Methyl-2-Pyrrolidinone (NMP) solution for more than eight hours to gradually dissolve all the LOR 5B and S1813 left, finally lifted off the electrodes. After these procedures, substrates were cleaned with acetone and IPA to wash away all the NMP left, blow dry with nitrogen and ready to be used. Four types of OFETs substrates are fabricated in this work: standard 5 μm, 10 μm, 20 μm channel lengths devices with channel width 1000 μm(L=5 μm,10 μm, and 20 μm, W=1000 μm), oriented 20 μm channel length device with channel width 1000 μm, with devices channels oriented to perpendicular directions on the sample.

For the spin-coating process of the fused polymers, due to the low solubility of this family of material, polymers could be dissolved well only within two kinds of hot chlorinated solvents: 1,2-dichlorobenzene and 1,2,4-trichlorobenzene. Hot polymer solution (110 °C) was spin-coated on top of substrates at 1500 rpm for 60 seconds, then annealing on top of hot plates at 120 °C for 30 minutes. Finally, a shadow mask is used to evaporate gate electrodes. In this work, aluminum is used for gate evaporation in an inert atmosphere. The pressure is controlled below 5×10^{-6} mbar, and the evaporation rate of 5 Å/s-40 Å/s, since it is very hard to control the evaporation rate of aluminum accurately.

3.4 Characterization techniques

3.4.1 Electronic characterization

Room temperature electrical characterization of OFETs were measured within probe stations. Three electrodes of OFETs were connected to three source-measurement units (SMUs) of Agilent 4155 Semiconductor Parameter Analyzer (SPA), the signals were recorded with a bespoke LabView program.

The source voltage was kept zero during measurements. Transfer characteristics were measured by sweeping the gate voltage (V_G) with fixed source-drain voltage (V_D). Output characteristics were measured with fixed V_G, by sweeping V_D. $|V_D|$ = 5 V was used to measure the linear characteristics, and $|V_D|$ = 50V or 60V was used to measure saturation characteristics.

The temperature-dependent characterizations of OFETs were done within a probe station (Lake Shore TTPX Cryogenic Probe Station). Measurements were recorded as above in high vacuum ($\leq 5\times10^{-6}$ mBar) after thermal equilibration ($\sim$ 10 minutes) of the substrate between liquid-N_2 flow and a resistive heater (Lakeshore 331S). Devices were mounted on a metal stage with a thin layer of Apiezon thermal grease between the bottom of devices and the station stage to improve thermal contact further.

Capacitance-frequency (C-f) measurement is performed by HP 4912A Impedance Analyzer (50 Hz to 1MHz) with 0.1V and 0.5V sinusoidal oscillating amplitudes. Capacitance value used for the calculation is extracted from sufficiently low frequency (< 100 Hz). C-f curves are measured for the (c.a. 500 nm) spin-coated PMMA dielectric layer sandwiched between two overlapping aluminium electrodes. The bottom aluminium electrode was evaporated on top of a pre-patterned ITO layer (in the middle of the glass substrates). The overlapping area between the two electrodes is 0.045 cm^2.

3.4.2 Absorption measurements

Normal thin-film steady-state absorption was measured on a calibrated UV-VIS-NIR Spectrophotometer (UV-3600 Plus from SHIMADZU). For more sensitive measurements, especially for characterizing the ultra-weak sub-bandgap absorption (such as certain charge-transfer states), photothermal deflection spectroscopy (PDS) measurements were performed. Simply put, the PDS technique is a pump-probe

spectroscopy technique based on a similar working mechanism to the "mirage effect": The probe light beam is refracted when it passes parallel to the sample surface, on top of which a gradient of temperature, and hence refractive index, build up due to the heat released from non-radiative relaxation of polymer samples after the excitation of the pump beam (pass perpendicular to the sample surface). Samples were prepared identically as the ones used for the transistor measurements, but infrared transparent fused silica substrates (Quartz Windows from the UQG Optics) were used as substrates instead. The samples were first hermetically sealed in a quartz liquid cell filled with an inert perfluorocarbon, which has a significant temperature-dependent refractive index and could serve as an effective deflection medium. During an experiment, a monochromatic pump beam impinges perpendicularly on a sample surface, forming temperature and refractive index gradients near the sample surface due to the heat released, bending the tightly focused continuous-wave laser beam (the probe beam) passing through the deflection medium, producing a deflection proportional to the absorbed pump light at that particular wavelength, which is detected by a quadrant photodiode. Scanning the targeted spectrum hence builds up the whole absorption spectrum with high sensitivity. Based on its unique working mechanism, PDS gives much higher sensitivity compared with standard UV-VIS-NIR measurements, hence rendering it suitable for the characterization of the weakly-absorbing band-tail region[161]. Also, it could serve as a complementary technique when transmission-based absorption spectroscopy techniques are not applicable. The scheme of the PDS setup used in the Cavendish Laboratory is shown in Figure 3-6. More Details about the setup components and types/models of the deflection medium could be found at reference [162].

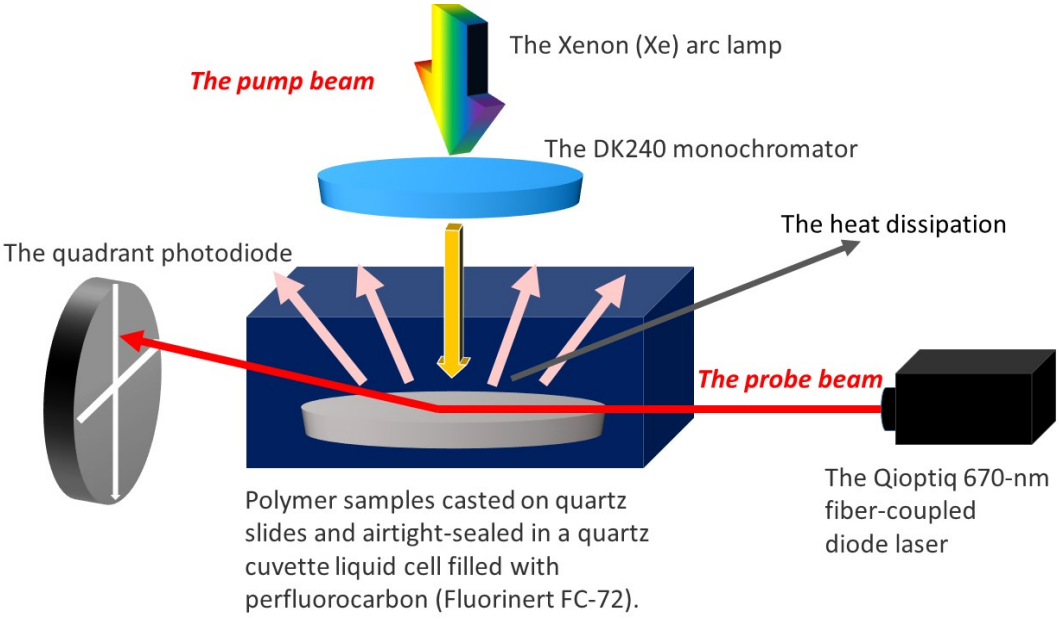

Figure 3-6 The scheme of the home-built PDS setup in the OE group, the Cavendish Laboratory.

The band-tail region of the absorption spectrum reveals important information, such as the degree of energetic disorder within materials, which broaden the absorption onset and create an exponential sub-bandgap tail (Urbach tail)[161], as shown in Figure 3-7. We extract the Urbach energy, which characterises the width of the joint excitonic density of states and is a measure of energetic disorder[161][163], by fitting the exponential tail of the PDS spectra to the equation:

$$\alpha(\hbar\omega) \sim exp\left(\frac{\hbar\omega - E_g}{E_u}\right),$$

Briefly speaking, the Urbach energy parameterise the width of the joint density of states (JDOS) of the transition, and a smaller value of E_u (or a sharper JDOS near the energy gap), indicates a lower energetic disorder of the JDOS. Typically, high-mobility polymers have a E_u<80 meV, including poly(3-hexylthiophene) (P3HT; E_u=52 meV) and (pBTTT; E_u=58 meV)[163]. Now the conjugated polymer with the lowest Urbach energy is IDT-BT, which is 24 meV according to the result presented in D. Venkateshvaran's work[29], even smaller than the thermal energy k_BT at 300K, which is around 25.9 meV.

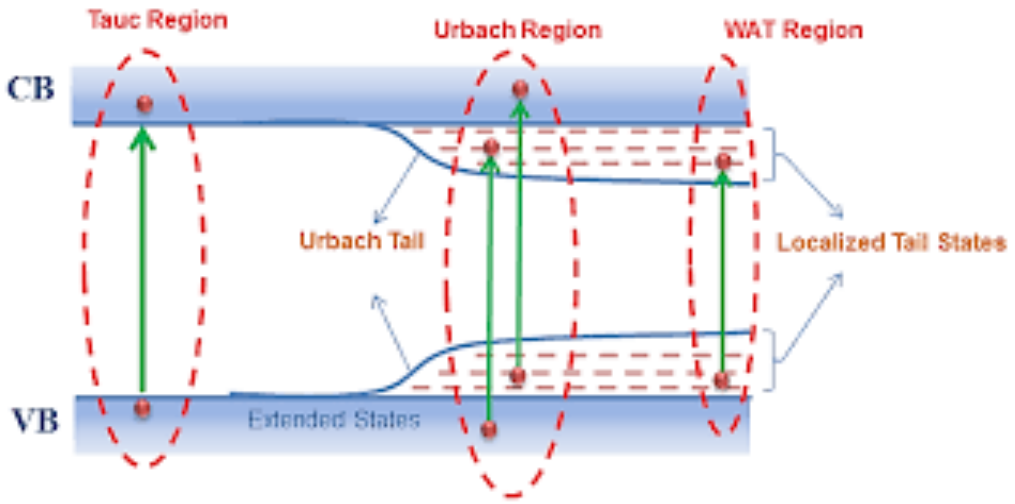

Figure 3-7 Schematic representation of various transitions between valence band (VB) and conduction band (CB). Tauc region, Urbach region and weak absorption tail region are highlighted with dotted circles. Image and caption from N. Sharma [164]

However, the level of the energetic disorder of conjugated polymers is still significantly higher than other state-of-the-art inorganic/hybrid semiconductors. For example, high-quality hybrid perovskite shows an E_u around 10meV at 100K which increases to around 15meV at room temperature[162], showing significantly lower energetic disorder than conjugated polymers, approaching the E_u of single-crystalline inorganic semiconductors, such as the GaAs(E_u = 7.5 meV) and c-Si (E_u = 11 meV). The Urbach tail of the $CH_3NH_3PbI_3$ perovskite thin film is benchmarked against other inorganic semiconductors in Figure 3-8, with the exponential fit of the band-edge region serves as the visual guidance.

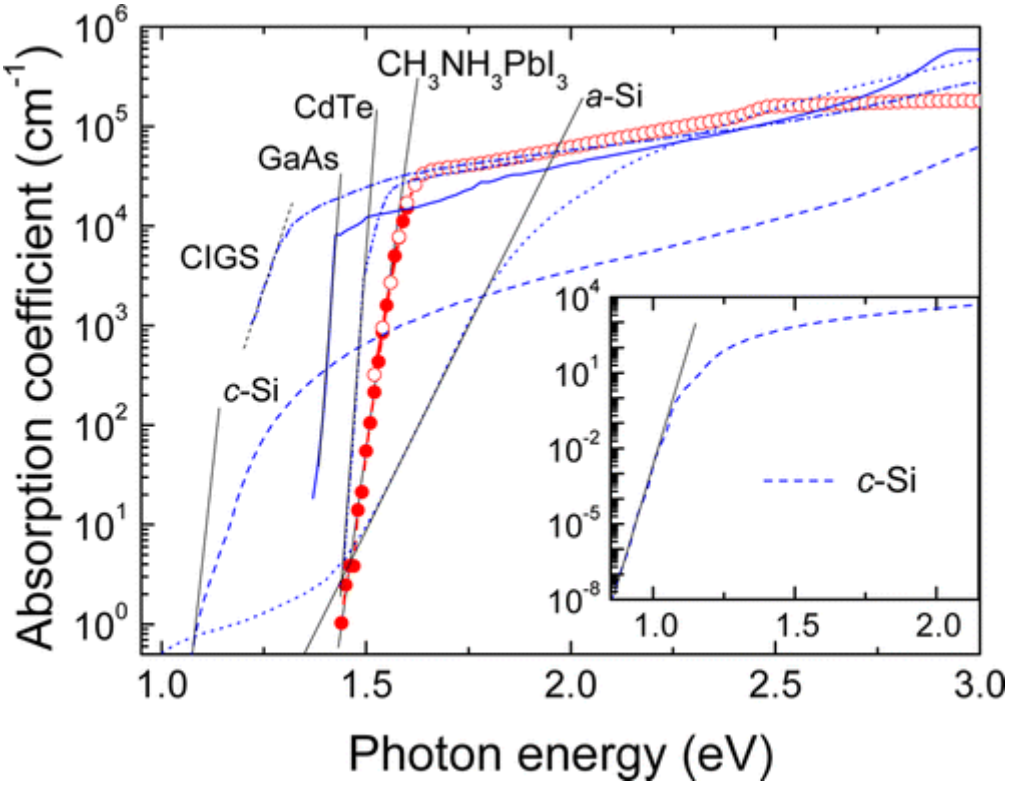

Figure 3-8 The room-temperature effective absorption coefficient of a $CH_3NH_3PbI_3$ perovskite thin film compared with other semiconductors, including amorphous silicon (a-Si), GaAs, CIGS, CdTe, and crystalline silicon (c-Si). For each material, the slope of the Urbach tail is shown. For clarity, the inset shows the data for c-Si down to lower absorption energy. Image and caption from[165].

3.4.3 Photoluminescence measurements

The fraction of photons re-emitted of the photons absorbed decides the photoluminescence quantum efficiency (PLQE) of materials. To quantify the PLQE, the method proposed by J. de Mello was used in this work, which is a three-measurement determination with the integrating sphere accessory.[166] This approach is especially suitable for the measurement of thin-film coated samples that do not absorb incident light fully, with a certain proportion of incident light passing through the samples unabsorbed, which requires the integrating sphere for re-distribution and re-collection.

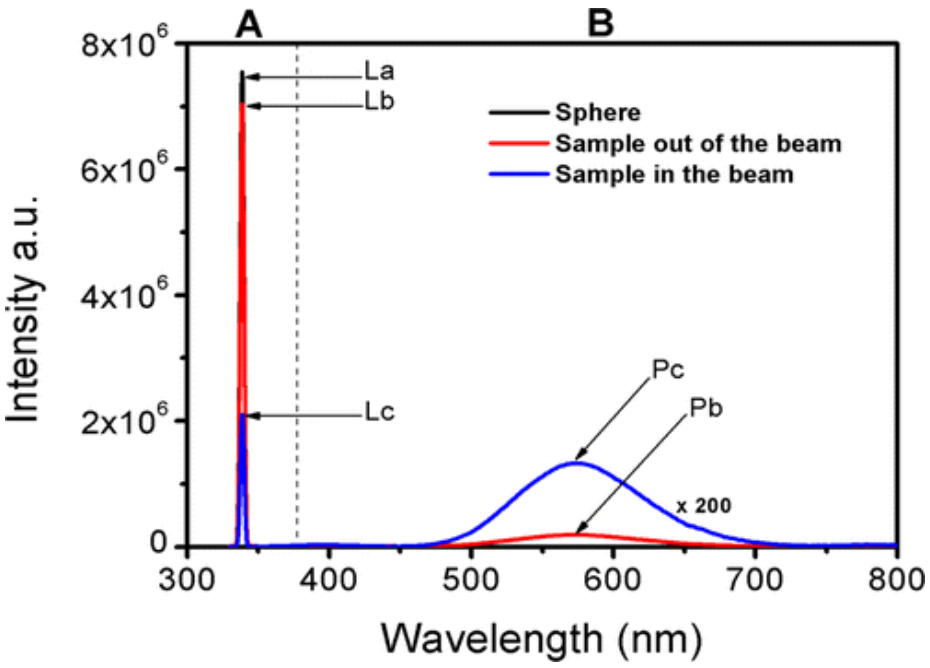

Figure 3-9 Spectra of a three measurement determination of PLQE. Image and caption from E. Coutino-Gonzalez [167]

More specifically, for each sample, we measure three spectra with the setup described above, as illustrated in Figure 3-9. In the first (A), the laser is directed into an empty sphere. In the second (B), the sample is loaded but not directly excited by the laser path. In the third (C), the sample is directly excited.

The number of photons is proportional to the intensity recorded (I), and to determine the number of photons due to the laser (L) or the photoluminescence (P), we integrated under the curve. We can then calculate the PLQE from the equation in ref. [166]

3.4.4 Grazing-Incidence Wide-Angle X-ray Scattering (GIWAXS)

X-ray diffraction is a technique revealing information about crystalline structures. Incoming X-rays interact with electrons of atoms, and these electrons behave as a second source of emanating waves, scattering intensity is hence decided by the number of electrons for each atom. These waves interfere with each other either destructively or constructively in specific directions following the Bragg's Law:

$$2d \sin\theta = n\lambda ,$$

which creates specific diffraction patterns on the detector plane. The position, order, and shape of these diffraction peaks reveal important crystallographic information of materials. Figure 3-10 shows the Bragg's law, here d is the spacing of the periodic planes (the Miller indices (h,k,l) is used to describe the plane orientation), while θ is the incident angle. The integer n is the diffraction order index, and λ is the wavelength of the incoming beam. Conventionally, the scattering vector q is used instead of angle θ, which is calculated from

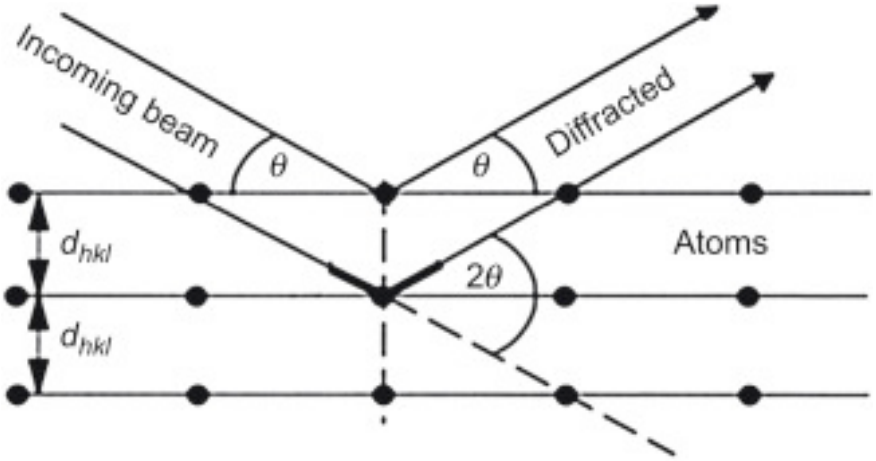

Figure 3-10 Illustration of X-ray diffraction. Image and caption from J. Epp [168]

$$q = \frac{4\pi \sin(\theta)}{\lambda},$$

then the relationship between q and d could be derived as:

$$q_{hkl} = \frac{2\pi}{d_{hkl}},$$

however, most conjugated polymers have a significant structural disorder and hence do not form extended crystalline structures within thin films, but form semi-crystalline or amorphous microstructure instead[52]. Therefore, calculating the unit cells of these materials is impossible in most cases[51].

3.4.5 Small Angle Neutron Scattering (SANS)

In terms of its basic property, the charge of a neutron is 0, and it interacts mostly with nuclei within femtometre-range short distances. Since nuclei only occupy a negligible volume of atoms, most materials are significantly more transparent to neutrons than to electrons, and hence neutrons are more "penetrating" compared with electrons, making it suitable for the characterization of bulk samples or solutions with certain optical path lengths (on the order of mm to cm).

In order to quantify the nature and intensity of interaction between neutron and nuclei, a parameter called nuclear scattering length b is proposed, while a negative/positive value of b represents an attractive/repulsive neutron-nuclear interaction, the amplitude of b represents the interaction intensity. Interestingly, isotopes may have different signs and values of b, for example, hydrogen and deuterium have scattering lengths of -3.74×10^{-5} Å and 6.67×10^{-5} Å respectively, hence deuterated solvents, when combined with non-deuterated polymers, could provide the important scattering contrast and hence get rid of the influence of solvents to investigate the morphology of isolated polymer chains, which is a key advantage of the neutron scattering technique compared with X-ray scattering techniques[142]. Based on b, a more intuitive parameter called scattering cross-section $\sigma = 4\pi b^2$ could be derived to quantify how "large" the incident neutron "feels" the nucleus. There are two different kinds of scattering happens during the SANS experiments: the coherent, elastic scattering of radiation produces interference, which contains structural information of materials, while the incoherent scattering merely contributes to the scattering background. Not like wide-angle scattering providing information about "internal structure" read out from the position and shape of Bragg peaks, small-angle scattering provides information about more averaged, mesoscopic structural features such as the size and shape of particles.

SANS experiments were carried out using the Sans2D instrument at the ISIS Facility, Rutherford Appleton Laboratory, the United Kingdom. As a time-of-flight instrument, Sans2D uses the neutrons with an incident wavelength of 2.0 - 14.0 Å at 10 Hz.

The polymers were dissolved into a deuterated solvent (dichlorobenzene-d4, DCB-d4) with a concentration of ~ 5 mg/mL. The sample to detector distance is 8 m, which results in a q range of 0.006 $Å^{-1}$ ~ 0.45 $Å^{-1}$ (where q is the scattering vector $q = 4\pi \sin(\theta)/\lambda$, 2θ is the scattering angle). The initial 2-dimensional scattering patterns were corrected for the background signal and the detector response, and then reduced to 1-dimensional intensity plots of absolute scattering cross-section (in cm^{-1}) using standard procedures[169].

For a mono-disperse collection of particles, the scattering cross-section can be written as:

$$I(q) = \phi V \Delta\rho^2 P(q) S(q),$$

where ϕ is the volume fraction of the particle, V the volume of the particle, $\Delta\rho$ is the scattering length density difference between the particle and the solvent, $P(q)$ is the particle form factor and $S(q)$ is the structure factor. The $P(q)$ describes the structure of the particles and equals unity at $q = 0$. The structure factor describes the interferences of scattering from different particles and contains information on the interaction between the particles. For experiments on dilute systems (the cases for this work), $S(q)$=1 and can be neglected. In addition, due to polydispersity within conjugated polymers, the size distribution of polymer chains usually must be considered as well, which tends to "smear out" sharp features or turning points of scattering patterns.

3.4.6 High resolution scanning tunnelling microscopy (STM)

Scanning tunneling microscopy (STM) images were obtained by using a combined electrospray deposition (ESD) and variable temperature STM system operated in an ultrahigh vacuum (UHV). Epitaxial Au(111) layer on mica films (Georg Albert PVD, Heidelberg, Germany) were used as substrates and cleaned prior to ESD by repeated cycles of Ar^+ sputtering (ion current density of ~3 $\mu A/cm^2$ with 1 keV ion energy) and

annealing (temperature 450 °C, time 12 mins). Solutions for ESD were prepared by dissolving polymers in a composite solution made of toluene and methanol (with a volume ratio of 4:1 and concentration of ca. 0.1 mg/mL). These NN1 solutions were electrosprayed (UHV4iH ultra-high vacuum compatible electrospray deposition setup, Molecularspray Ltd.) onto pre-cleaned, atomically flat Au (111) surface with a total deposition charge of 9 pA.h. STM measurements were conducted using a variable temperature (temperature range 90K – 1000°C) STM (Aarhus 150 HT) under ultrahigh vacuum (~5×10^{-10} mbar). Images were acquired at −150 °C in constant-current feedback mode, with typical sample bias (V_{bias}) of −1.8 V and tunneling currents of 40 pA. The Gwyddion software[170] was used to analyze the images. Details of the experimental procedure have been described previously[171].

3.4.7 Dynamic mechanical analysis (DMA)

A Triton 2000 DMA, in combination with a material pocket accessory, was used to conduct all DMA measurements shown in the work. 8 mg polymer powder were enveloped within the metal pocket and mounted in the DMA. Single cantilever bending mode was chosen as the deformation mode. Displacement was set as 0.05 mm; compared with the 10 mm length sample dimension it was well within the linear viscoelastic response (LVR) region[172], within which the resultant stress responds linearly to the applied strain, and deformation of sample could completely recover after the removal of the applied strain without damage of sample to any extent. Two frequencies of 1 Hz and 10 Hz were set for the temperature sweep mode measurement, with a ramp rate of 3 °C/min, from -100 °C to 350 °C. Within this temperature regime, β, α, and melting process happens sequentially during temperature increase, while the highly localised and subtle structural relaxation occurs during the γ transition (happens at even lower temperature than the β transition, not within the temperature range of our experiments), and its potential impact on materials' electronic and optoelectronic performance, is not the focus of this study. During experiments, a sinusoidal strain

within the linear viscoelastic region (LVR) is applied to the sample clamped through the periodic movements of the driveshaft, whilst measuring the mechanical response (resulting stress) as a function of both oscillatory frequency and temperature. Within the LVR region, relatively small strain amplitude is applied, hence the sample would not be destroyed during experiments. Recently, this technique demonstrates its capacity for broader applications such as measuring powdered materials with pharmaceutical and biomedical significance with the help of material pocket accessory (folded sheets of stainless steel)[147][173]. Material pockets envelop and reinforce the polymer in order to measure these powdered materials with DMA. During measurements, polymer powders are sheared periodically within the material pockets. Hence to a certain extent, DMA measures the response of polymer powders under interchain friction directly. However, due to the unclear sample geometric, the accurate modulus of the materials could not be measured directly, which is a drawback of the material pocket approach. In other words, the much stiffer and heavier stainless steel pockets (750mg for each) would dominate modulus signal, masking the much weaker signals from lighter (8 mg polymer powder used each time) and softer polymer powders. However, the temperature at which a specific relaxation happens would still induce a detectable peak in the "joint" damping factor or loss modulus of the material pocket enveloped sample (MPE sample), due to the ultra-sensitivity intrinsic to the setup's working mechanism. Since stainless steel has no structure relaxation within the measured temperature regime (-100 to 350 °C within this work)[147], the mentioned features could be unambiguously correlated with specific relaxation processes of the target polymer enveloped. In other words, the trend of the modulus or damping factors, such as peaks in the curves, could still be related to the change of polymers' mechanical property at relaxation.

4. Materials characterization and device optimization of fused polymers

Unlike inorganic semiconductors for which delocalized electronic states and band structures stem from long-range crystallinity within atomic lattices the charge transport and optoelectronic properties of conjugated polymers are largely determined at the single molecular level by the conformation of the polymer backbone, which governs the ability of the π-conjugated electronic states in the frontier molecular orbitals to delocalise along the polymer backbone. A distribution of different conformations adopted across the network of polymer chains in the solid state is also responsible for energetic disorder and broadening of the electronic DOS. Key factors that characterize or determine the chain conformation include backbone planarity[29], backbone deflection angles[174], torsional potentials[174] and persistence length[175]. Characterisation of molecular level chain conformations[174–176] is arguably the starting point for understanding structure-property relationships [33,51,52] in specific conjugated polymer systems.

In recent years the persistence length, which is a measure of the length scale over which the polymer backbone changes its direction, has been uncovered to intimately correlate with the materials' electronic and optoelectronic characteristics, and a long persistence length has been demonstrated to be desirable for applications such as high-efficiency organic photovoltaics and high mobility organic field-effect transistors (OFETs)[175]. Examples of the importance of persistence length include studies of the photoluminescence quantum yield of polyphenylene vinylene derivatives, which were found to be positively correlated with the persistence length and stiffness of the backbone[177]. Unusually high optical absorption in specific donor-acceptor (D-A) conjugated polymers have been ascribed to long persistence length as well[79]. Already from early studies it has been known that persistence length is related to the degree of conformational and energetic disorder[178]. Stiffer chains not only reduce the number of possible backbone configurations and hence energetic disorder[134][179], but also provide straight tie chains bridging neighbouring crystallites, forming efficient percolation

pathways required for macroscopic charge transport within thin-film devices such as OFETs[38].

One of the factors that limits the persistence length of traditional conjugated polymers is the existence of single-bond linkages that connect rigid conjugated units along the polymer backbone. At these single-bond linkages cis–trans isomerism or variations of the torsional angle between neighbouring conjugated units can occur that limit π-electron delocalisation and may change the orientation of the backbone. As a result most conjugated polymers exhibit limited chain rigidity with random coil or worm-like conformations on length scales above 1-10 nanometers[175] and more flexibility compared with other π-conjugated systems such as carbon nanotubes[180]. To date the conjugated polymers with the longest persistence lengths have been found to be donor-acceptor copolymers with extended, fused-ring conjugated units linked by single bonds designed to exhibit steep torsion potentials[29][79]. In such rigid and low disorder polymers the highest carrier mobilities on the order of 1-5 $cm^2V^{-1}s^{-1}$ have been observed in polymer-based OFETs to date. A wide range of such donor-acceptor polymers have been investigated to date, but at present there are no clear molecular design guidelines that would allow going beyond the level of performance that is achievable with such systems and for the last five years there has been only gradual and slow progress in the performance of conjugated polymers for OFETs.[77,181–183] There is an urgent need for new design motifs for conjugated polymers that might allow further reductions in mainchain conformational flexibility and energetic disorder.

Recently, an aldol condensation reaction between bis-isatin and bis oxinddole monomers has been used to synthesize an unusual series of electron-deficient conjugated polymers with completely fused backbone structures that do not contain any single-bond linkages[75]. These polymers comprise fused ring units that are linked together by double as opposed to single, carbon-carbon bonds. Because the energetic barrier for rotation around a double bond is expected to be an order of magnitude higher than for rotation around a single bond[75], we expect these polymers to have a more rigid backbone with potentially longer persistence lengths. In one such polymer, a

homopolymer based on naphthalene-derived monomers, referred to as NN2 within this work, a high electron affinity (EA) of 4.2 eV and air-stable electron transport for up to 300 hours were observed within OFETs with μ_{FET} of 0.03 $cm^2V^{-1}s^{-1}$.[75] Given the unique nature of the backbone of these polymers this level of achievable μ_{FET} is maybe somewhat disappointing. However, to date a detailed study of the structure property relationships and charge transport physics of this class of polymers has not been reported yet and it is important to understand the polymer chain conformations that these polymer adopt and the factors that limit their charge transport properties.

In this work, we systematically investigate the chain conformations, persistence lengths, microstructure, energetic disorder and charge transport properties in several such polymers. Compared to the polymers included in our previous work[75], including NN1, we designed derivatives in which the branch-point is moved further away from the backbone [43][158] to promote crystallinity and we adopted also a copolymer design with some units extended from a naphthalene to an anthracene core to extend the conjugated backbone[152]. We present a full characterisation, including the molecular weight dependence of charge transport properties as well as film microstructure by grazing-incidence wide-angle x-ray scattering (GIWAXS) and quantification of energetic disorder by the PDS technique. We show that optimisation of molecular design provides access to electron mobilities of 0.5 $cm^2/V^{-1}s^{-1}$, that are significantly higher than observed previously in this class of polymers and comparable to those of other state-of-the-art n-type conjugated polymers, such as the widely investigated n-type polymer p(NDI2OD-T2)[49].

4.1 SANS experimental results of NN2 polymer

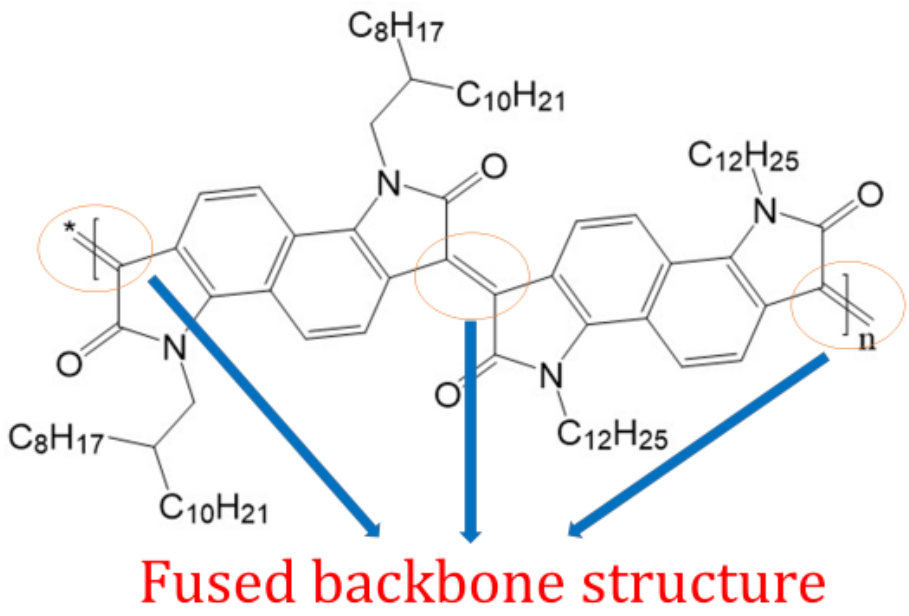

Figure 4-1 Fused backbone structure of NN2 polymer

Electronic performance of conjugated polymers emerges from their microstructure properties. The unique double-bonding fused backbone structure provides the possibility for longer persistence length and a more rigid polymer chain structure of fused polymers compared with traditional conjugated polymers (Figure 4-1). Hence it would be very helpful to confirm the backbone rigidity experimentally. In this work, small-angle neutron scattering is carried out by our collaborators to investigate the backbone rigidity and estimate the persistence length of NN2 polymers directly.

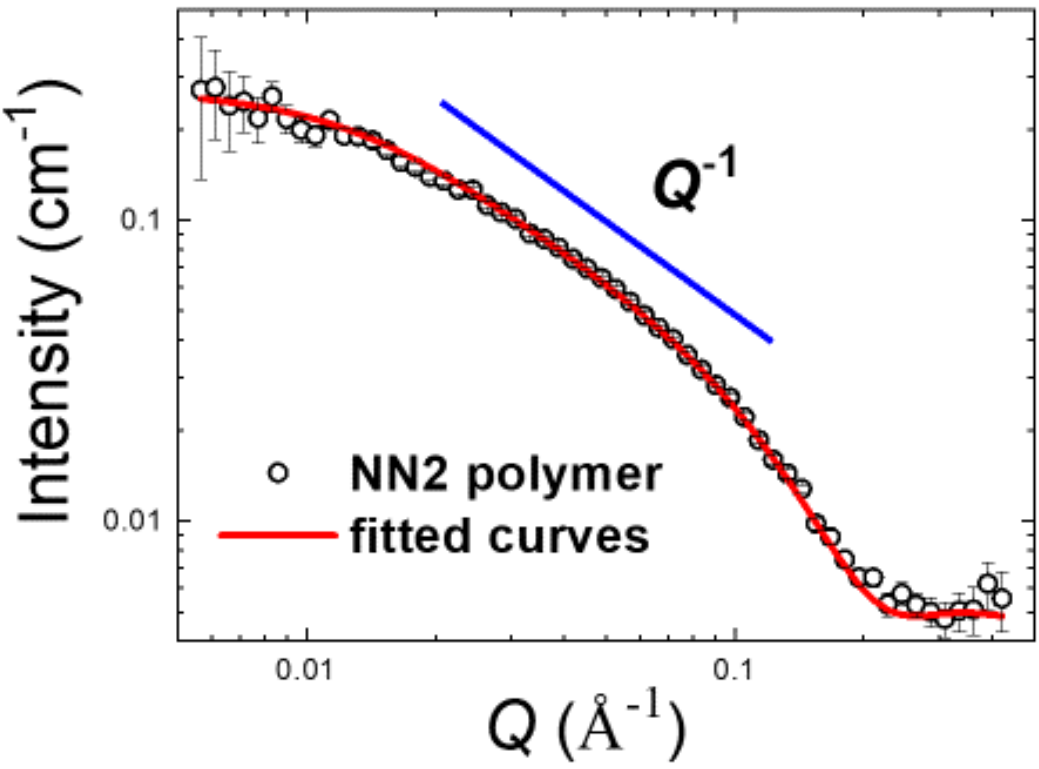

Figure 4-2 SANS plots for NN2 polymer (SANS experiments performed by Professor Guoming Liu and Yutian Wu, data analysis performed by Professor Guoming Liu).

Figure 4-2 shows the scattering cross-section of the polymer. A rapid decrease in scattering intensity can be seen for large scattering vectors above 0.1 Å^{-1}. The sharp decrease of intensity at high Q corresponds to a cross-sectional Guinier behavior. For intermediate scattering vectors in the range between 0.01 Å^{-1} and 0.1 Å^{-1} the scattering intensity decreases approximately as $I \propto Q^{-1}$, which agrees with a rod-like object. Below 0.01 Å^{-1}, we observe a gradually weaker dependence of intensity on Q, such plateau at low Q corresponds to the Gunier region. Those features of scattering agree well with a rod with a finite length. If the chain adopts a rod-like conformation, the length L is proportional to the molecular weight (MW). The form factor of randomly oriented cylinders is[184]:

$$P(Q) = \frac{scale}{V}\int_0^{\pi/2} F^2(Q,\alpha)\sin(\alpha)\,d\alpha + \text{background},$$

where,

$$F(Q,\alpha) = 2(\Delta\rho)V\frac{\sin\left(\frac{1}{2}QL\cos(\alpha)\right)}{\frac{1}{2}QL\cos(\alpha)}\frac{J_1(QR\sin(\alpha))}{QR\sin(\alpha)},$$

where α is the angle between the axis of the cylinder and Q, V is the volume of the cylinder ($V = \pi \cdot r^2 \cdot L$), L is the length of the cylinder, R is the radius of the cylinder, and $\Delta\rho$ is the scattering length density difference between the cylinder and the solvent. J_1 is the first-order Bessel function[185]. The fitting curve is included in Figure 4-2. Reasonably good agreement between the fitting curve and the experimental data points is seen. Structural parameters are obtained: R = 14.8 Å and L = 200 ± 100 Å. The length L is expected to be the contour length of the chain. According to the GPC results (M_n = 16 800 g/mol, measured by Professor Guoming Liu from ICCAS, China), the number of monomer per chain is ca. 12. The repeat length per monomer is estimated to be ca. 2 nm (MMFF94 Force Field[186–190]), therefore the contour length of chains is ca. 24 nm. The SANS results fully confirm the rigid rod nature of the polymer chains of NN2 polymers.

4.2 Air-stability of NN2 OFETs

Transition metal free Aldol polymerization was used to synthesize fused polymers. The basic characteristics of these fused polymers are high electron affinity(EA) and low bandgap[75], which make these polymers ideal candidates for air-stable electron transport.

For the NN2 polymer, it has a high EA of 4.2 eV[75], much higher than the previous reported, well-studied polymer P(NDI2OD-T2). To study the charge transport properties of this material together with its air-stability, we carefully fabricate TGBC OFETs with ca. 400 nm PMMA as dielectrics and 20 nm aluminum gate layer. The channel dimension used for these OFETs is the channel length L = 20 μm and the

channel width W = 1mm. The pristine device's characteristics are shown below in Figure 4-3:

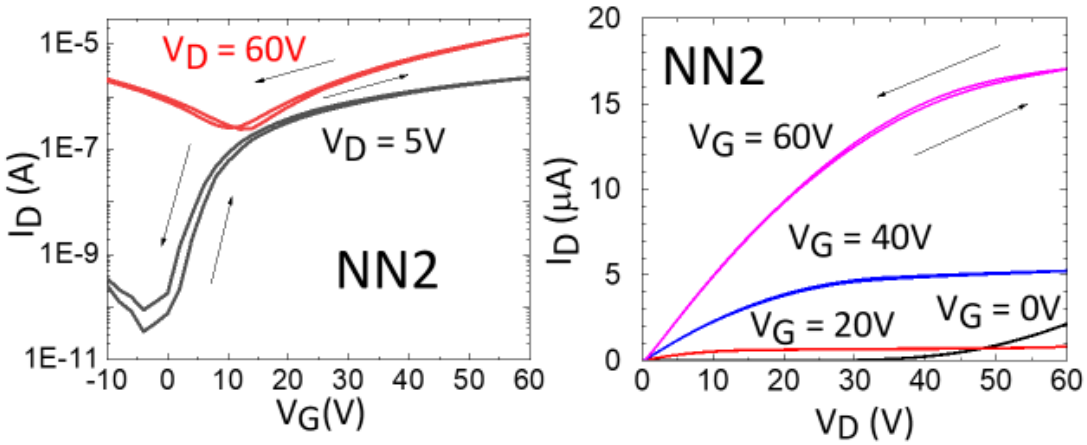

Figure 4-3 (left) transfer characteristics and (right) output characteristics of pristine NN2 TGBC OFETs (L = 20 μm, W = 1mm) measured in a nitrogen atmosphere.

For the saturation transfer curves, the device shows n-channel behaviors predominately at positive gate voltage when electrons are accumulated at the OSC-PMMA interface. However, due to the low band-gap of this polymer, p-channel behavior at negative gate voltage also manifests. Such typical ambipolar behavior makes the device lacking a well-defined turn-off. While for the linear transfer curves, cleaner n-channel behavior could be observed with a current modulation of > 10^4. Significant hysteresis is observed for NN2 devices, which implies that trap states exist either in the bulk of semiconductor or at the semiconductor-dielectric or semiconductor-electrodes interface.

To investigate the air-stability of these NN2 OFETs, we stored the samples in air and did the device characterization in the air as well. The air-stability test is also bench-marked with the well-studied n-channel polymer P (NDI2OD-T2).

From Figure 4-4, it could be observed that the NN2 polymer demonstrates impressive air-stability. The threshold voltage shift happens during the ca. 300 hours of air exposure. However, the electron transport property largely remains, holding the currents and mobility values around the same order of magnitude compared with the pristine device.

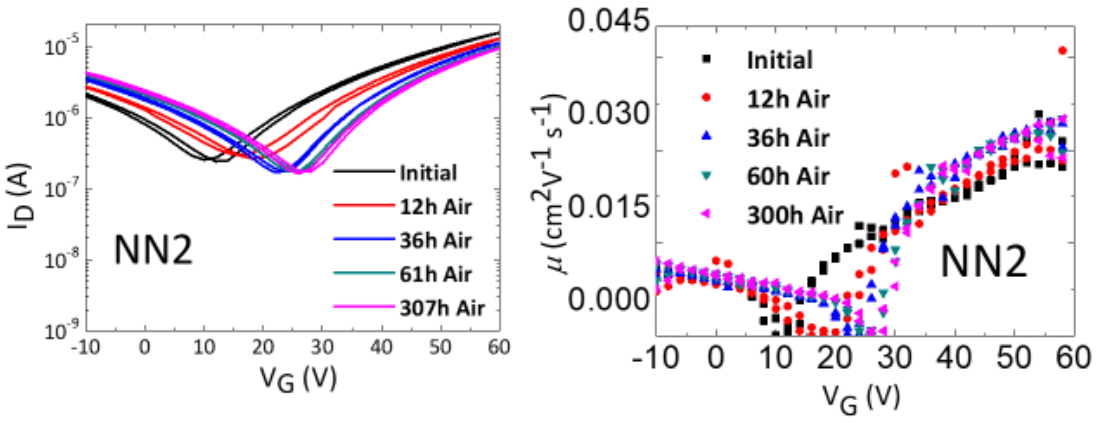

Figure 4-4 The changes of (left) saturation transfer curves and (right) saturation mobilities of pristine NN2 TGBC OFETs (L = 20 µm, W = 1mm) during air-exposure up to ca. 300 hours. The sample was stored in air and re-measured in air.

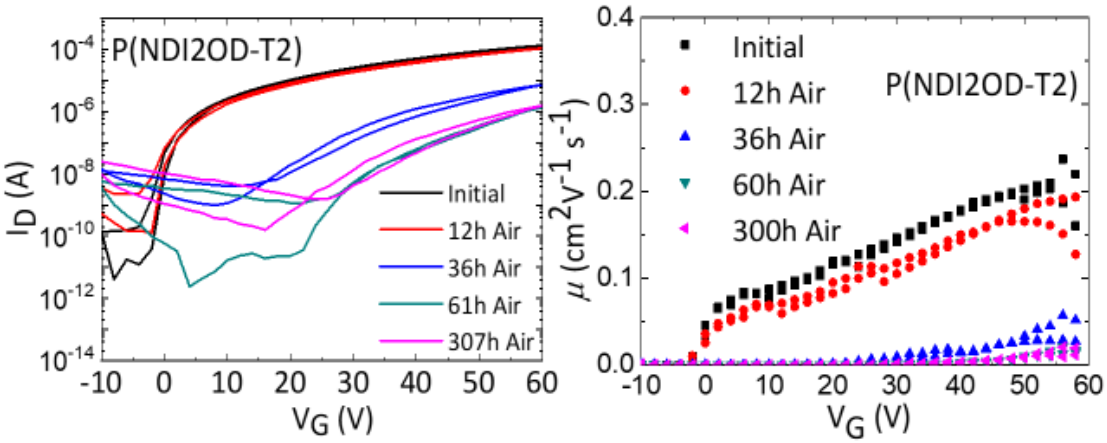

Figure 4-5 The changes of (left) saturation transfer curves and (right) saturation mobilities of pristine P(NDI2OD-T2) TGBC OFETs (L = 20 µm, W = 1mm) during air-exposure up to ca. 300 hours. The sample was stored in air and re-measured in air.

Compared with NN2, the bench-mark P(NDI2OD-T2) shows significantly worse air-stability, as shown in Figure 4-5. The electron mobility drops by more than one order of magnitude after exposure to air for 307 hours, together with significantly

reduced saturation mobility. The possible explanation for this may be due to the lower kinetic barrier for the diffusion of environmental species into the device or lower EA of P(NDI2OD-T2), rendering electron-transport process less stable compared with NN2.

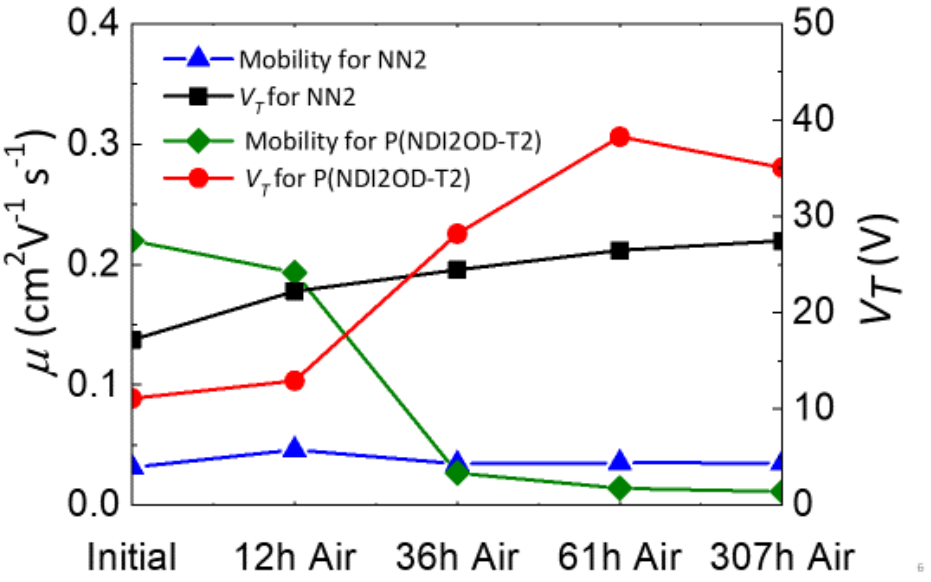

Figure 4-6 Saturation mobilities and threshold voltage changes during air exposure.

To see the effects of air-exposure more clearly, we present the saturation mobility and threshold voltage changes during the 300 hours air-exposure process (Figure 4-6). While the mobility of NN2 retained a similar level (around 0.03 $cm^2V^{-1}s^{-1}$) after 300 hours air-exposure, and the threshold voltage shift from 18 V to 27 V. However, for the bench-mark P(NDI2OD-T2) device, much more significant degradation happened, with the threshold voltage changed to 35 V after air-exposure and mobility dropped to 0.01 $cm^2V^{-1}s^{-1}$. These results clearly demonstrated that NN2 has higher environmental stability compared with P(NDI2OD-T2).

4.3 Activation energy calculation of NN2 OFETs

Temperature-dependent measurements are carried out to derive the activation energy of NN2 OFETs. Transfer curves are taken from 200K to 340K with 20K as a

step. Saturation transfer curves are shown in the left of Figure 4-7. The transistor current for both electron and hole transport decreases monotonically with decreasing temperature, but the shape of the ambipolar transfer characteristics does not change, which suggests that electron and hole transport exhibit similar activation energies. Because of the issues with hole contact injection we focus on a discussion of electron transport here. It is also clear that the ambipolar turning point did not move during the temperature change, showing that the temperature dependent mobilities are accurate characterization of charge transport property rather than artefacts caused by issues like contact resistance. Significant temperature activation behaviour was observed, with an activation energy for saturation mobility calculated to be 102 meV, as shown in the right of Figure 4-7. Interestingly, hysteresis is also significantly reduced at the higher temperature, which could be due to thermally activated trap passivation. With the consideration that PMMA dielectric is prone to induce larger dipolar disorder compared with other lower dielectric constant materials like Cytop[32], the activation energy is well-within the range of those of high-performance semicrystalline polymers[33].

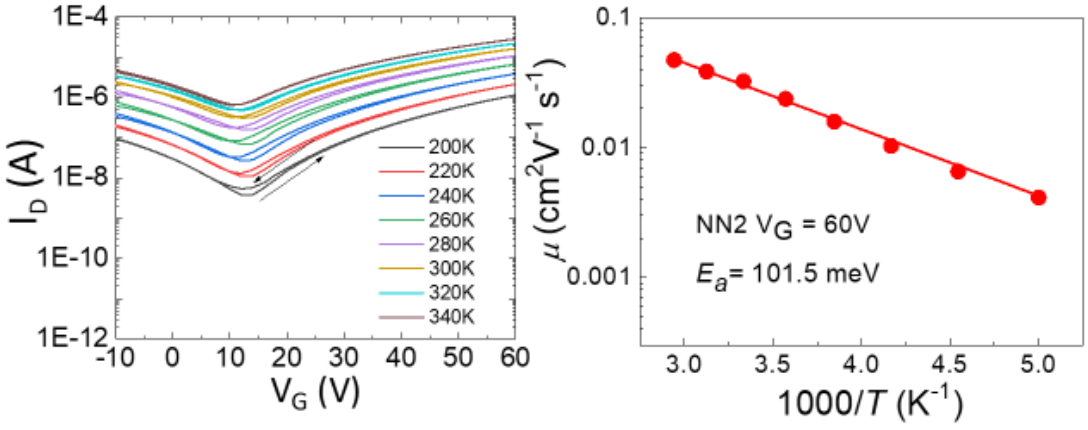

Figure 4-7 (left) Temperature dependent saturation transfer curves and (right) temperature dependent saturation mobilities and activation energy extraction of NN2 TGBC OFETs (L = 20 µm, W = 1mm) with PMMA dielectric.

4.4 Contact resistance optimization of NN2 OFETs

Due to the mismatch of the work function of gold and the EA of NN2 polymer, electron injection/extraction into/out of electrodes might be the bottle-neck of the device performance. Here we investigate this effect by optimizing the device's performance with the modification of an additional injection layer.

For the output curves of NN2 devices, near V_D = 0V, sigmoidal contact artefact manifests to a certain extent, as demonstrated in Figure 4-8(b). Also, from Figure 4-8(c), it is clear to see that the linear and saturation mobility does not overlap with each other, which is another indication of the possible existence of significant contact resistance of NN2 OFETs with standard gold electrodes.

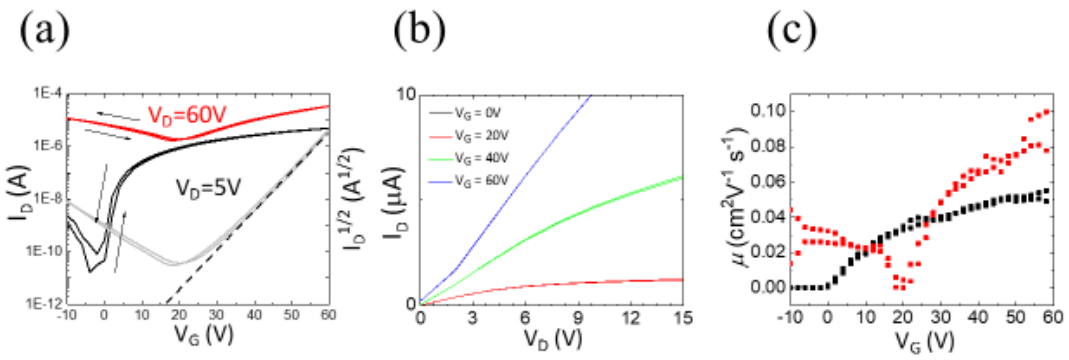

Figure 4-8 (a) transfer curves, (b) output curves, (c) mobilities of NN2 TGBC OFETs(L = 20 μm, W = 1mm) with standard gold electrodes.

To optimize the electron injection property of NN2 OFETs and reduce the contact resistance of related devices, we use a sputter-coated ITO layer on top of gold to modify the work function. In Figure 4-9 **错误!未找到引用源。**, we show the device architecture of related OFETs. In Figure 4-10, it is clear that the contact resistance reduces significantly, manifest as reduced threshold voltage and better overlap of linear and saturation mobilities. This is likely due to the lower work function of ITO (4.4 eV) compared with gold (5.1 eV), which provides a more matched energy level for electron injection from electrodes into OSCs (LUMO level of which around 4.2 eV). In the

future, other air-stable electron injection layers[191] could be used to optimize device performance further.

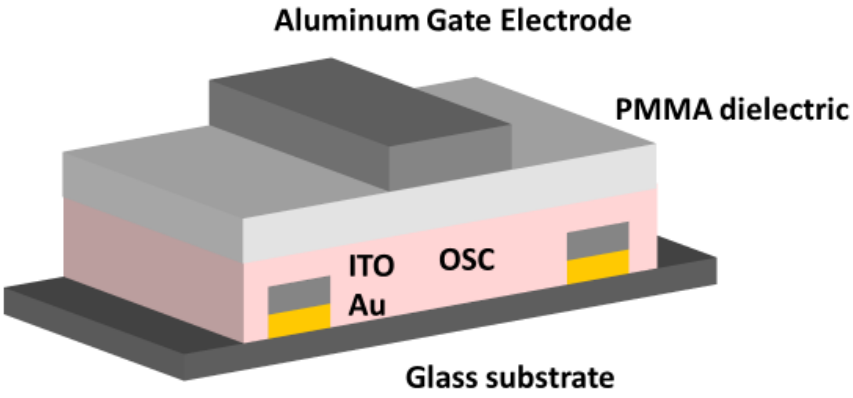

Figure 4-9 The device architecture of a TGBC OFET with ITO modified gold electrodes. ITO sputter-coating performed by Shijie Zhan at the Department of Engineering, the University of Cambridge.

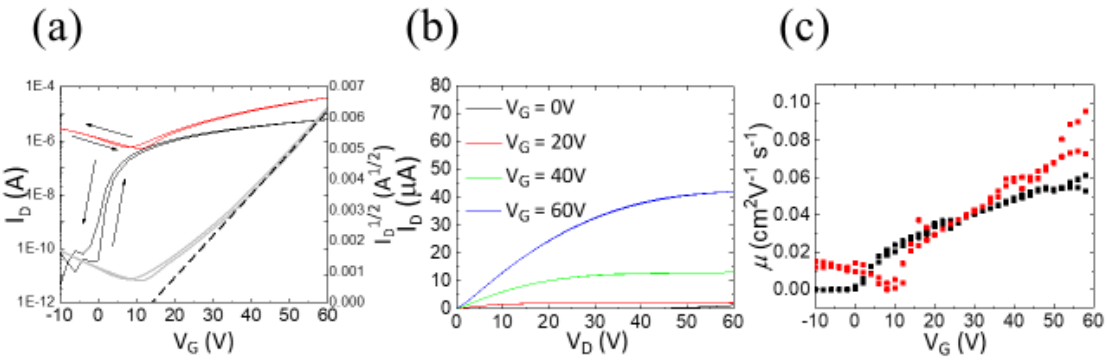

Figure 4-10 (a) transfer curves, (b) output curves, and (c) mobilities of NN2 TGBC OFETs (L = 20 μm, W = 1mm) with ITO modified gold electrodes. ITO sputter-coating performed by Shijie Zhan at the Department of Engineering, the University of Cambridge.

4.5 Side-chain optimization of NN2 polymers

Side-chain engineering has been used to improve the performance of NN fused polymers. Starting with the NN2 polymer, different lengths of linear side-chains, and

the position of branching points of branched side-chains are adjusted to improve the performance of related OFETs.

4.5.1 Linear-chain lengths study of NN polymers

Five NN polymers with different linear-chain lengths: from NN C8 to NN C16 are characterized. The UV–vis-NIR absorption spectra of all polymers were measured in dilute chlorobenzene solution and thin films, as shown in Figure 4-11. All polymers exhibit almost the same absorption profile due to their identical backbone structures. Three distinct absorption bands from 300 to 1300 nm can be observed, with a broad and high-intensity NIR absorption band, a band in the visible and the highest band in the ultraviolet. The absorption features of all polymers are nearly identical in solution and thin films, suggesting strong preaggregation exists in the solution. For NN C8, NN C10, NN C12, and NN C16, the absorption maximum in the NIR region in solutions are blue-shifted around 4-5 nm when compared with those in their solid states, whereas NN C14 has the opposite phenomenon with a 3 nm bathochromic-shift in the thin film. Interestingly, NN C14 exhibits the longest wavelength absorption maximum around 940 nm both in solution and solid-state.

The ionization potentials (IPs) were measured by the photoelectron spectroscopy in air (PESA) of these thin films. The IPs of NN C8, NN C12, NN C14, and NN C16 were found to be around 5.20 eV, and NN C10 has a little higher IP of 5.27 eV. With the consideration of the optical bandgap (around 1.0 eV), the electron affinity (EA) of polymers were estimated between 4.09 eV and 4.26 eV. These high EA indicates that the polymers are suitable for ambient-stable electron transport.

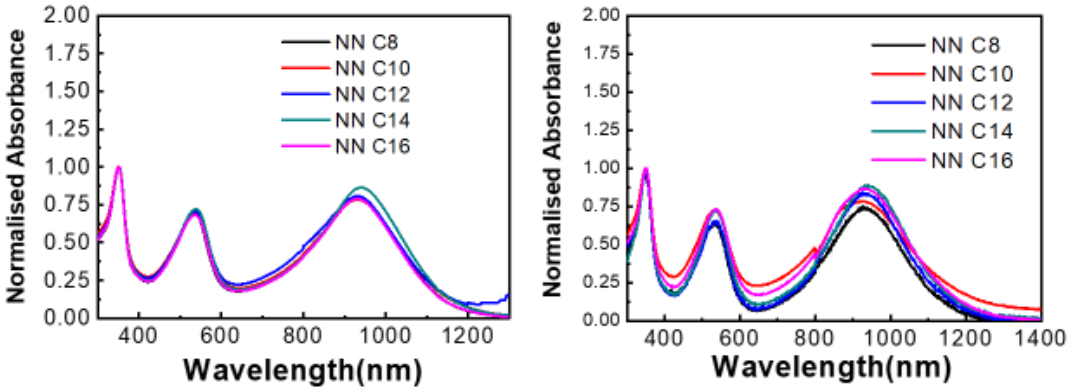

Figure 4-11 Normalized UV-Vis-NIR absorption spectra of NN C8, NN C10, NN C12, NN C14 and NN C16 measured in hot (80 °C) chlorobenzene solutions (left) and thin-films (right). Measurements performed by HaiLiang Liao at SUN YAT-SEN University.

Basic information about these five polymers are summarized in Table 4-1 below:

Table 4-1 Properties of the synthesized polymers.

Polymer	Mn(kDa)[a)]	Mw(kDa)[a)]	PDI [a)]	IP(eV) [b)]	E_{opt} (eV) [c)]	EA(eV) [d)]
NN C8	72	337	4.7	5.2	1.1	4.1
NN C10	27	41	1.5	5.3	1.0	4.3
NN C12	67	266	4.0	5.2	1.0	4.2
NN C14	100	395	4.0	5.2	1.1	4.1
NN C16	41	115	2.8	5.2	1.0	4.2

a) Molecular weights of all polymers were evaluated by gel permeation chromatography (GPC) using chlorobenzene (CB) as eluent at 80 °C; b) Measured by Photo-Electron Spectroscopy in Air (PESA) system; c) Estimated optical gap was calculated using onset of the thin-film (spincoated on glass substrates) absorption spectra ($E_{opt} = 1240/\lambda_{onset}$); d) EA is calculated from

EA = IP−E_{opt}. Measurements performed by HaiLiang Liao at SUN YAT-SEN University and Dr. Hu Chen from KSC, King Abdullah University of Science and Technology (KAUST),

Saturation mobilities extracted from these OFETs are presented below in Figure 4-12. NN C14 demonstrates the highest mobilities within these five polymers. However, since the molecular weights of these polymers are not the same, a direct performance comparison is hard to make.

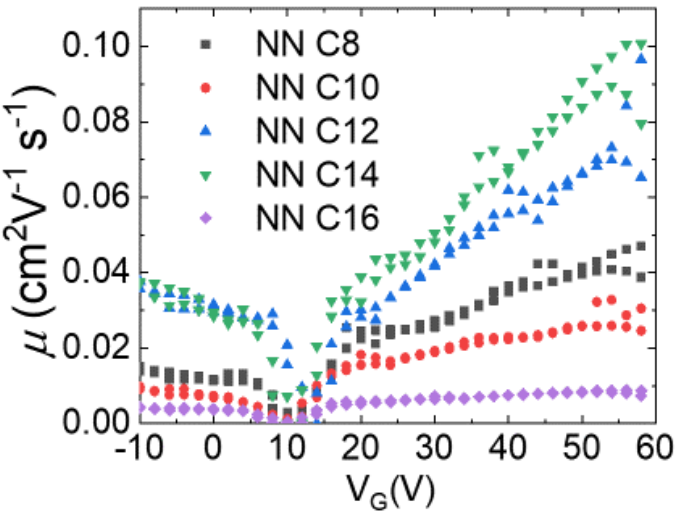

Figure 4-12 Saturation mobilities of NN polymers with different side-chain lengths (measured from TGBC OFETs, L = 20 μm, W = 1mm).

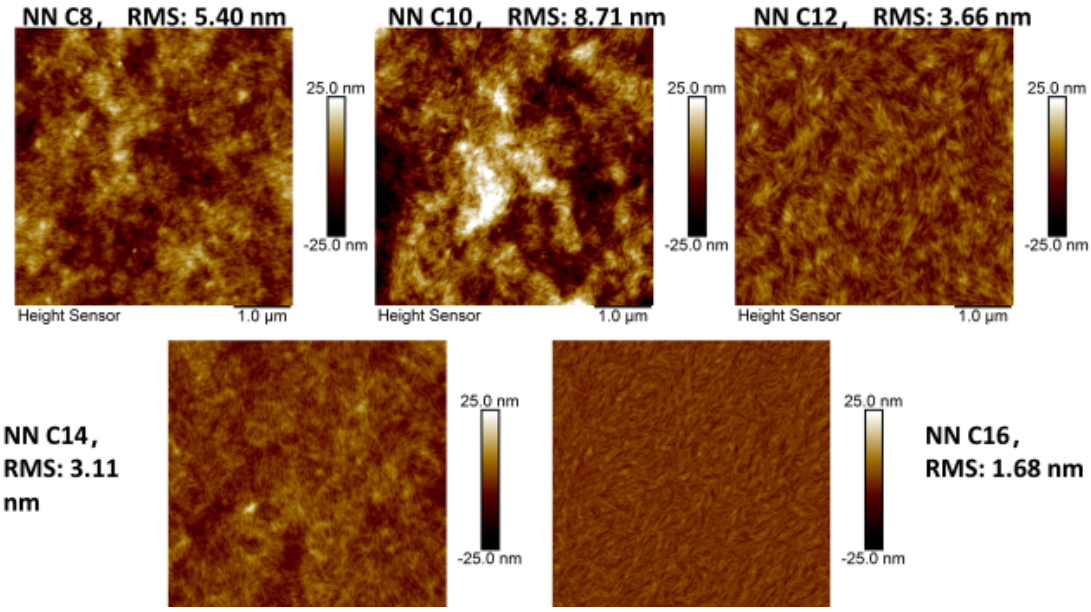

Figure 4-13 AFM images of NN polymers with different linear side-chain lengths. Measurements performed by HaiLiang Liao at SUN YAT-SEN University

AFM images are taken for these five polymers with different linear-chain lengths (Figure 4-13). Strong self-organization of these polymers could be observed from these AFM images directly, which manifests as fibrillar morphologies. Such significant microstructural order could be an important clue to explain the high n-channel field-effect mobilities of related OFETs, especially for the NN C14 device.

4.5.2 The effect of moving side-chain branching point of NN polymer

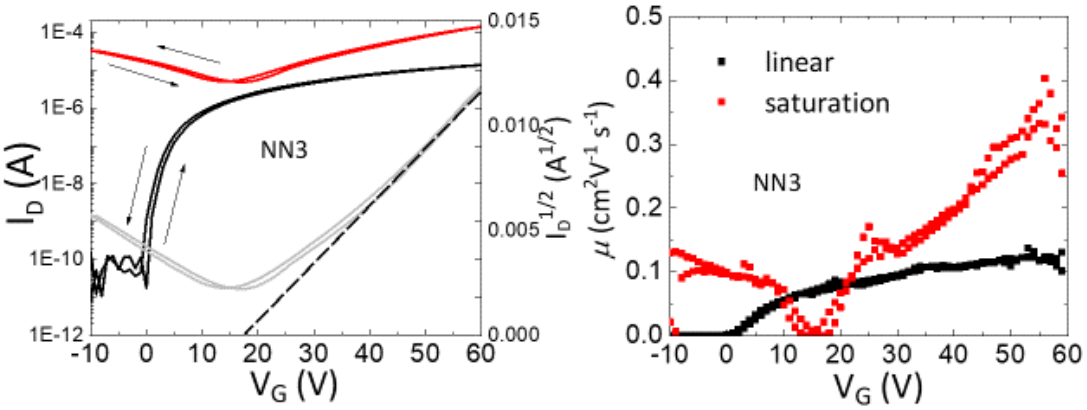

Figure 4-14 (a) Transfer curves and (b) mobility of NN3 TGBC OFETs (L = 20 μm, W = 1mm)

Manipulation of the position of the branching point has proved to be one effective method to increase the crystallinity and solubility of conjugated polymers. Applying the same methodology, our collaborators synthesised the improved version of NN2 polymer, the NN3 polymer. The performance of a representative NN3 OFET is shown in Figure 4-14. Significantly improved mobility compared with the NN2 device (around 0.06 $cm^2V^{-1}s^{-1}$) is observed, showing the successful side-chain strategy.

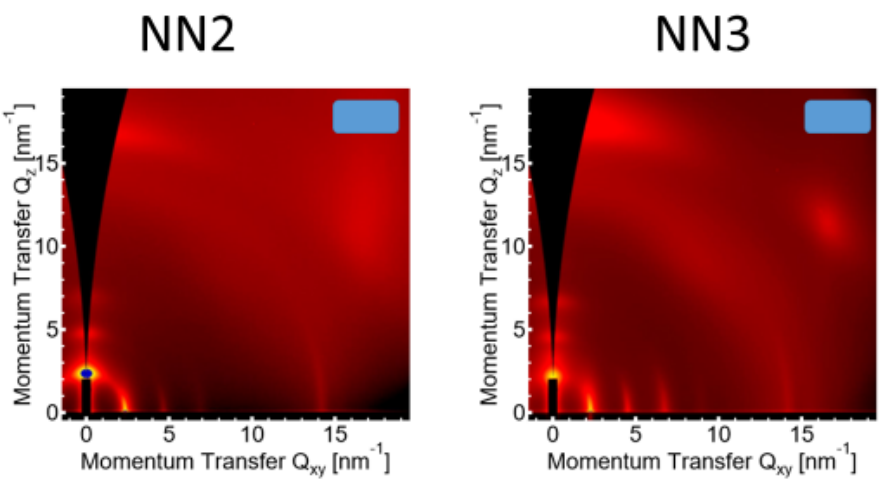

Figure 4-15 2D GIWAXS comparison between NN2 and NN3 polymers. GIWAXS experiments performed by Professor Chris McNeill, Dr. Xuechen Jiao at the Department of Materials Science and Engineering, Monash University.

To understand the microstructural origin of the significantly improved performance of NN3 polymer, we performed and compared 2D GIWAXS for both NN2 and NN3 polymers in Figure 4-15.

Comparing the out-of-plane lamellar stacking, we found that NN3 exhibits stronger higher-order diffraction, especially the out-of-plane (300) diffraction. This suggests that NN3 possesses edge-on crystallites with less paracrystallinity than NN2. Comparing the in-plane lamellar stacking, it is more obvious that NN3 shows a much stronger higher-order lamellar diffraction than NN2. This suggests that NN3 also grows face-on crystallites with higher crystallinity. It could also be observed that NN3 has a more pronounced face-on crystalline structure.

Regarding the edge-on crystallites, although both NN2 and NN3 show the same π-π stacking distance (q=1.42 $Å^{-1}$, d=4.42 Å), the lamellar stacking of NN3 (q=0.23 $Å^{-1}$, d=27.37 Å) is larger than NN2 (q=0.24 $Å^{-1}$, d=26.36 Å). Regarding the face-on crystallites, the lamellar stacking of NN3 (q=0.23 $Å^{-1}$, d=27.37 Å) is still larger than NN2 (q=0.24 $Å^{-1}$, d=26.36 Å). Moreover, the π-π stacking of NN3 (q=1.74 $Å^{-1}$, d=3.61 Å) is significantly shorter than NN2 (q=1.68 $Å^{-1}$, d=3.74 Å). This may facilitate inter-chain stacking and improve interchain charge transport properties significantly, hence explains significantly higher field-effect mobility within NN3 OFETs.

Energetic disorder within materials could be characterized by Urbach energy, to compare the energetic disorder between NN2 and NN3 polymers, we performed PDS measurements and calculated Urbach energy for the materials.

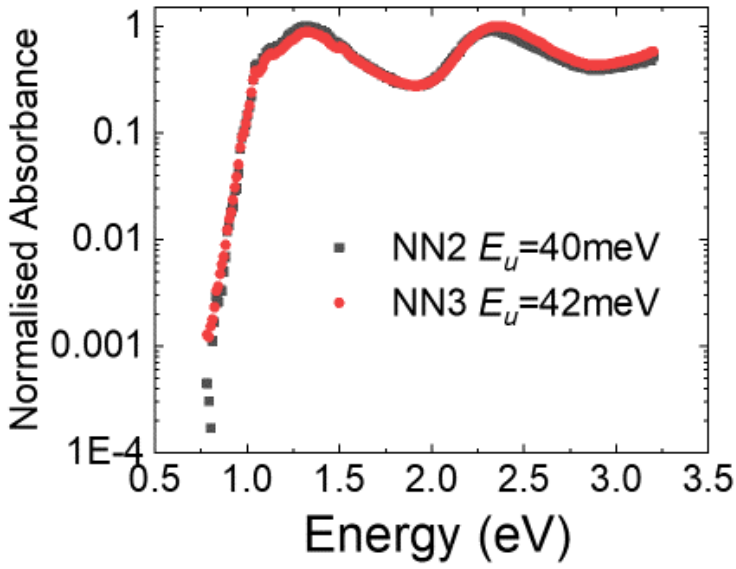

Figure 4-16 Urbach energy comparison between NN2 and NN3 polymers. PDS measurements done by Dr. Aditya Sadhanala, Dr. Mojtaba Abdi Jalebi at the Cavendish Laboratory, the University of Cambridge.

From the PDS measurement results in Figure 4-16, the sub-bandgap region of these two polymers shows significant similarity due to the same backbone structure. However, the NN3 polymer, which demonstrates much higher mobility and less paracrystallinity shows slightly higher energetic disorder than the lower mobility NN2 polymer.

To understand the charge transport mechanism of NN2 and NN3 polymers, we performed molecular weight study on these two materials, and plot the relationship between molecular weight and saturation mobilities in Figure 4-17. Interestingly, NN3 polymer not only demonstrates higher mobility but also shows significantly less molecular weight dependence of device performance. With consideration of the GIWAXS data, one possible explanation could be due to improved interchain short

contacts of NN3 compared with NN2, making NN3 less reliant on high molecular weight chains to form effective charge transport networks.

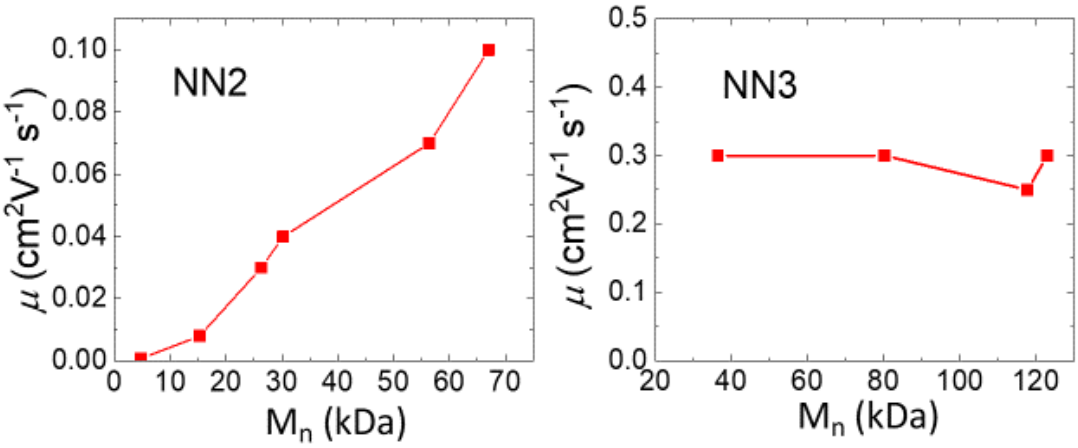

Figure 4-17 relationship between molecular weight and saturation mobility of (left) NN2 polymer and (right) NN3 polymer TGBC OFETs (L = 20 μm, W = 1mm).

4.6 The effect of backbone extension on OFET performance of fused polymers

Backbone extension is also a very effective method to improve the charge transport property of conjugated polymers. Hence the anthracene-co- naphthalene fused copolymer (the AN fused polymer) and the anthracene-co-anthracene fused copolymer (the AA fused polymer) are synthesized by our collaborators to investigate their charge transport behaviours.

4.6.1 Characterization of AN polymer

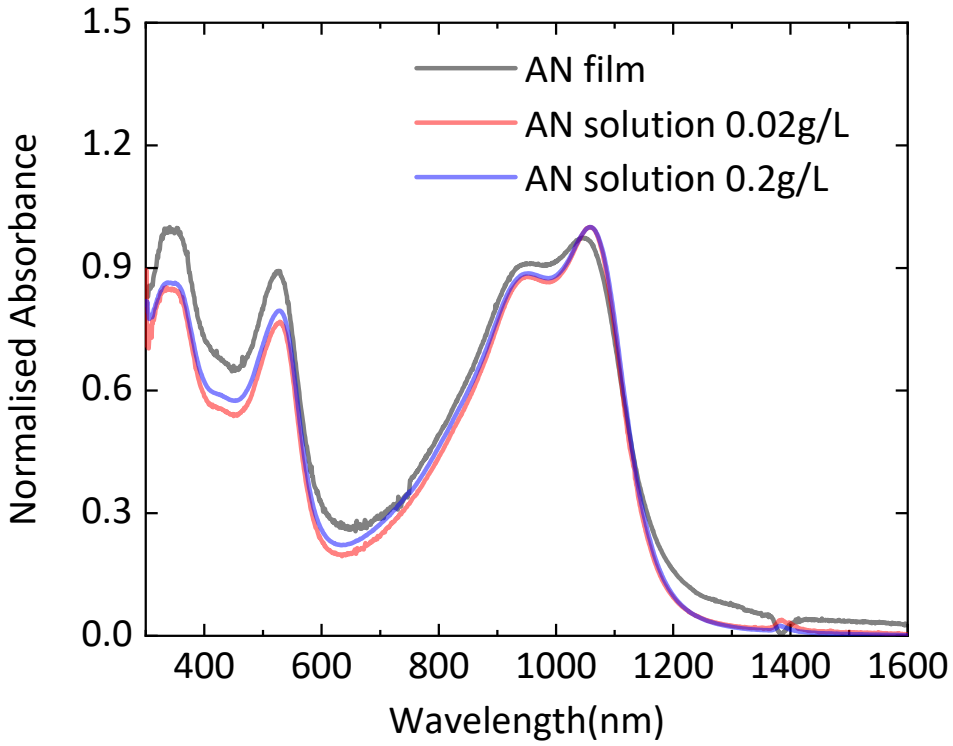

Figure 4-18 The thin-film and solution UV-Vis-NIR absorption spectra of the AN polymer.

High molecular weight (Mn/Mw 147/450 kDa) AN polymer was synthesized by our collaborator Hu Chen in KAUST. Figure 4-18 shows the thin-film UV-Vis-NIR absorption spectra for the AN polymers with wavelengths ranging from 250 nm to 1600 nm. Three absorption peaks appear within this spectral range, one each in the ultraviolet (UV), visible, and near-infrared (NIR). The absorption peaks in the UV and visible bands are observed at similar positions to the NN polymers in Figure 4-11, namely 355 nm for the UV band and 524 nm for the visible band. However, the longest wavelength absorption in the NIR occurs at a longer wavelength (1047nm) in AN than in NN1 and NN2 (930nm). Also, AN is the only polymer in which it is possible to observe a well-resolved 0-0 and 0-1 vibronic progressions in the NIR band, suggesting a smaller degree of energetic disorder. Thin-film and solution absorption spectra are quite similar for the AN polymer; however, for AN, the ratio between the intensities of the 0-0 and 0-1 NIR absorption peaks is slightly higher in solution than in thin-film.

TGBC devices with ca. 400nm PMMA dielectric were fabricated and tested under a nitrogen atmosphere. Transfer/output characteristics and mobilities are shown in Figure 4-19. The representative AN device shows similar ambipolar behavior compared with NN polymer devices due to low bandgap. However, significantly improved performance is observed for the AN device, with saturation mobility above 0.5 $cm^2V^{-1}s^{-1}$ and linear mobility above 0.3 $cm^2V^{-1}s^{-1}$.

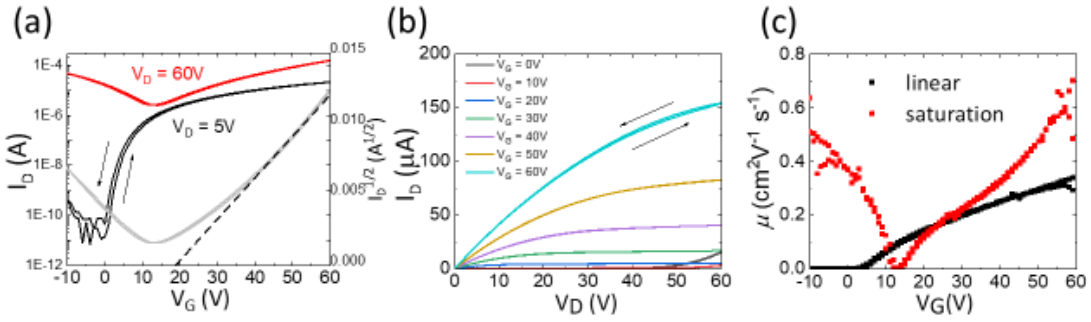

Figure 4-19 Transfer curves (a) output curves (b) and mobilities (c) of a representative AN TGBC OFET (L = 20 μm, W = 1mm).

To figure out the microstructural origin of this high performance, GIWAXS is performed on AN films prepared with the same condition of OFETs (Figure 4-20).

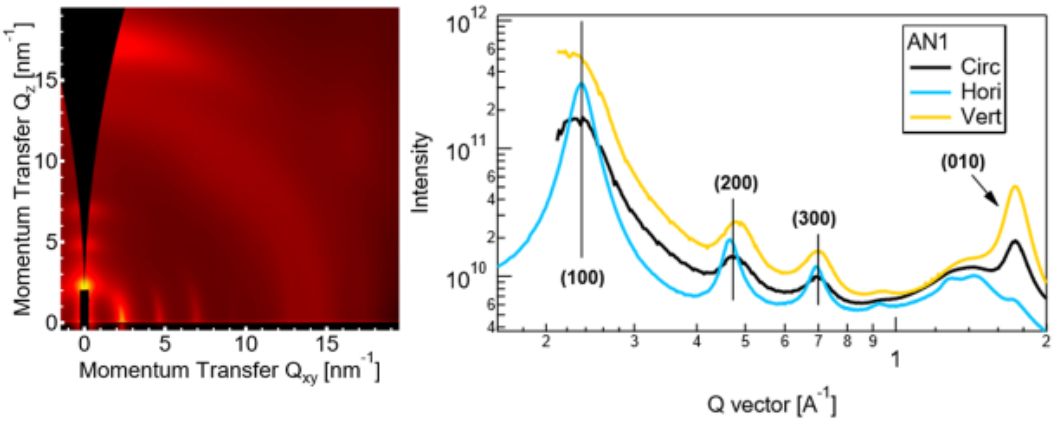

Figure 4-20 2D Giwaxs pattern of AN polymer (left). GIWAXS line-cut profiles of AN polymer (right). GIWAXS experiments performed by Professor Chris McNeill, Dr. Xuechen Jiao at the Department of Materials Science and Engineering, Monash University.

Higher-order lamellar diffraction along both in-plane and out-of-plane directions are observed. However, distinct to the observation of NN2 and NN3 is that the diffraction along the in-plane direction around the π-π stacking range exhibit three peaks, which might be signal from rigid backbone repeating units and are worth further investigation. Due to the beam-stop effect, the lamellar (100) peak along the out-of-plane direction cannot be well resolved, hence we will analyse the (200) peak instead. For the AN polymer, along the out-of-plane direction, the lamellar stacking distance is 26.04 Å, while along the in-plane direction, the lamellar stacking distance is 26.74 Å. The π-π stacking distance of AN polymer is 3.64 Å, for both in-plane and out-of-plane direction.

The PDS spectrum is measured for the AN polymer to investigate the energetic disorder of its joint excitonic DOS, Urbach energy for AN is extracted from the PDS measurements. The results are shown in Figure 4-21. Compared with NN fused polymer, AN polymer shows significantly lower energetic disorder with an Urbach energy around 33meV, similar to the very low energetic disorder material P(NDI2OD-T2),

which has a similar level of Urbach energy which is 32 meV [163],. This very low energetic disorder could be one of the reasons contributing to its high field-effect mobility within OFETs.

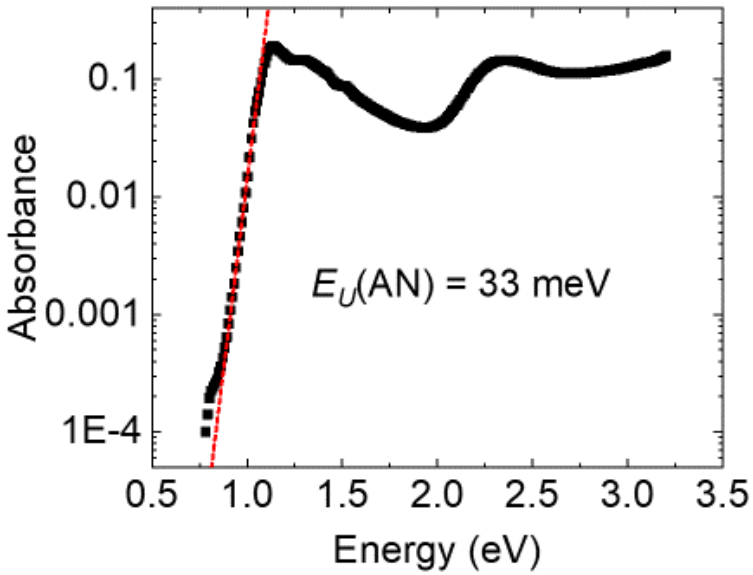

Figure 4-21 PDS spectrum of AN polymer and Urbach energy extraction from PDS spectrum. The PDS measurement was performed by Dr. Aditya Sadhanala, Dr. Mojtaba Abdi Jalebi at the Cavendish Laboratory, University of Cambridge.

4.6.2 Characterization of AA polymer

High molecular weight (Mn/Mw 359/1184 kDa) AA polymer was synthesized by our collaborator Dr. Hu Chen in KAUST. TGBC device with ca. 400nm PMMA is fabricated and tested under a nitrogen atmosphere. Transfer/output characteristics and mobilities are shown in Figure 4-22. AA devices show similar ambipolar behavior compared with NN and AN polymer due to low bandgap. Interestingly, the device performance of the AA OFET is worse than NN and AN polymer with the same side-chain strategy with saturation mobility less than 0.1 cm^2/Vs and linear mobility around 0.05 cm^2/Vs.

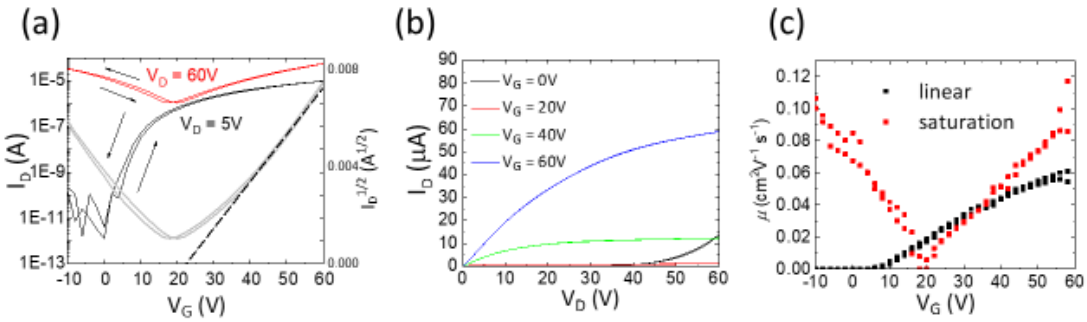

Figure 4-22 Transfer curves (a) output curves (b) and mobilities (c) of a representative AA polymer TGBC OFET (L = 20 μm, W = 1mm).

GIWAXS measurements were performed on AA films to characterize their microstructural properties with results shown in Figure 4-23. AA film consists of two types of crystallites with distinct preferential orientation-face-on and edge-on. Both face-on and edge-on crystallites exhibit strong lamellar crystallinity as seen by the third-order lamellar diffraction (300). Different to NN and AN, the π-π stacking (010) adopt the same d-spacing (d=3.57 Å, q=1.76 $Å^{-1}$) along face-on and edge-on direction. This π-π stacking distance is closer than the π-π stacking observed in NN and AN polymer, which should be ideal for the interchain charge transport process. However, why this ideal micro-structure feature does not turn into improved charge transport property is an interesting topic worth investigation in the future. For example, more sophisticated microstructure investigations, including the 2D NMR technique[192], would be useful to figure out the exact inter-chain packing strategy and the impacts on intermolecular transfer integral.

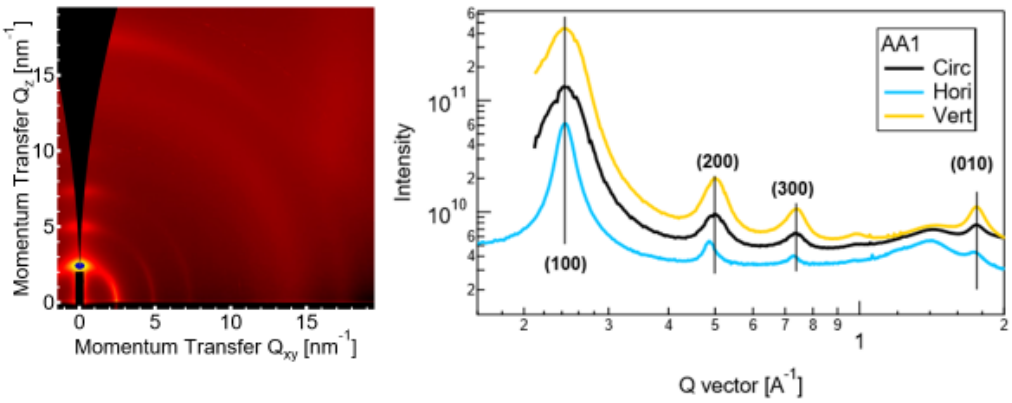

Figure 4-23 2D Giwaxs pattern of AA polymer (left). GIWAXS line-cut profiles of AA polymer (right). GIWAXS experiments did by Professor Chris McNeill, Dr. Xuechen Jiao at the Department of Materials Science and Engineering, Monash University.

Figure 4-24 presented the results of PDS measurements for AA polymer with Urbach energy calculated to be 28.2meV, which is among the lowest reported for conjugated polymers[29].

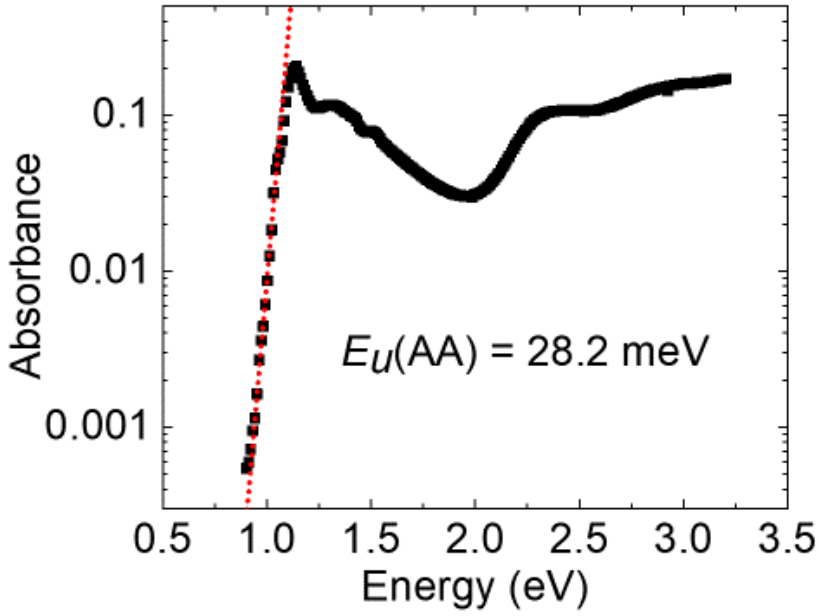

Figure 4-24 PDS spectrum of AA polymer and Urbach energy extraction from PDS spectrum. PDS measurements done by Dr. Aditya Sadhanala, Dr. Mojtaba Abdi Jalebi at the Cavendish Laboratory, University of Cambridge.

4.7 Chapter Summary

In this chapter, we show that it is possible to realize the rigid rod behaviour of conjugated polymers synthesized by aldol condensation with only double-bond and no single-bond linkages between fused-ring conjugated units. We have shown evidence that the persistence lengths of these polymer matches/exceeds their contour lengths. We have also demonstrated that by the side-chain optimisation and by adopting a copolymer design, it is possible to achieve respectably low energetic disorder and high electron mobilities of 0.5 $cm^2V^{-1}s^{-1}$ that are within an order of magnitude to those of the best-performing conjugated polymers. The level of performance achieved to date is already of interest for large-area electronics because of the excellent stability for n-type OFET operation in air.

5. Anisotropy of charge transport in a uniaxially aligned fused electron deficient polymer

Precise control of the microstructure in organic semiconductors (OSC) is essential for developing high-performance organic electronics and optoelectronics devices. Here we report a comprehensive microstructural and charge transport characterization of two recently synthesized, structurally similar fused poly-iso-indigo naphthalene based electron-deficient polymers (NN1 and NN2). We demonstrate that this structure makes it possible to overcome the bends and kinks typically observed in traditional conjugated polymer systems and obtain an exceptionally high persistence length (l_p) of 40 nm which could be directly visualized with a high-resolution scanning tunneling microscopy (STM) technique. These very rigid, and fully conjugated polymers show similarity to carbon nanotubes (CNTs), demonstrating morphologies significantly different from traditional conjugated polymers. We further use a simple one-step non-contacting solution shearing technique with a commercial PTFE rod blade to align the polymer chains and observe high optical anisotropy of up to a factor of 6. Transport measurements performed on these aligned films using top-gate bottom-contact (TGBC) field-effect transistors exhibit a saturation electron mobility of 0.2 cm^2/Vs along the aligned direction, which is more than six times higher than the value reported in our previous work. This not only demonstrates this specific polymer's potential as a semiconducting material in next-generation n-channel organic field-effect transistors (OFETs) but also provides an optimized processing strategy for this class of newly emerging rigid-rod polymer system in general.

5.1 Introduction of meniscus-guided solution-shearing technique

Choosing the right processing condition is essential to realize ideal charge transport properties. Fast-drying processes like the commonly used spin-coating technique do not always lead to optimal microstructural order for semi-crystalline polymers, which restricts the optimisation of these polymer semiconductors. Thus, for certain families of semi-crystalline materials, a more controlled film deposition technique must be developed to improve their structural order and charge transport properties further. Techniques reported in the literature include several meniscus-guided coating techniques like zone casting[193], solution shearing[80][194], slot-die coating[195] and dip coating[196]. These not only allow improved charge transport to a level that it can outperform some of the inorganic semiconductors, such as amorphous silicon[15][197], but also have the potential of large-area scalability and compatibility as well as the convenience of a single-step fabrication process[56]. The relative uni-directional motion of the solution meniscus to the substrate produces a shear force on the fluid that promotes polymer chain alignment during the film drying process. Film deposition happens during the well-controlled solvent drying process across the substrates to deliver aligned polymer films. Intuitively, it can be expected that this technique would be particularly favorable if the polymer adopts a fully fused, rigid backbone structure allowing the realization of microstructures comparable to aligned CNT networks[180][198]. Based on the experience of CNTs, the disorder in the raw material could be significantly reduced after alignment and anisotropy in electronic transport properties could be observed as well, with improved transport along the tube alignment direction[199]. Similarly, for our fused polymer system, its unique backbone structure not only shows the potential to outperform other classes of conjugated polymers due to reduced disorder[180] but also should be the ideal backbone structure for alignment, making the process easy and achieving a high degree of charge transport anisotropy. In short, the meniscus-guided coating technique offers a new approach to advance both our understanding

of the charge transport physics in these fused n-channel polymer semiconductors as well as their device applications.

5.2 High resolution STM image of NN1 polymer

The polymers used in this study are shown in Figure 5-1 (a) and (b). The two polymers referred to as NN1 and NN2 have the same fused backbone structure but vary in the alkyl side chain attached. In order to visualize their backbone structure directly, we performed high-resolution scanning tunneling microscopy (STM) imaging of the films fabricated on gold (111) surface[171]. Unfortunately, the solubility of the NN2 polymer is too low to deposit it on the gold surface successfully. However, owing to the improved solubility of NN1 imparted by the longer alkyl chain we successfully deposited NN1 on a gold (111) surface and used STM to image the backbone structure with molecular resolution (Figure 5-1 (c) and (d)). Polymer chains in these images are mostly straight with occasionally observed kinks and tend to lie parallel to each other. More importantly, structural chain defects, such as abrupt kinks, appear mostly absent in the STM images of NN1. This straight chain conformation is believed to reflect the rigid rod nature of the polymer due to the absence of single bonds along the backbone. It is also apparent that the side chains are able to assemble into an ordered structure and do not disturb the linear conformation of the backbone.

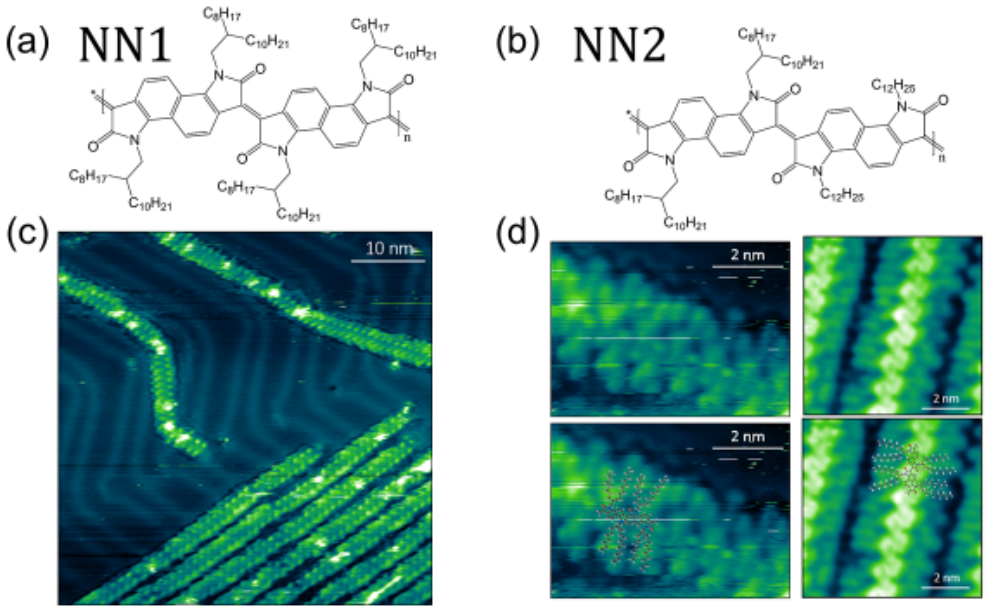

Figure 5-1 Chemical structure of (a) NN1 (b) NN2 polymer. (c) STM image showing NN1 polymer adsorbed on Au(111). (d) sub-molecular resolution STM images of NN1 polymer. The central bright region corresponds to the conjugated core, and the alkyl chains correspond to the lighter areas. STM experiments are done by Professor Giovanni Costantini, Dr. Luís M. A. Perdigão, Dr. Alex Luci of Department of Chemistry, University of Warwick.

The persistence length l_p is a direct measurement of the stiffness of polymer chains, and may be defined as the length scale for chain bending by 90 degrees on average.[174] Recently, it is noted that large l_p of conjugated polymers might be beneficial for their applications in optoelectronic devices, and several high performance conjugated polymers used in OFETs and photovoltaics demonstrate significantly higher persistence lengths compared with P3HT[175]. Stiffer chains are likely to increase intrachain electronic coupling, facilitate on-chain charge delocalization, and provide short and straight paths for charge transport within polymer film[176]. Backbone deflection angles and torsional potentials together decide a polymer's persistence length[174]. For both NN1 and NN2, well-designed backbones guarantee the linearity while large torsional potentials between adjacent aromatic units[75] further rigidify the backbone structure. Thus, NN1 and NN2 may be expected to exhibit large l_p. With the STM technique, l_p of NN1 was calculated to be 40 nm from the regions scanned directly (Figure 5-2(a)), with straight segment lengths distribution analysis presented as well (Figure 5-2(b)). To the best of our

knowledge, this l_p is exceptionally high compared to the values of all the conjugated polymers measured up to now and even higher than the values of some state-of-the-art conjugated polymers estimated from the freely rotating chain model[175](a simplified version of the hindered rotation model[200]), which provide trustworthy insights into chain stiffness in a range of conjugated polymers[175]. For example, three high mobility polymers, ranging across different degrees of crystallinity, all show estimated l_p lower than NN1 observed from STM imaging[175]: the persistence lengths of DPP-DTT[201], PffBT4T-2OD[202] and C_{16}IDT-BT[19] are estimated to be 7.9nm, 13.3nm, and 29.2nm respectively by freely rotating chain model[175]. As another reference, for the DPP-DTT polymer a calculation of persistence was also reported[37] based on the formula given by Flory *et al*. [203], which obtained a value of 42.5nm under the assumption that no torsions, only cis-trans isomerism. Of course, it is not possible to directly compare values from such calculated lengths with the ones determined here experimentally on a surface. However, these comparison provide some reference for the exceptionally long persistence length of NN1. To the best of our knowledge, the l_p of NN1 estimated from the STM image is one of the highest values reported up to now for conjugated polymers (comparable to the value of BCHA-PPV measured from light scattering technique[177]), and outperforms those of a range of commonly used high-mobility conjugated polymers, including P3HT and PBTTT, determined by various techniques, such as light scattering, small-angle neutron scattering (SANS), viscosity measurements and molecular dynamics (MD) simulations[175]. As discussed previously, this observation can possibly be attributed to the larger energetic barrier for torsional 180° rotation around double bonds(≈25 kcal mol^{-1}) compared with single bonds(≈2–8 kcal mol^{-1}).[75]. These results motivate the usage of alignment techniques to fully exploit the rigid polymer backbone structure and to enhance charge transport along the polymer chain direction.

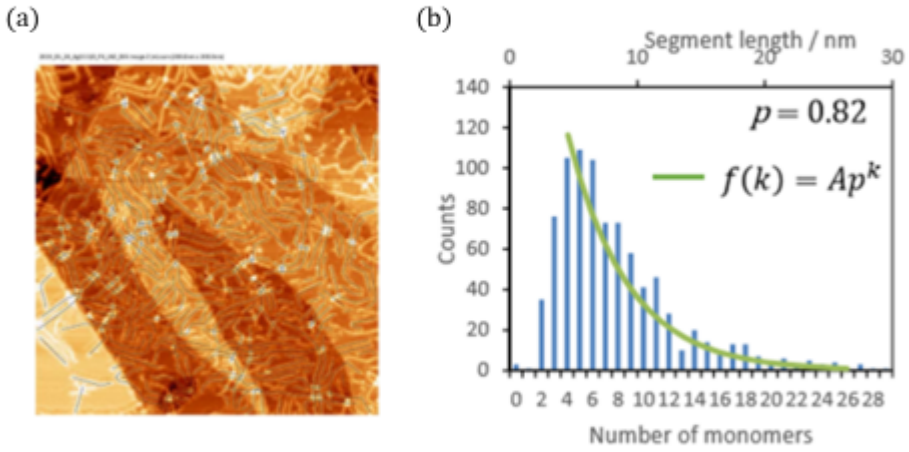

Figure 5-2 (a) persistence length analysis for NN1 from STM image, (b) straight segment lengths distribution analysis based on the same image. STM experiments and data analysis done by Professor Giovanni Costantini, Dr. Luís M. A. Perdigão, Dr. Alex Luci of Department of Chemistry, University of Warwick.

5.3 Anisotropy of aligned NN2 films

In order to align the polymer films, we use a solution shearing technique with a PTFE rod working as the coating blade. After a range of optimization procedures, we adopted a procedure where a temperature-controlled glass substrate (140 °C) was moved at a fixed speed of 146 μm/s underneath a PTFE coating blade. By using this technique, it was possible to restrict the solvent evaporation to the edge of the meniscus and align the polymer chains uniaxially along the shearing direction in NN2. It is worth noting that only 10 μL of the solution is required to fully cover a 16mm × 16mm substrate by solution shearing compared to 100 μL solution required to obtain uniform film coverage in the spin coating process indicating the efficacy of the solution shearing technique for large-area electronics applications. Detailed microstructure characterization was performed on the aligned and spin-coated films of both NN1 and NN2 polymer. AFM measurements performed on spin-coated NN2 films indicated a disordered surface morphology with small grains of a few nm's in size (Figure 5-3(a)). Upon solution shearing of the NN1 polymer, it was possible to observe an anisotropic microstructure with well defined, aligned fibrils each with a width on the order of 100 nm (Figure 5-3(b), Figure 5-4). In addition, the root mean square roughness of the film increases to 16.8 nm compared with 5.3

nm for spin-coated films. However, under similar conditions, the AFM image of NN1 did not exhibit any significant variation upon solution shearing. NN1 OFETs made with solution shearing technique shows no anisotropy in terms of charge transport and demonstrate mobility in both directions similar to spin-coated device reported previously[75], as shown in Figure 5-5 .This behavior can possibly be attributed to the un-favorable side-chain structure, which results in the relatively weaker interchain interaction and lower achievable degree of crystallinity in the material[75]. One of the possible ways to quantify the degree of alignment of the film is to characterize the dichroic ratio from optical absorption measurements parallel and perpendicular to the alignment direction. It was possible to observe a dichroic ratio close to 6 from the absorption peak around 2.3 eV for aligned NN2 film. It is important to note that the optical transition dipole moment of NN2 is likely to have a non-zero component perpendicular to the polymer backbone direction, which implies that the dichroic ratio should only provide a lower bound for the degree of alignment.

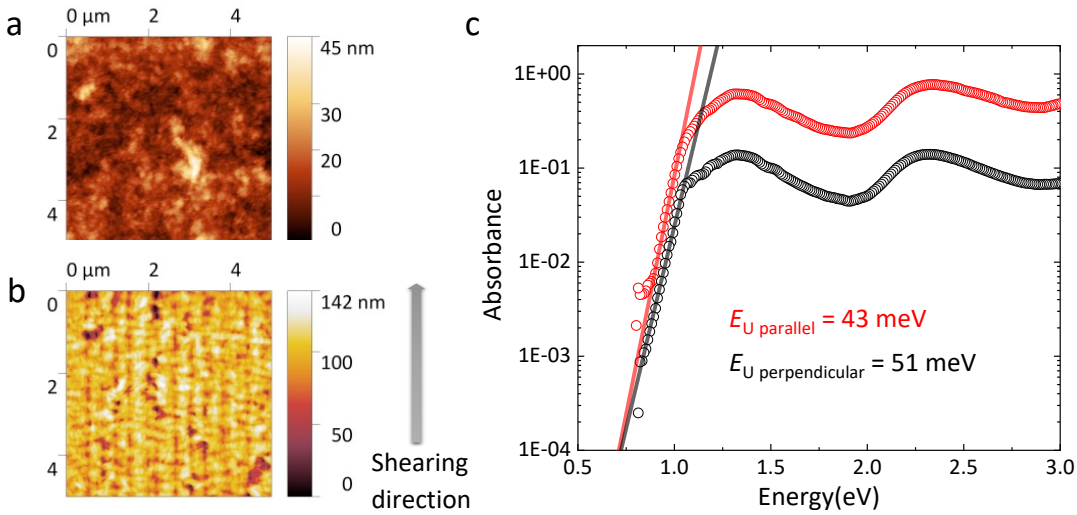

Figure 5-3 (a) AFM image of spin-coated NN2 polymer (b) AFM image of aligned NN2 polymer (with arrow below showing the shearing direction) (c) Polarized PDS spectrum of the aligned NN2 film along directions parallel and perpendicular to chain alignment directions.

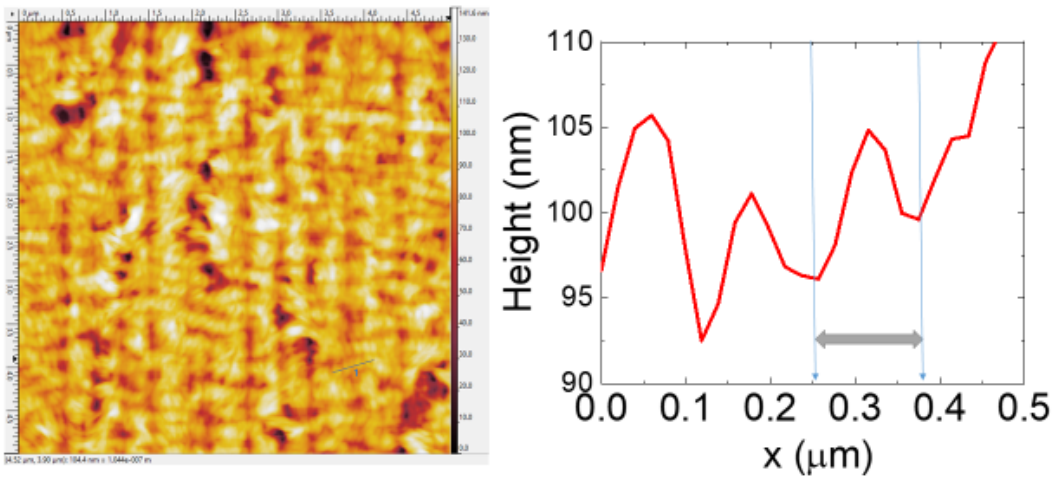

Figure 5-4 (left) AFM image of aligned NN2 film with the line-cut region labelled (right) direct estimation of width of fibrils from the line-cut of AFM image.

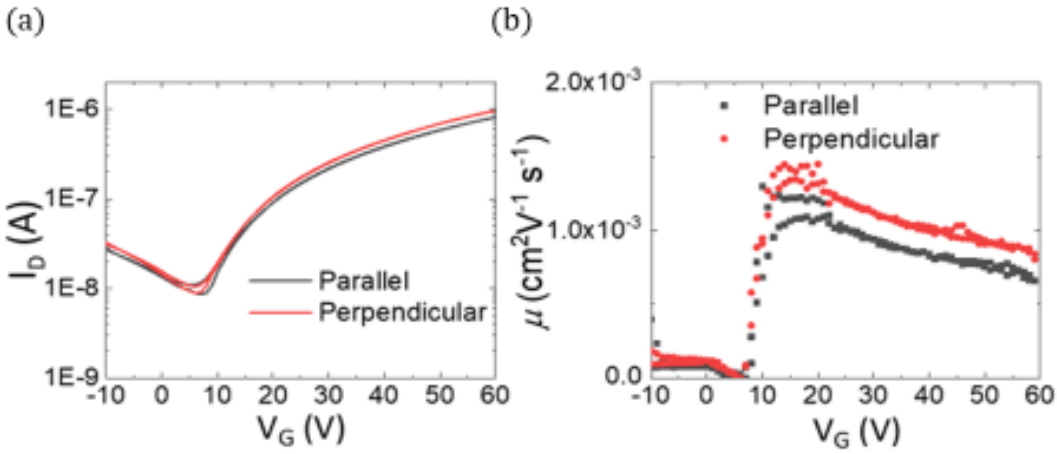

Figure 5-5 (a) Transfer curves measured on solution-sheared NN1 OFET with charge transport direction parallel and perpendicular to the solution shearing direction (b) saturation mobilities comparison between directions parallel and perpendicular to the solution shearing direction.

The band-tail region of the absorption spectrum reveals important information, such as the amount of energetic disorder. The disorder which creates trap states in the bandgap would broaden the absorption onset and create an exponential sub-bandgap tail (Urbach tail)[161], the characteristic width of which is defined as the Urbach energy (E_u) and can be interpreted as a measure of the width of the DOS[163]. We performed PDS measurements on the aligned NN1 sample to obtain the Urbach energies along directions parallel and perpendicular to chain alignment directions.

The working mechanism of PDS is described in the experimental section. For the aligned film, it is possible to extract the E_u to be 43 meV for measurement parallel to the aligned direction. In comparison, the E_u was observed to be 51 meV for measurement perpendicular to the alignment direction (Figure 5-3(c)). These measurements indicate a decrease in energetic disorder along the alignment direction. This presumably indicates that the chains or chain segments that are aligned along the shearing direction with the aligned fibrils exhibiting lower conformational and energetic disorder than those chain segments or chains that are in regions of the film that are poorly aligned, such as grain boundaries or more disordered regions in between the aligned fibrils.

5.4 GIWAXS analysis on aligned NN2 films

To further characterize the alignment procedure we performed detailed structural analysis of the polymers through the GIWAXS measurements and summarized the GIWAXS spacing parameters for both spin-coated and sheared samples in Table 5-1. The π–π stacking distance and lamella stacking distance are calculated from the related peak spacing Q_{hkl} through the equation $d_{hkl}= 2\pi/Q_{hkl}$, with Q_{hkl} in nm^{-1} , while the associated coherence lengths were estimated from the radial full width at half maximum(FWHM) via Scherrer's equation[51][204], with Q_{FWHM} in nm^{-1}. For the spin-coated sample, it shows bimodal morphology with both face-on and edge-on oriented crystallites: For the face-on crystallites a π–π stacking peak is observed in the out of plane direction with close π–π stacking distance of 0.38 nm, which is similar to other high mobility D-A copolymers[8]. For the edge-on crystallites two orders of alkyl-stacking (h00) peaks are observed along the out-of-plane direction as well. In contrast, aligned samples show preferential edge-on orientation, with significant anisotropy between the incident X-ray beam being along the direction parallel and perpendicular to the chain alignment direction. Along the chain alignment direction, the (h00) peaks as well as the weak π–π stacking diffraction exhibit an arc texture indicating a distribution of grain orientations around the surface normal, while perpendicular to chain alignment

direction, the arc disappears. In consideration of the alignment process during which lamella crystals grow, the arc could be correlated with the perturbation of the lamella crystals during this process, which is frozen after film drying, so this arc signal, which is a clear manifestation of crystalline disorder, would be more evident when the sample is measured along the alignment direction. For both directions, alkyl stacking (h00) peaks up to three orders could be observed, implying increased crystallinity compared with spin-coated samples, which agrees with the observation from the AFM images. The lamella stacking distance in the out-of-plane direction is reduced significantly compared with spin-coated film, showing out the shearing process impacts the angle at which the side chains are oriented with respect to the substrate normal. The π–π stacking distance stays almost the same upon alignment, indicating there is no significant lattice strain or other non-equilibrium effects that were observed for sheared TIPS-pentacene[80]. In conclusion, the analysis of GIWAXS patterns further confirms the structural order improvement and strong structural anisotropy induced by this solution shearing process.

Table 5-1 GIWAXS spacing parameters for spin-coated and solution-sheared samples

Crystallographic parameters		Parallel	Perpendicular	Spin-Coating
Lamella stacking (Out-of-plane)	q (Å^{-1})	0.247	0.247	0.464
	d-spacing (Å)	25.4	25.4	27.1
	FWHM (Å^{-1})	0.0505	0.0392	0.0842
	Coherence length (Å)	224.2	288.7	134.4
Lamella stacking (In-plane)	q (Å^{-1})	0.236	0.236	0.242
	d-spacing (Å)	26.6	26.6	26.0
	FWHM (Å^{-1})	0.0403	0.0565	0.0346
	Coherence length (Å)	281.1	200.1	326.9
π - π stacking (Out-of-plane)	q (Å^{-1})	1.703	1.697	1.654
	d-spacing (Å)	3.7	3.7	3.8
	FWHM (Å^{-1})	0.455	0.155	0.173
	Coherence length (Å)	25.2	74.2	66.2
π - π stacking (In-plane)	q (Å^{-1})	1.63		
	d-spacing (Å)	3.9		
	FWHM (Å^{-1})	0.170		
	Coherence length (Å)	67.5		

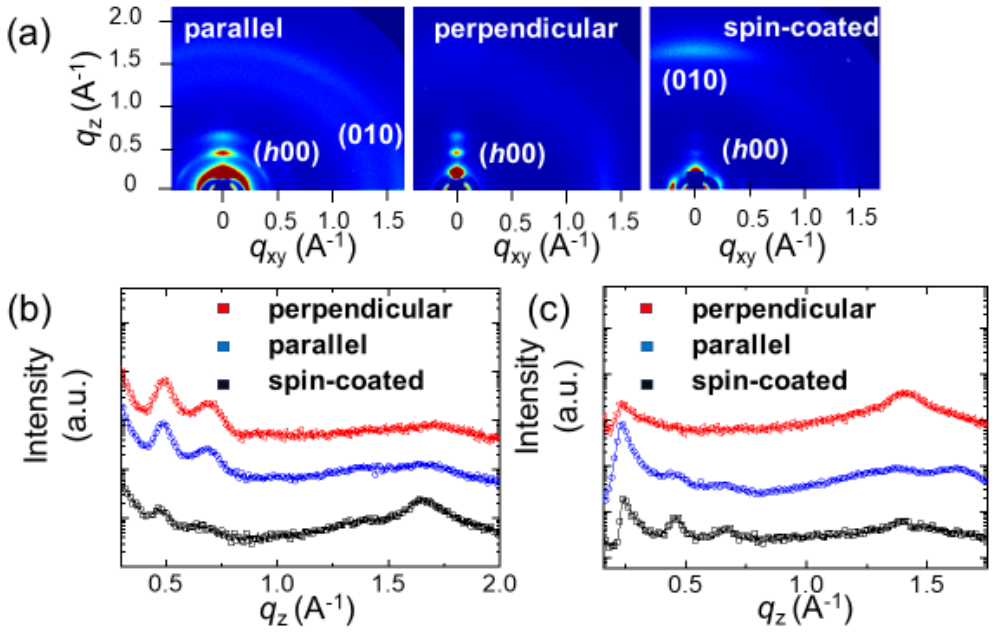

Figure 5-6 (a) Grazing incidence wide-angle X-ray scattering patterns of spin-coated and sheared NN1 film (parallel and perpendicular to the alignment direction). (b) GIWAXS line-cut profiles (out-of-plane direction). (c) GIWAXS line-cut profiles (in-plane direction).

5.5 Anisotropic charge transport within aligned NN2 OFETs

Transport measurements were performed using a top-gate, bottom-contact device architecture (TGBC) on these aligned NN2 polymer films. To obtain a clear and reliable effect of the alignment on the transistor properties, we carefully fabricated transistor channels, which are oriented at 90 degrees with respect to each other on the same substrate. Clean n-type transfer characteristics with a current modulation of $> 10^4$ and output curves with well-defined linear and saturation regimes were obtained for transistors fabricated with polymer chains aligned parallel and perpendicular to the channel direction(Figure 5-7). However, the output curves indicate the effect of contact resistance for low V_G (Figure 5-8). This barrier at the metal-semiconductor interface which is observed as a contact resistance possibly originates from the mismatch of energy levels between the gold electrode

and conjugated polymer film, or the roughness of the semiconductor thin film, thus indicating scope for further improvement in device architecture and also the shearing procedure to enhance the transport properties. The maximum channel current at $V_D = 50$ V, $V_G = 60$ V was obtained to be 80 µA for devices with polymer chain alignment parallel to the channel direction. In comparison devices with polymer chains aligned perpendicular to the channel exhibit a much lower current of 18 µA under the same conditions. Correspondingly, saturation mobility as high as 0.2 cm^2/Vs was obtained for the device with the channel along the aligned direction, which decreases to 0.03 cm^2/Vs for the device with polymer chains aligned perpendicular to the channel direction. The mobility anisotropy was thus obtained to be around 6, close to the value of the dichroic ratio obtained from UV-VIS measurements.

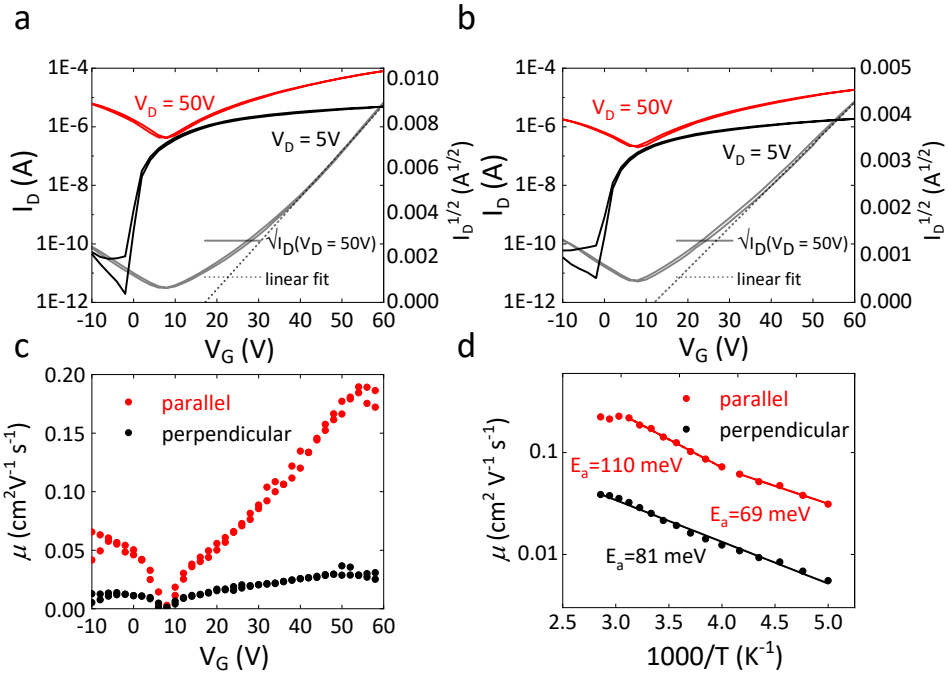

Figure 5-7 Transfer curves measured on top gate bottom contact FETs (with L = 20 µm and W = 1mm) fabricated from NN2 polymer with charge transport (a) parallel to the chain alignment direction (b) perpendicular to the chain alignment

direction. (c) Saturation mobility comparison between devices with charge transport direction parallel and perpendicular to chain alignment (d) Temperature-dependent saturation mobility for charge transport along with the two directions.

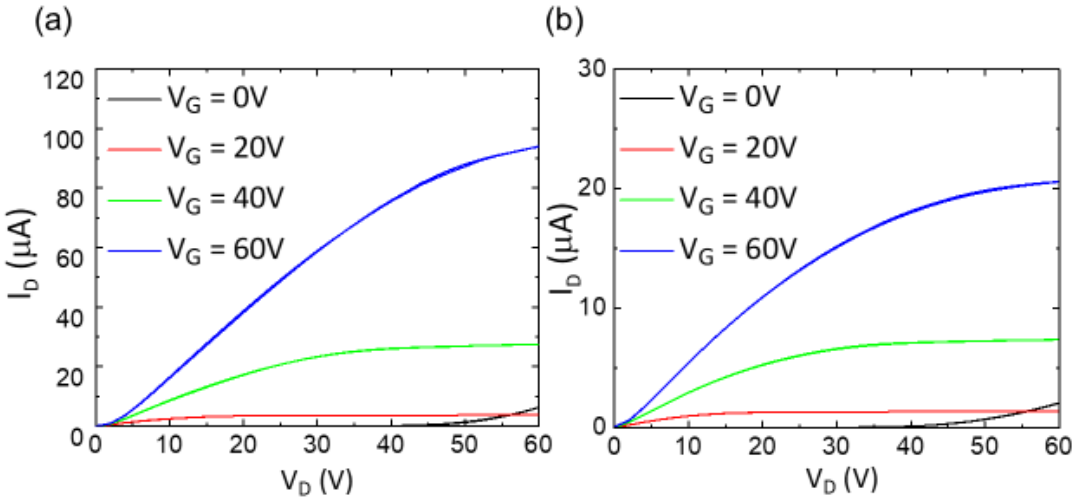

Figure 5-8 Room temperature output curves of sheared NN2 OFET for charge transport directions (a) parallel (b) perpendicular to the alignment direction.

Temperature-dependent transfer characteristics were measured over a range of 200 K to 350 K to understand the transport mechanism of OFETs with aligned NN2 film. In order to ensure a clear trend in μ_{FET}(T) and alleviate the influence of any possible artifacts like contact resistance as much as possible, we estimated the μ_{FET} in the saturation regime of operation with standard 20 μm channel length transistors. It is important to note that for the whole temperature range of the measurements, the magnitude of μ_{FET} along the chain alignment direction stays higher than μ_{FET} estimated from devices with channels perpendicular to the chain alignment direction(Figure 5-7), proving the effectiveness of our shearing technique to improve charge carrier mobility along the alignment direction. Furthermore, the temperature-dependent mobility comparison reveals different charge transport mechanisms parallel and perpendicular to the chain alignment direction. OFETs fabricated with the polymer alignment direction perpendicular to the current direction in the transistor channel, exhibit thermally activated charge transport within the whole temperature range measured. The activation energy was extracted to be 81 meV for charge transport along this direction. However, OFETs fabricated

with the current flow in the channel parallel to the polymer chain alignment exhibit three distinct regions: in the temperature range from 200-240K, charge transport is thermally activated with an activation energy of 69 meV; for the temperature region of 250-300K, the activation energy increases to 110 meV. Very similar behavior has been reported for aligned DPP-BTz OFETs along the chain alignment direction[205]. One likely explanation could be that in the shearing direction aligned fibrils have access to delocalized electronic states that are higher up in the LUMO density of states away from the band edges but allow hopping along longer distances[97]. Hence, more significant thermally activated behavior happens within this temperature range. However, when the temperature is increased above 300 K to 350 K, the transfer characteristics overlap with each other (Figure 5-9(a)), indicating that μ_{FET} is independent of temperature (Figure 5-9(b)). When ramping the temperature up and down during this regime, the transfer curves taken at the same temperature are highly reproducible, which eliminates the possibility of device degradation when operating at such temperatures. With the consideration of high activation energy in the previous temperature regime, the relatively high Urbach energy of 43meV, and mobility value below 1 $cm^2V^{-1}s^{-1}$, it is not likely a disorder free transport regime has been achieved. On the other hand, a possible explanation could be that in the high-temperature regime the mobility gets a significant contribution from a quasi 1D metallic transport due to efficient and delocalized transport along the chains and sufficient thermal energy to easily overcome the energetic barrier between aligned and less aligned domains. In terms of this, experimental techniques directly investigate charge delocalization at different temperatures and gate voltages are needed to reveal more details in the future.

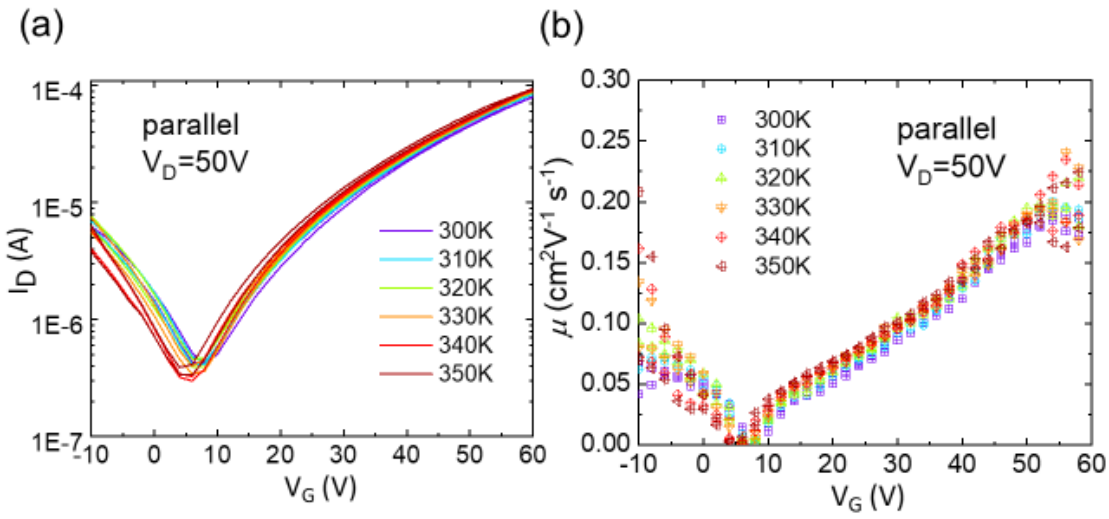

Figure 5-9 Temperature-dependent saturation transfer curves (a) and mobilities (b) for charge transport direction parallel to alignment direction for the temperature range of 300 K-350 K.

5.6 Chapter Summary

In conclusion, we have performed detailed structural and microscopic characterization on a new class of rigid, fused-ring aldol condensation polymers without single bonds along the polymer backbone. In STM it was possible to directly visualize single polymer chains with high persistence lengths and long straight chain segments. By taking advantage of this exceptional rigidity of the backbone, it was possible to uniaxially align one of the polymers by using a simple solution shear/bar coating technique and demonstrate significantly improved structural order as observed by GIWAXS. Consequently, upon alignment, the charge mobility increases by six times compared to the spin-coated films, reaching a value of 0.2 $cm^2\ V^{-1}s^{-1}$. These mobility values are within a factor of 5 compared to some state-of-the-art n-type polymers[40], which are encouraging and this class of polymers warrants further study. We see significant potential for further improvements in mobility by optimizing polymer chain structure or alignment technique[194], for example, in donor-acceptor copolymers synthesized by aldol

condensation, as these would retain the rigid rod nature with no single bonds along the backbone but are likely to exhibit smaller bandwidths and lower energetic disorder. Combining future better alignment technique and improved molecular design, even higher charge transport property with further improved anisotropy would be possible to achieve with these newly emerged, completely fused conjugated polymers, approaching the anisotropy and performance demonstrated previously by aligned P(NDI2OD-T2) system[55].

6. DMA measurements of conjugated polymers

Herein, we use dynamic mechanical analysis (DMA) to detect the β and α transitions of a range of high-mobility conjugated polymers, which have been widely investigated for applications in organic field-effect transistors (OFETs). We investigated both state-of-the-art near-amorphous and semi-crystalline donor-acceptor conjugated polymers that have shown some of the highest carrier mobilities μ_{FET} > 0.1-1 $cm^2V^{-1}s^{-1}$[206]. More traditional homopolymer systems such as polythiophene and its derivatives, have been investigated in other publications[44][70][73][207]. Despite the lack of long-range order and high crystallinity, ideal near-disorder-free transport properties exceeding the performance of amorphous silicon[14] could be achieved with OFETs made from these polymers[29]. Ideally, a near-planar, highly rigid backbone[29][37] allows charges to delocalize over long distances along the polymer backbone. Some close-contact points/aggregate regions or crystallites are needed to ensure effective interchain transport. In recent years, efforts have been made to optimise the performance of these materials[20], and understand the microscopic interactions between chains[208] but a full understanding of the role of the amorphous domains in charge transport remains elusive. A first aim of the present study is to simply report the glass transition temperatures of these polymers measured by the DMA technique, that to the best of our knowledge have not been studied yet. This is important because a knowledge of the temperatures at which mechanical relaxation processes and the glass transition occur is generally needed to inform process conditions for obtaining desired microstructures as well as for understanding the thermal stability of devices. Our second aim is to understand the relationship between glass transition and charge transport properties in these polymers.

Hopping between chains is an indispensable process to achieve macroscopic charge transport at the device level since no single chain alone could transport

charge carriers across such length scale[209]. Extended and close interchain contact is hence deemed as an essential element for high-mobility charge transport within conjugated polymers. However, up to now, very few techniques could be used to probe these short contacts directly. For example, GIWAXS experiments and related crystallinity analysis could provide basic information about averaged spacing and coherence length parameters in the crystalline domain of polymer films. However, for more subtle information such as detailed chain packing geometry and its influence on the charge-transport behaviours, the information GIWAXS could provide is limited.

6.1 DMA measurements on high mobility amorphous polymer systems

Recently, a detailed spectroscopic study and theoretical calculation of a family of near- amorphous donor-*alt*-acceptor polymers have been carried out to correlate these interchain short contact points to sub-bandgap absorption and luminescent features in polymer films[208]. According to theoretical calculation, interchain short contacts below 3.5 Å are correlated with the sub-bandgap absorption feature at around 1.3 eV for TIF-BT, as illustrated in **错误!未找到引用源。**. Besides, two luminescence pathways have been identified according to ultra-fast PL and TA measurement: namely the intra-chain ICT (internal charge transfer state) and interchain luminescence pathways, as illustrated in Figure 6-2. The nature of the redshifted interchain pathway has been figured out as “pinned ICT state” (pICT state) according to excited states calculation at close contact points[208]. The sub-bandgap absorption feature together with red-shifted luminescent pathway could hence provide a spectroscopic probe of the close contact points in the polymer film, and be used to explain the higher mobility of backbone elongated TIF-BT polymer compared with IDT-BT polymer (The reduced side-chain density and sterical hindrance are assumed to cause shorter and more extended interchain interaction in TIF-BT compared with IDT-BT according to theoretical calculation[208]).

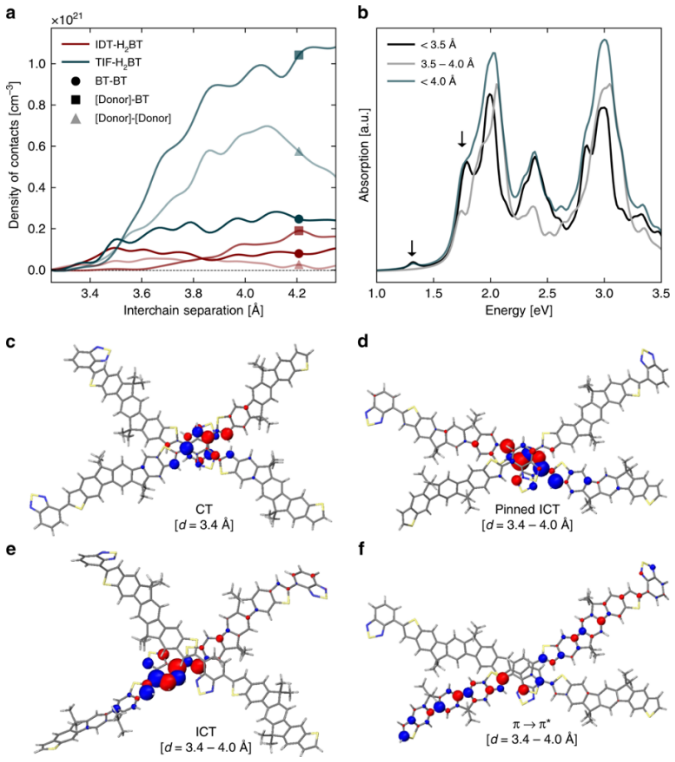

Figure 6-1 Theoretical calculations of excited states at close contact points. a Radial distribution functions for various interchain coupling motifs for IDT-H2BT and TIF-H2BT. b Absorption intensity for the closest interchain coupling motif for TIF-H2BT, shown below. For various model geometries for the close crossing of two polymer chains, transition densities for absorption features are shown: the CT formed at an interchain separation of 3.4 Å (c), and the pinned ICT (d), ICT (e), and π→π∗ (f) transitions at various geometries in the range 3.4–4.0 Å. Image and caption from [208].

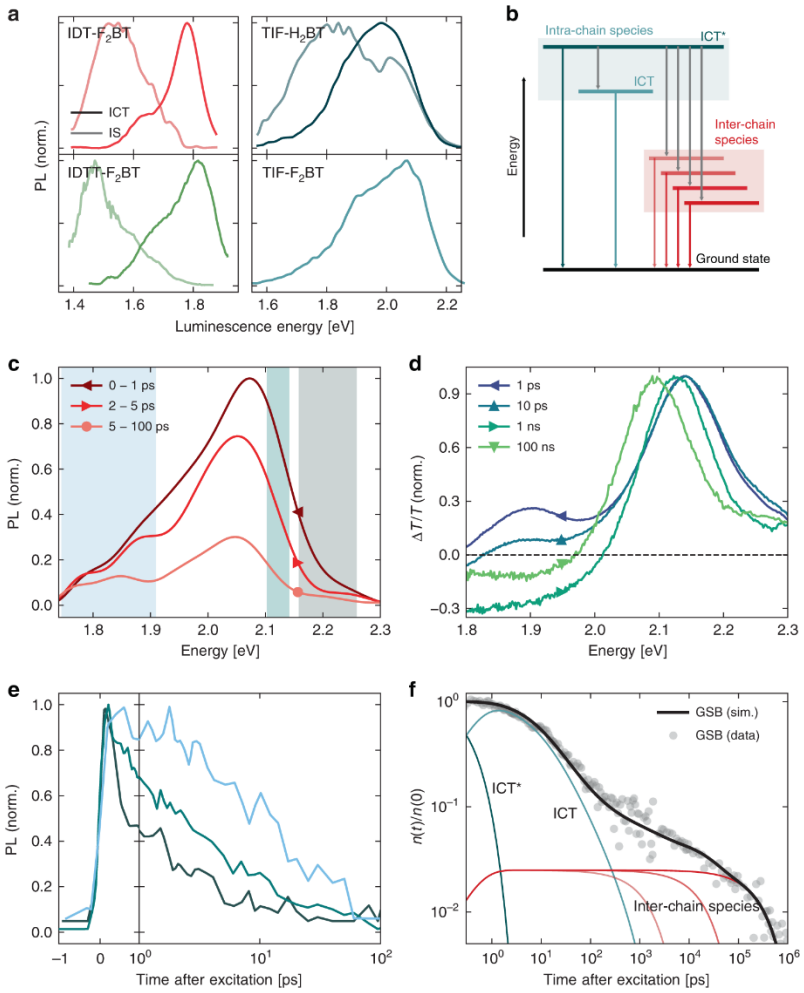

Figure 6-2 Transient optical characterisation. a PL spectra of the prompt and delayed emissive species extracted from the genetic algorithm. b Energy level diagram summarising the exciton dynamics. For TIF-H2BT: (c) ultrafast PL spectra normalised to the maximum of the first time-slice shown; (d) normalised TA spectra for different time delays; (e) kinetics of the PL decay in the different energy bands shaded in (a); and (f) GSB with population fits normalised to the maximum signal together with a fit of the contributions from different excited state species according to the kinetic model. Image and caption from[208].

However, with the consideration of the nature of these short interchain contacts, they should be the major origin of interchain “frictions”, hence it would be more straightforward if specific mechanical measurements could address these frictions directly, rather than investigate them indirectly with expensive, sophisticated and complex spectroscopic technique. In this work, material pockets are used to carry out DMA measurements on a series of IDT-BT like polymers and establish an

empirical relationship between the absorption sub-bandgap area, PLQY, and glass-transition temperatures of these polymers.

First of all, a family of IDT-BT like materials is measured, basic information including modulus and damping factor could be extracted from these measurements directly, however, all the modulus(including storage modulus and loss modulus) are mainly decided by the steel material pocket, rather than the soft polymer powders enveloped, hence only the trend of the modulus, such as abrupt turning point or bend/kink in the curves could be related with the change of polymers rather than the absolute value of modulus, which is dominated by stiffer material pockets. However, the peaks of these damping factors have accurate physical interpretation, and the position of these peaks could be related to the temperatures at which certain relaxation processes /transformation happens. From the case of IDT-BT polymer, three features could be observed directly from the temperature and frequency scans (Figure 6-3), namely the β transition related with side-chain relaxation below 0 °C, a low temperature α transition related with the backbone relaxation process (56 °C for the peak of the damping factor for the 1 Hz scan), and a high temperature melting process around 280 °C. Two frequencies are applied to the scan, namely 1 Hz and 10 Hz. Interestingly, for β and α transitions, higher frequency measurements lead to higher temperature peaks in the damping factor, while for the melting peak, such frequency-dependent relationship does not manifest, and the data points related to these two frequencies overlap. This should agree with the nature of the glass transition process as a relaxation process[210]: during the glass transition process, polymer measured need to have enough mechanical mobility such that relaxation time of chain segments matches the frequency of oscillating stress induced by the movement of the drive-shaft of the DMA. Higher-frequency measurements would hence require larger amounts of thermal energy to reach the glass transition, and the process initiate at higher temperatures. While for the melting process, since it is a truly first-order phase transition in nature, such frequency-dependence would not be demonstrated.

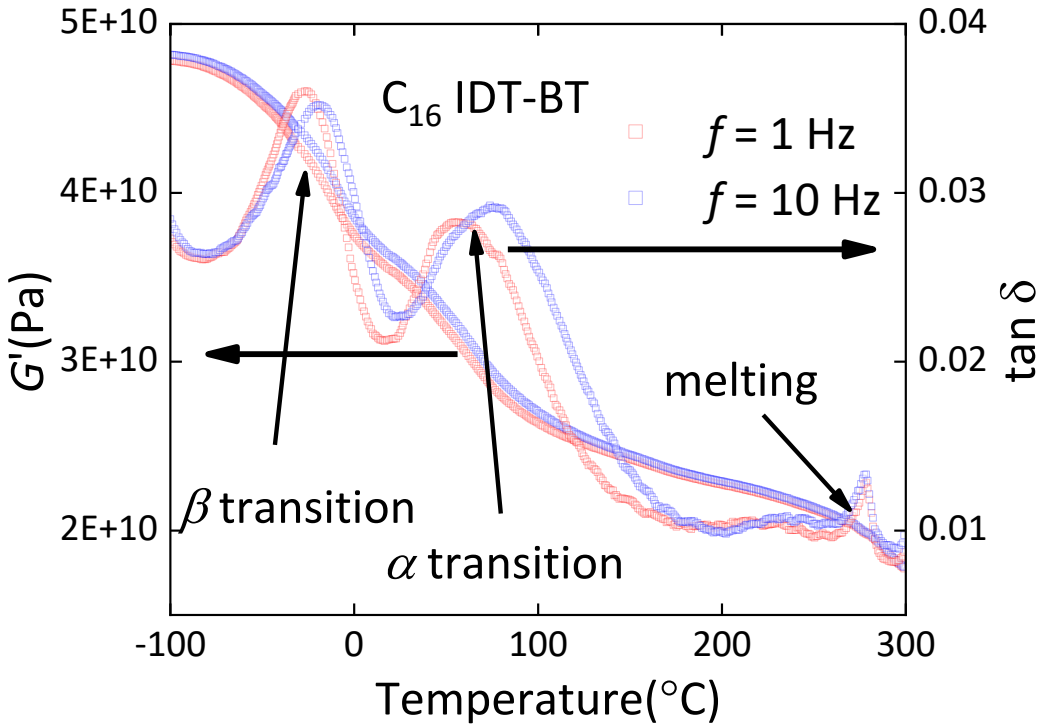

Figure 6-3 DMA measurement results of the IDT-BT C16 polymer.

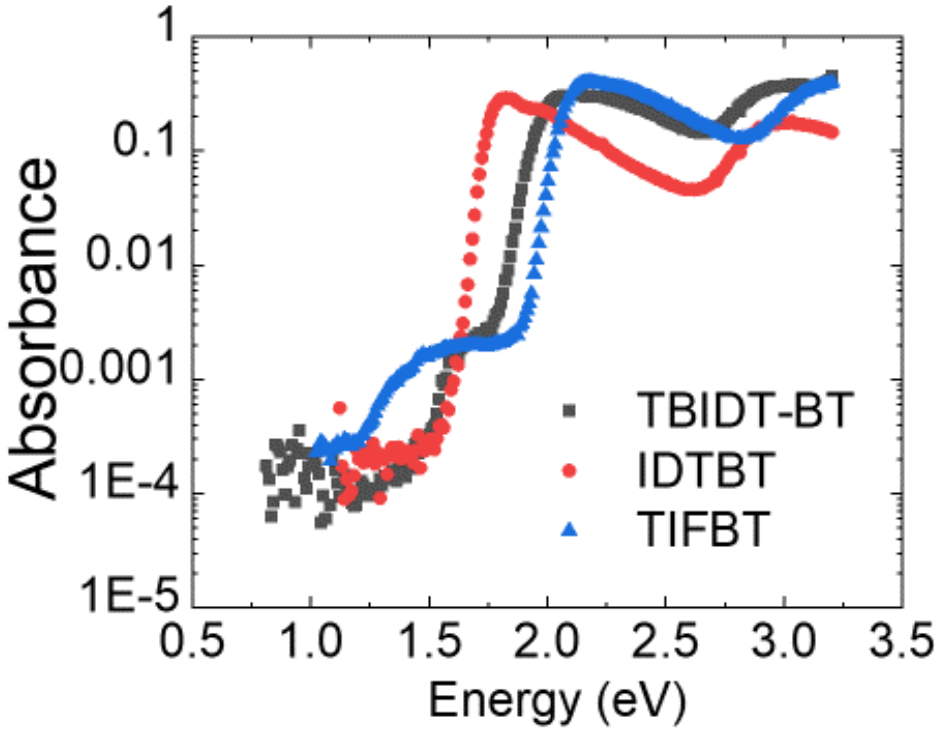

Figure 6-4 PDS measurement results of the three polymers

In this family of IDT-BT like polymers, sub-bandgap area of absorption spectrum has been correlated with the pICT states (even though only a certain portion of these sub-bandgap states are luminescent states), so an indirect way to investigate the density of these short contacts is to perform PDS measurements and directly compare the sub-bandgap area of the polymers measured. In Figure 6-4, three polymers are picked out as examples to demonstrate this. It is shown that TIF-BT, with the highest mobility and PLQY among the three (PLQY results for all the polymers measured are summarized in Table 6-1), show the most significant sub-bandgap shoulder, while for IDT-BT, no sub-bandgap shoulder has been demonstrated, in agreement with its lowest PLQY and mobility. While for TBIDT-BT, which has a moderate sub-bandgap shoulder, shows field-effect mobility value in between, as is demonstrated in Figure 6-5.

Table 6-1 Summary of the properties of the near-amorphous D-A polymers

Material	μ_{sat} ($cm^2V^{-1}s^{-1}$)	T_g (°C)	E_U (meV)	E_{opt} (eV)	PLQY

IDT-BT	1	56	23	1.66	0.017[208]
TBIDT-BT	2.5	91	39	1.82	0.057
TIF-BT	4[208]	141	31	1.94	0.15[208]

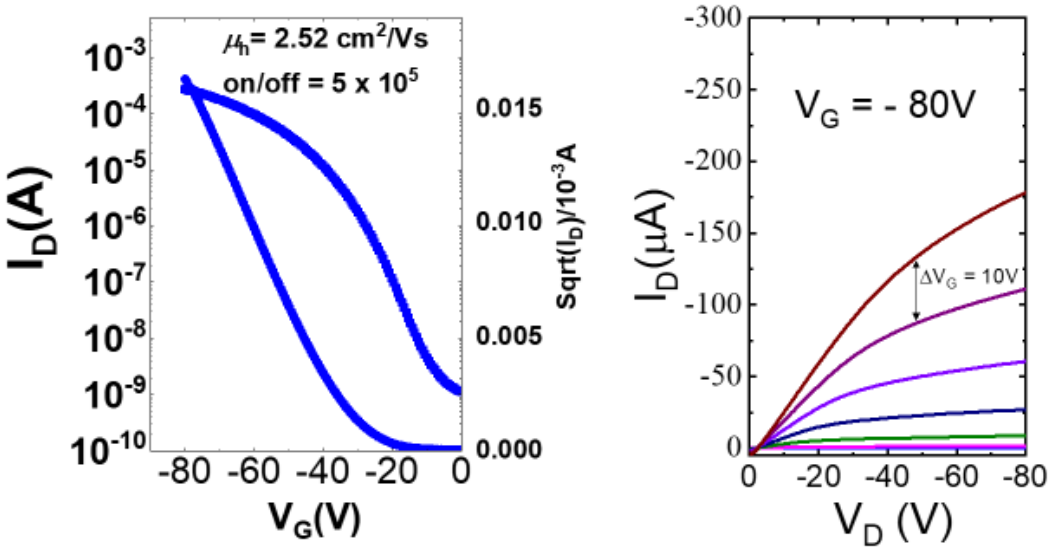

Figure 6-5 Transfer curves (left) and output curves (right) of a representative TBIDT-BT TGBC OFET (L=20 μm, W=1 mm, this device was fabricated and measured by Dr. Mark Nikolka at the Cavendish Laboratory, the University of Cambridge, data was used with permission by Dr. Mark Nikolka).

To confirm the observed spectroscopic and mobility trends are indeed related to the density of short interchain contacts, DMA is performed on the three polymers, with DMA spectra shown in Figure 6-6 and T_g values(position of the peaks of the damping factors in the 1 Hz DMA spectra) summarised in Table 6-1 . From the second peak of the damping factor, which corresponds to the backbone glass transition process, the glass transition temperature has a clear trend of IDT-BT < TBIDT-BT < TIF-BT. To a certain extent, the data could be understood in this way: for TIF-BT which has the highest density of close interchain contact points, more energy is required to break all these contacts before the polymer could be turned into more mobile rubber state. This higher energy requirement is reflected as a higher glass transition temperature directly from the DMA measurements.

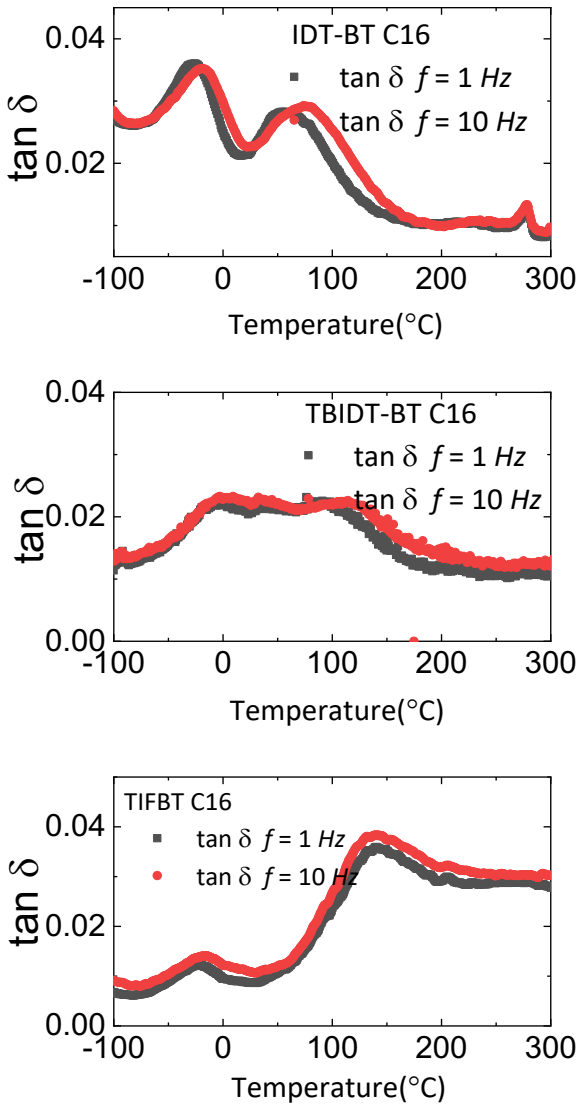

Figure 6-6 Temperature dependent damping factor for IDT-BT, TBIDT-BT, and TIF-BT

6.2 DMA measurements on high-mobility semicrystalline polymers

Three other high mobility semicrystalline DA polymers were measured, namely the DPP-BTz polymer, the DPPSe-12 polymer, and the P(NDI2OD-T2) polymer. These three polymers all show very weak or negligible (for the P(NDI2OD-T2) polymer) glass transition peaks around or above 200 °C, even higher than TIF-BT. For example, the T_g for DPPSe-12 is 190 °C, while the T_g for P(NDI2OD-T2) is 220 °C, both obtained from the weak second peak of the damping factors of the related 1 Hz DMA scans. Since the intensity of glass transition peak is related to the amounts (percentage) of amorphous content within the whole mateirals[147], and we do not have information about this for each material, the intensity of glass transition peaks could not be directly compared between each other. However, such high glass transition temperatures within these polymers do indicate the rigid and close-contact chain structures within amorphous regions of polymers, which could be the reason for high field-effect mobility within these polymer OFETs.

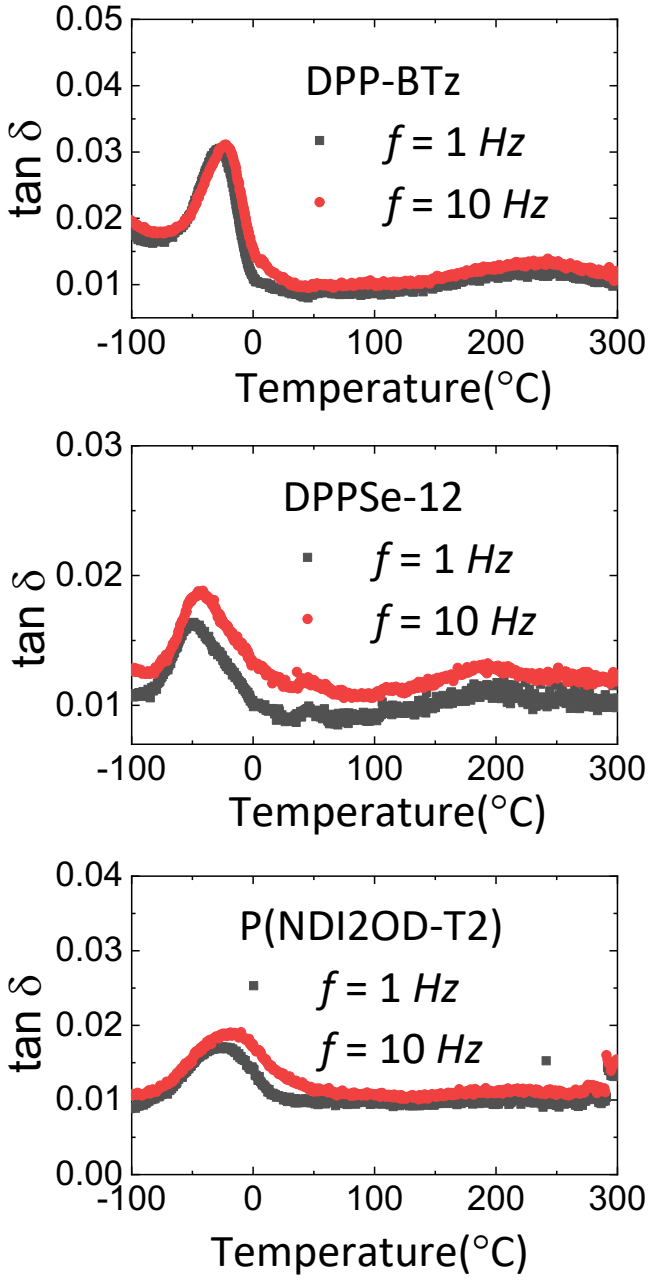

Figure 6-7 Temperature-dependent damping factors for DPP-BTz, DPPSe-12 and P(NDI2OD-T2)

6.3 DMA measurements on fused polymer systems

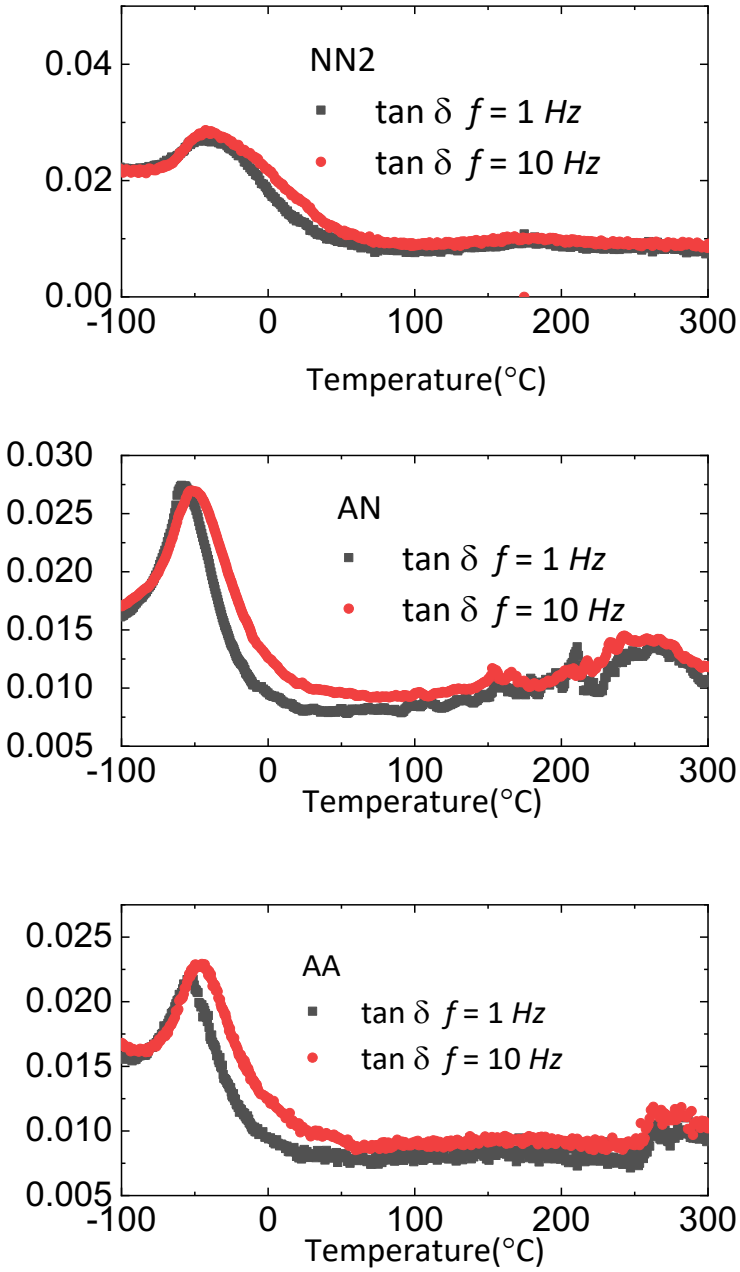

Figure 6-8 Temperature dependent damping factor for NN2, AN and AA polymers

A few fused polymers were also measured with the results presented in this work. These three polymers show high glass transition temperatures in general: the

T_g for the NN2 polymer is 180 °C, the T_g for the AN polymer is 255 °C, while the T_g for the AA polymer is 270 °C. Interestingly, with more extended backbone, AN and AA polymers do show higher glass transition temperature than NN2, which could potentially be ascribed to more rigid backbone structures achieved or more short-contact interchain contact points.

6.4 Chapter Summary

In this chapter we have measured glass tranistion temperatures for a range of state-of-the-art high-mobility conjugated polymers whose mechanical properties had hitherto not been investigated yet. For a class of near-amorphous polymers based on IDT-BT we have correlated the glass transition temperature with the nature of interchain short contacts and have observed an empirical correlation between stronger interchain short-contacts as evident in stronger sub-bandgap absorption bands and higher glass transition temperatures with weaker frequency-dependency. For a range of semi-crystalline D-A copolymers we have observed much higher glass transition temperatures than previously seen for polythiophene-based semicrystalline polymers such as P3HT and PBTTT. The high values of T_g observed in these systems are a manifestation of the reduced conformational freedom of the backbone and rigidity of the tie-chain molecules that are also responsible for the low energetic disorder/Urbach energies and excellent charge transport properties of these polymers. Our study demonstrates the importance of studying the mechanical properties and glass transition temperatures of conjugated polymers for understanding photophysical and charge transport properties. The DMA technique is an easily accessible benchtop technique with excellent sensitivity that is applicable to a wide range of amorphous and semi-crystalline conjugated polymers for different optoelectronic applications.

7. Conclusion

In this work, a detailed characterization and optimization of these newly emerged fused polymers are investigated. These high-mobility, air-stable polymers, combined with the meniscus-guided, solution shear coating technique, emerge as a new family of high-performance n-channel or ambipolar conjugated polymer system. Further improved chemical structure, including a fully planar backbone incorporating thienothiophene moiety, optimized side-chain design, could potentially increase the charge transport property of materials further. Better processing technique, such as preaggregation induced solvents combination[55] and improved shearing technique such as "fluid-flow-enhanced crystal growth through micropillar-patterned blade"[194], could be explored to induce stronger microstructural and charge transport anisotropy, hence enhance directional charge transport property of these semicrystalline materials further.

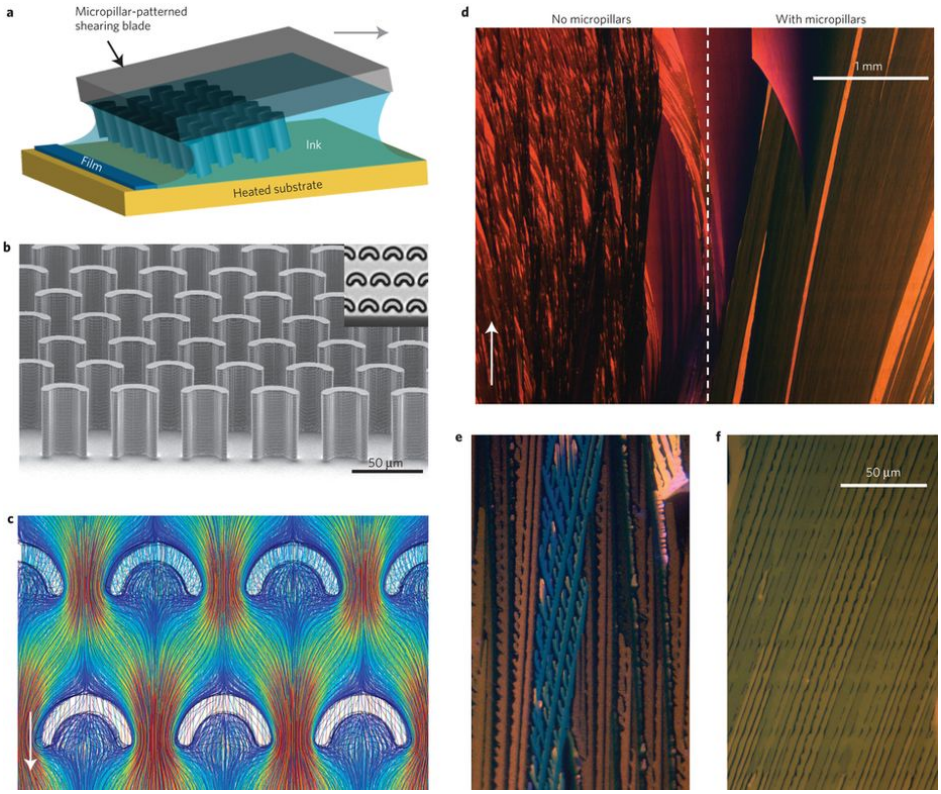

Figure 7-1 **a**, Schematic of solution shearing using a micropillar-patterned blade. For clarity, the micropillars are not drawn to scale. The arrow indicates the shearing direction. **b**, A scanning electron micrograph of a micropillar-patterned blade.

Inset, top view of the micropillars under an optical microscope. The pillars are 35 μm wide and 42 μm high. **c**, Streamline representation of simulated fluid flow around the micropillars. The arrow indicates the flow direction. The streamlines are colour coded to indicate the scale of velocity (mm s^{-1}), ranging from 0 (deep blue) to 1.3 mm s^{-1} (dark red). **d**–**f**, Cross-polarized optical micrograph of a TIPS-pentacene film coated from its mesitylene solution with (**d**, right; **f**) and without micropillars (**d**, left; **e**), at a shearing speed of 0.6 mm s^{-1}. Image and caption from [194].

Some potential experiments in the future are:

1. Continuous-wave, field-induced electron spin resonance (FI-ESR) technique could be used to study polaron spin dynamics and to obtain microscopic insight into the corresponding charge dynamics. By measuring the power saturation characteristics and linewidths of the FI-ESR spectra, it is possible to extract the spin-lattice relaxation time, T_1, and the coherence time, T_2, as a function of temperature. Motion frequencies, ν, can be computed directly from the measured ESR linewidths[98]. From the Einstein relationship $\mu = e\bar{R}^2/(k_B T)\nu$ using the measured OFET mobility μ, it is then possible to compute the average hopping distance $\bar{R}$ so long as charges are governed by motional narrowing. Interesting experiments may include comparing the NN, AN and AA polymer system, to understand the influence of backbone extension on molecular level charge dynamics, comparison between solution-sheared, aligned sample to non-aligned sample to investigate the potential difference in charge delocalisation length along with different directions of aligned sample and between aligned and spin-coated sample. Also, it would be interesting to compare the hopping distance and motion frequency between these rigid fused polymers to more traditional homopolymers or D-A polymers, to investigate the influence of morphological features such as the torsional disorder, crystallinity, and persistence lengths on the microscopic charge transport properties.

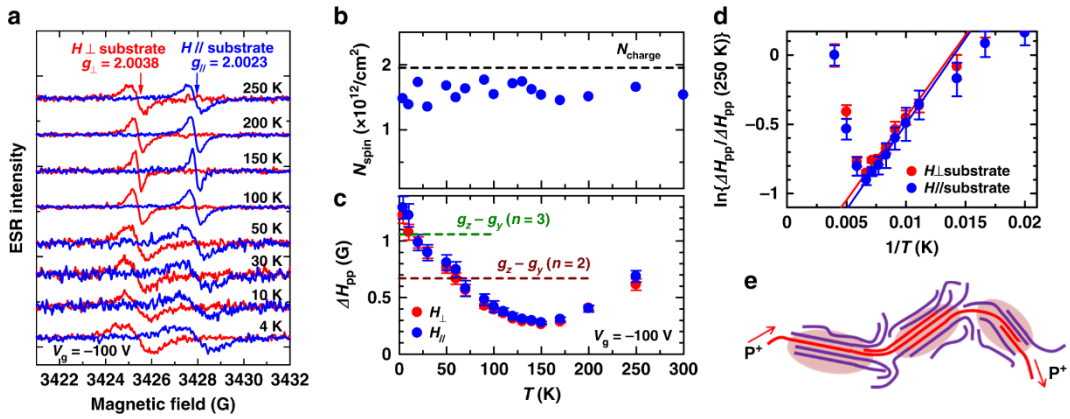

Figure 7-2 Field-induced electron spin resonance (FI-ESR) parameters for the diketopyrrolo-pyrrole-thiophene-vinylene-thiophene (DPP-TVT) device. Temperature dependence of the **a** normalized FI-ESR signal obtained with the magnetic field parallel and perpendicular to the substrate, **b** accumulated spin concentration (N_{spin}), and **c** FI-ESR linewidth (ΔH_{pp}) obtained for each magnetic field direction in the DPP-TVT device. **d** Arrhenius plot of the normalized linewidth above 50 K. **e** Schematic illustration of the microscopic charge transport of polarons (P^+) within the domains and across domain boundaries via tie molecules (shown in red) in donor–acceptor (DA) copolymers. The carriers can be fully delocalized within the domains due to strong π–π interactions both in conventional semicrystalline polymers and DA polymers. However, the interdomain transport pathways are effectively formed in the case of DA polymers, which have a rigid, highly planar backbone. The dashed line in **b** shows the charge concentration (N_{charge}) determined from the capacitance measurement. The dashed lines in **c** shows the difference in the resonance magnetic field arising from the anisotropy of the g values between the chain (g_y) and π-stack (g_z) directions calculated by the DFT method for the DPP-TVT with n = 2 and 3. The solid lines in **d** show the linear fitting of the data to the activation formulae between 70 and 150 K in both directions. Error bars represent the uncertainty in determining the linewidth due to the noise level of the FI-ESR signal. Image and caption from [38].

2. Temperature-dependent linewidth analysis of the FI-ESR spectra with magnetic fields along different directions has the potential to provide information about intra-domain and inter-domain activation energy for microscopic charge transport processes. It would be interesting to compare these "microscopic" activation energy between each other, and also to macroscopic activation energy measured from temperature-dependent FET characterisation. These might give clues about the real limiting factors of charge transport processes within materials investigated. For example, in a recent study, the intra-domain and inter-domain

activation energy of two D-A type DPP polymers are calculated from the temperature-dependent linewidth analysis of their FI-ESR spectra, the ultra-low inter-domain activation energy is assumed to originate from the rigidity of tie-chain molecules, while the significantly higher macroscopic activation energy is likely due to the rough semiconducting film surface[38] (Table 7-1). Similar linewidth analysis would be interesting for fused polymers as well since tie-chain rigidity imparted by the double-bonding fused backbone structure is likely to lead to similarly low thermal activation behaviour when charge carriers transport across domain boundaries of fused polymer films.

Table 7-1 SUMMARY OF ACTIVATION ENERGIES OF MICROSCOPIC AND MACROSCOPIC CHARGE TRANSPORT PROCESSES[38].

	E_a^{intra} (meV)	E_a^{inter} (meV)	E_a^{μ} (meV)
DPP-TVT	10 .6	10.3	74
DPPT-TT	13.6	11.9	68
PBTTT/SiO_2	21	86	90

3. It would be interesting to further optimise fused-polymer OFETs with various dielectric layers, especially with certain dielectric layers such as Cytop with lower relative permittivity (ε_r =2.1) than the PMMA dielectric (ε_r =3.6) used in this work, since dielectrics with lower relative permittivity tend to induce more moderate dipolar disorders within materials and hence provide a better OSC-dielectric interface for a more efficient charge transport process.

4. In this work, the DMA technique has shown its potential as an easily accessible, elegant, while powerful technique in terms of materials screening. Based

on the measurement results, it is at least safe to claim that certain high-performance polymers have clear correlations between charge transport/ luminescence property to their mechanical property due to the same microstructural origin, such as the interchain short contact points mentioned in this work. Further interesting experiments may include a temperature-dependent PL or fluorescence measurement on the TIF-BT system to looking for the quenching of pICT states around glass-transition temperature. High-sensitivity EQE measurements[211] of related solar cells around glass transition temperature might also be interesting if it is doable(since it is not possible to do temperature-dependent PDS measurements).

8. References

[1] J. Plans, F. J. Baltá Calleja, *Polym. Bull.* **1981**, *5*, 311.

[2] A. J. Heeger, *Rev. Mod. Phys.* **2001**, *73*, 681.

[3] H. Sirringhaus, T. Kawase, R. H. Friend, T. Shimoda, M. Inbasekaran, W. Wu, E. P. Woo, *Science (80-.).* **2000**, *290*, 2123.

[4] T. Sekitani, U. Zschieschang, H. Klauk, T. Someya, *Nat. Mater.* **2010**, *9*, 1015.

[5] J. Xu, S. Wang, G.-J. N. Wang, C. Zhu, S. Luo, L. Jin, X. Gu, S. Chen, V. R. Feig, J. W. F. To, S. Rondeau-Gagné, J. Park, B. C. Schroeder, C. Lu, J. Y. Oh, Y. Wang, Y.-H. Kim, H. Yan, R. Sinclair, D. Zhou, G. Xue, B. Murmann, C. Linder, W. Cai, J. B.-H. Tok, J. W. Chung, Z. Bao, *Science (80-.).* **2017**, *355*, 59.

[6] J. Xu, H.-C. Wu, C. Zhu, A. Ehrlich, L. Shaw, M. Nikolka, S. Wang, F. Molina-Lopez, X. Gu, S. Luo, D. Zhou, Y.-H. Kim, G.-J. N. Wang, K. Gu, V. R. Feig, S. Chen, Y. Kim, T. Katsumata, Y.-Q. Zheng, H. Yan, J. W. Chung, J. Lopez, B. Murmann, Z. Bao, *Nat. Mater.* **2019**, *18*, 594.

[7] H. Klauk, *Chem. Soc. Rev.* **2010**, *39*, 2643.

[8] H. Sirringhaus, *Adv. Mater.* **2014**, *26*, 1319.

[9] S. C. B. Mannsfeld, B. C.-K. Tee, R. M. Stoltenberg, C. V. H.-H. Chen, S. Barman, B. V. O. Muir, A. N. Sokolov, C. Reese, Z. Bao, *Nat. Mater.* **2010**, *9*, 859.

[10] J. T. Mabeck, G. G. Malliaras, *Anal. Bioanal. Chem.* **2005**, *384*, 343.

[11] L. Torsi, M. Magliulo, K. Manoli, G. Palazzo, *Chem. Soc. Rev.* **2013**, *42*, 8612.

[12] S. C. Sun, J. D. Plummer, *IEEE Trans. Electron Devices* **1980**, *27*, 1497.

[13] S. D. Brotherton, *Semicond. Sci. Technol.* **1995**, *10*, 721.

[14] C. C. Wu, S. D. Theiuss, G. Gu, M. H. Lu, J. C. Sturm, S. Wagner, S. R. Forrest, *IEEE Electron Device Lett.* **1997**, *18*, 609.

[15] R. A. Street, *Hydrogenated Amorphous Silicon*, Cambridge University Press, **2005**.

[16] R. A. Street, *Technology and Applications of Amorphous Silicon*, Springer Science & Business Media, **2013**.

[17] P. G. Le Comber, W. E. Spear, *Phys. Rev. Lett.* **1970**, *25*, 509.

[18] D. J. Yaron, T. Kowalewski, *Nat. Mater.* **2019**, *18*, 1154.

[19] S. E. Watkins, M. Heeney, A. Salleo, R. Gysel, S. Ashraf, I. McCulloch, J. Kirkpatrick, T. Anthopoulos, W. Zhang, M. McGehee, J. Smith, *J. Am. Chem. Soc.* **2010**, *132*, 11437.

[20] M. Nikolka, I. Nasrallah, B. Rose, M. K. Ravva, K. Broch, A. Sadhanala, D. Harkin, J. Charmet, M. Hurhangee, A. Brown, S. Illig, P. Too, J. Jongman, I. McCulloch, J.-L. Bredas, H. Sirringhaus, *Nat. Mater.* **2017**, *16*, 356.

[21] X. Jia, C. Fuentes-Hernandez, C.-Y. Wang, Y. Park, B. Kippelen, *Sci. Adv.* **2018**, *4*, eaao1705.

[22] A. Luzio, F. Nübling, J. Martin, D. Fazzi, P. Selter, E. Gann, C. R. McNeill, M. Brinkmann, M. R. Hansen, N. Stingelin, M. Sommer, M. Caironi, *Nat. Commun.* **2019**, *10*, 3365.

[23] A. F. Paterson, T. D. Anthopoulos, *Nat. Commun.* **2018**, *9*, 5264.

[24] H. Sirringhaus, P. J. Brown, R. H. Friend, M. M. Nielsen, K. Bechgaard, B. M. W. Langeveld-Voss, A. J. H. Spiering, R. A. J. Janssen, E. W. Meijer, P. Herwig, D. M. De Leeuw, *Nature* **1999**, *401*, 685.

[25] B. S. Ong, Y. Wu, P. Liu, S. Gardner, *Adv. Mater.* **2005**, *17*, 1141.

[26] B. S. Ong, Y. Wu, P. Liu, S. Gardner, *J. Am. Chem. Soc.* **2004**, *126*, 3378.

[27] I. McCulloch, M. Heeney, C. Bailey, K. Genevicius, I. MacDonald, M. Shkunov, D. Sparrowe, S. Tierney, R. Wagner, W. Zhang, M. L. Chabinyc, R. J. Kline, M. D. McGehee, M. F. Toney, *Nat. Mater.* **2006**, *5*, 328.

[28] R. Payerne, M. Brun, P. Rannou, R. Baptist, B. Grévin, *Synth. Met.* **2004**, *146*, 311.

[29] D. Venkateshvaran, M. Nikolka, A. Sadhanala, V. Lemaur, M. Zelazny, M. Kepa, M. Hurhangee, A. J. Kronemeijer, V. Pecunia, I. Nasrallah, I. Romanov, K. Broch, I. McCulloch, D. Emin, Y. Olivier, J. Cornil, D. Beljonne, H. Sirringhaus, *Nature* **2014**, *515*, 384.

[30] S. Wang, *Synth. Met.* **2019**, *251*, 104.

[31] S. Wang, S. Fabiano, S. Himmelberger, S. Puzinas, X. Crispin, A. Salleo, M. Berggren, *Proc. Natl. Acad. Sci.* **2015**, *112*, 10599.

[32] M. Caironi, M. Bird, D. Fazzi, Z. Chen, R. Di Pietro, C. Newman, A. Facchetti, H. Sirringhaus, *Adv. Funct. Mater.* **2011**, *21*, 3371.

[33] R. Noriega, J. Rivnay, K. Vandewal, F. P. V Koch, N. Stingelin, P. Smith, M. F. Toney, A. Salleo, *Nat. Mater.* **2013**, *12*, 1038.

[34] W. Yue, M. Nikolka, M. Xiao, A. Sadhanala, C. B. Nielsen, A. J. P. White, H.-Y. Chen, A. Onwubiko, H. Sirringhaus, I. McCulloch, *J. Mater. Chem. C* **2016**, *4*, 9704.

[35] C. B. Nielsen, M. Turbiez, I. McCulloch, *Adv. Mater.* **2013**, *25*, 1859.

[36] X. Zhang, L. J. Richter, D. M. Delongchamp, R. J. Kline, M. R. Hammond, I. McCulloch, M. Heeney, R. S. Ashraf, J. N. Smith, T. D. Anthopoulos, B. Schroeder, Y. H. Geerts, D. A. Fischer, M. F. Toney, *J. Am. Chem. Soc.* **2011**, *133*, 15073.

[37] M. S. Vezie, S. Few, I. Meager, G. Pieridou, B. Dörling, R. S. Ashraf, A. R. Goñi, H. Bronstein, I. McCulloch, S. C. Hayes, M. Campoy-Quiles, J. Nelson, *Nat. Mater.* **2016**, *15*, 746.

[38] H. Tanaka, A. Wakamatsu, M. Kondo, S. Kawamura, S. Kuroda, Y. Shimoi, W.-T. Park, Y.-Y. Noh, T. Takenobu, *Commun. Phys.* **2019**, *2*, 96.

[39] D. A. Johns, K. Martin, *Analog Integrated Circuit Design*, John Wiley & Sons, **2008**.

[40] J. T. E. Quinn, J. Zhu, X. Li, J. Wang, Y. Li, *J. Mater. Chem. C* **2017**, *5*, 8654.

[41] Y. Wang, T. Michinobu, *J. Mater. Chem. C* **2018**, *6*, 10390.

[42] H. T. Nicolai, M. Kuik, G. A. H. Wetzelaer, B. De Boer, C. Campbell, C. Risko, J. L. Brédas, P. W. M. Blom, *Nat. Mater.* **2012**, *11*, 882.

[43] Y. Yang, Z. Liu, G. Zhang, X. Zhang, D. Zhang, *Adv. Mater.* **2019**, *31*, 1903104.

[44] I. McCulloch, M. Heeney, C. Bailey, K. Genevicius, I. MacDonald, M. Shkunov, D. Sparrowe, S. Tierney, R. Wagner, W. Zhang, M. L. Chabinyc, R. J. Kline, M. D. McGehee, M. F. Toney, *Nat. Mater.* **2006**, *5*, 328.

[45] B. Kang, R. Kim, S. B. Lee, S. K. Kwon, Y. H. Kim, K. Cho, *J. Am. Chem. Soc.* **2016**, *138*, 3679.

[46] M. Nikolka, K. Broch, J. Armitage, D. Hanifi, P. J. Nowack, D. Venkateshvaran, A. Sadhanala, J. Saska, M. Mascal, S.-H. Jung, J. Lee, I. McCulloch, A. Salleo, H. Sirringhaus, *Nat. Commun.* **2019**, *10*, 2122.

[47] G. Zuo, M. Linares, T. Upreti, M. Kemerink, *Nat. Mater.* **2019**, *18*, 588.

[48] M. Nikolka, G. Schweicher, J. Armitage, I. Nasrallah, C. Jellett, Z. Guo, M. Hurhangee, A. Sadhanala, I. McCulloch, C. B. Nielsen, H. Sirringhaus, *Adv. Mater.* **2018**, *30*, 1801874.

[49] H. Yan, Z. Chen, Y. Zheng, C. Newman, J. R. Quinn, F. Dötz, M. Kastler, A. Facchetti, *Nature* **2009**, *457*, 679.

[50] R. Di Pietro, H. Sirringhaus, *Adv. Mater.* **2012**, *24*, 3367.

[51] A. Salleo, R. J. Kline, D. M. DeLongchamp, M. L. Chabinyc, *Adv. Mater.* **2010**, *22*, 3812.

[52] J. Rivnay, S. C. B. Mannsfeld, C. E. Miller, A. Salleo, M. F. Toney, *Chem. Rev.* **2012**, *112*, 5488.

[53] T. Yang, Q. Wu, F. Dai, K. Huang, H. Xu, C. Liu, C. Chen, S. Hu, X. Liang, X. Liu, Y. Noh, C. Liu, *Adv. Funct. Mater.* **2019**, 1903889.

[54] J. F. Chang, B. Sun, D. W. Breiby, M. M. Nielsen, T. I. Sölling, M. Giles, I. McCulloch, H. Sirringhaus, *Chem. Mater.* **2004**, *16*, 4772.

[55] S. G. Bucella, A. Luzio, E. Gann, L. Thomsen, C. R. McNeill, G. Pace, A. Perinot, Z. Chen, A. Facchetti, M. Caironi, *Nat. Commun.* **2015**, *6*, 8394.

[56] X. Gu, L. Shaw, K. Gu, M. F. Toney, Z. Bao, *Nat. Commun.* **2018**, *9*, 534.

[57] D. Khim, A. Luzio, G. E. Bonacchini, G. Pace, M.-J. Lee, Y.-Y. Noh, M. Caironi, *Adv. Mater.* **2018**, *30*, 1705463.

[58] S. Bauer, *Nat. Mater.* **2013**, *12*, 871.

[59] D.-H. Kim, N. Lu, R. Ma, Y.-S. Kim, R.-H. Kim, S. Wang, J. Wu, S. M. Won, H. Tao, A. Islam, K. J. Yu, T. -i. Kim, R. Chowdhury, M. Ying, L. Xu, M. Li, H.-J. Chung, H. Keum, M. McCormick, P. Liu, Y.-W. Zhang, F. G. Omenetto, Y. Huang, T. Coleman, J. A. Rogers, *Science (80-.).* **2011**, *333*, 838.

[60] S. Wang, J. Xu, W. Wang, G.-J. N. Wang, R. Rastak, F. Molina-Lopez, J. W. Chung, S. Niu, V. R. Feig, J. Lopez, T. Lei, S.-K. Kwon, Y. Kim, A. M. Foudeh, A. Ehrlich, A. Gasperini, Y. Yun, B. Murmann, J. B.-H. Tok, Z. Bao, *Nature* **2018**, *555*, 83.

[61] D. Kong, R. Pfattner, A. Chortos, C. Lu, A. C. Hinckley, C. Wang, W.-Y. Lee, J. W. Chung, Z. Bao, *Adv. Funct. Mater.* **2016**, *26*, 4680.

[62] C. Wang, W.-Y. Lee, D. Kong, R. Pfattner, G. Schweicher, R. Nakajima, C. Lu, J. Mei, T. H. Lee, H.-C. Wu, J. Lopez, Y. Diao, X. Gu, S. Himmelberger, W. Niu, J. R. Matthews, M. He, A. Salleo, Y. Nishi, Z. Bao, *Sci. Rep.* **2015**, *5*, 17849.

[63] K.-Y. Chun, Y. Oh, J. Rho, J.-H. Ahn, Y.-J. Kim, H. R. Choi, S. Baik, *Nat. Nanotechnol.* **2010**, *5*, 853.

[64] B. O'Connor, E. P. Chan, C. Chan, B. R. Conrad, L. J. Richter, R. J. Kline, M. Heeney, I. McCulloch, C. L. Soles, D. M. DeLongchamp, *ACS Nano* **2010**, *4*, 7538.

[65] Y. Zheng, G. N. Wang, J. Kang, M. Nikolka, H. Wu, H. Tran, S. Zhang, H. Yan, H. Chen, P. Y. Yuen, J. Mun, R. H. Dauskardt, I. McCulloch, J. B. -H. Tok, X. Gu, Z. Bao, *Adv. Funct. Mater.* **2019**, *1905340*, 1905340.

[66] Y. Li, W. K. Tatum, J. W. Onorato, Y. Zhang, C. K. Luscombe, *Macromolecules* **2018**, *51*, 6352.

[67] J. Y. Oh, S. Rondeau-Gagné, Y. C. Chiu, A. Chortos, F. Lissel, G. J. N. Wang, B. C. Schroeder, T. Kurosawa, J. Lopez, T. Katsumata, J. Xu, C. Zhu, X. Gu, W. G. Bae, Y. Kim, L. Jin, J. W. Chung, J. B. H. Tok, Z. Bao, *Nature* **2016**, *539*, 411.

[68] J. A. Rogers, T. Someya, Y. Huang, *Science (80-.).* **2010**, *327*, 1603.

[69] S. Wang, J. Y. Oh, J. Xu, H. Tran, Z. Bao, *Acc. Chem. Res.* **2018**, *51*, 1033.

[70] R. Xie, R. H. Colby, E. D. Gomez, *Adv. Electron. Mater.* **2018**, *4*, 1700356.

[71] M. R. VanLandingham, J. S. Villarrubia, W. F. Guthrie, G. F. Meyers, *Macromol. Symp.* **2001**, *167*, 15.

[72] D. Rodriquez, J.-H. Kim, S. E. Root, Z. Fei, P. Boufflet, M. Heeney, T.-S. Kim, D. J. Lipomi, *ACS Appl. Mater. Interfaces* **2017**, *9*, 8855.

[73] R. Xie, Y. Lee, M. P. Aplan, N. J. Caggiano, C. Müller, R. H. Colby, E. D. Gomez, *Macromolecules* **2017**, *50*, 5146.

[74] P. E. Hopkinson, P. A. Staniec, A. J. Pearson, A. D. F. Dunbar, T. Wang, A. J. Ryan, R. A. L. Jones, D. G. Lidzey, A. M. Donald, *Macromolecules* **2011**, *44*, 2908.

[75] A. Onwubiko, W. Yue, C. Jellett, M. Xiao, H.-Y. Chen, M. K. Ravva, D. A. Hanifi, A.-C. Knall, B. Purushothaman, M. Nikolka, J.-C. Flores, A. Salleo, J.-L. Bredas, H. Sirringhaus, P. Hayoz, I. McCulloch, *Nat. Commun.* **2018**, *9*, 416.

[76] I. N. Hulea, S. Fratini, H. Xie, C. L. Mulder, N. N. Iossad, G. Rastelli, S. Ciuchi, A. F. Morpurgo, *Nat. Mater.* **2006**, *5*, 982.

[77] H. Bronstein, C. B. Nielsen, B. C. Schroeder, I. McCulloch, *Nat. Rev. Chem.* **2020**, *4*, 66.

[78] K. Wijeratne, *Conducting Polymer Electrodes for Thermogalvanic Cells*, Linköping University Electronic Press, Linköping, **2018**.

[79] M. S. Vezie, S. Few, I. Meager, G. Pieridou, B. Dörling, R. S. Ashraf, A. R. Goñi, H. Bronstein, I. McCulloch, S. C. Hayes, M. Campoy-Quiles, J. Nelson, *Nat. Mater.* **2016**, *15*, 746.

[80] G. Giri, E. Verploegen, S. C. B. Mannsfeld, S. Atahan-Evrenk, D. H. Kim, S. Y. Lee, H. A. Becerril, A. Aspuru-Guzik, M. F. Toney, Z. Bao, *Nature* **2011**, *480*, 504.

[81] J. Zaumseil, *Adv. Electron. Mater.* **2019**, *5*, 1.

[82] M. Knupfer, *Appl. Phys. A Mater. Sci. Process.* **2003**, *77*, 623.

[83] V. Bulovic, *6.973 Org. Optoelectron. Spring 2003. (MIT OpenCourseWare Massachusetts Inst. Technol.* **2003**, *5321*, 1.

[84] J.-L. Brédas, J. Cornil, A. J. Heeger, *Adv. Mater.* **1996**, *8*, 447.

[85] S. Alvarado, P. Seidler, D. Lidzey, D. Bradley, *Phys. Rev. Lett.* **1998**, *81*, 1082.

[86] V. I. Arkhipov, H. Bässler, *Phys. status solidi* **2004**, *201*, 1152.

[87] C. E. Swenberg, M. Pope, *Electronic Processes in Organic Crystals and Polymers*, Oxford University Press New York, **1999**.

[88] G. N. Lewis, M. Kasha, *J. Am. Chem. Soc.* **1944**, *66*, 2100.

[89] S. Guha, J. D. Rice, Y. T. Yau, C. M. Martin, M. Chandrasekhar, H. R. Chandrasekhar, R. Guentner, P. Scanduicci de Freitas, U. Scherf, *Phys. Rev. B* **2003**, *67*, 125204.

[90] A. L. T. Khan, P. Sreearunothai, L. M. Herz, M. J. Banach, A. Köhler, *Phys. Rev. B* **2004**, *69*, 085201.

[91] A. Nano, **2015**.

[92] M. C. J. M. Vissenberg, M. Matters, *Phys. Rev. B* **1998**, *57*, 12964.

[93] C. Liu, K. Huang, W.-T. Park, M. Li, T. Yang, X. Liu, L. Liang, T. Minari, Y.-Y. Noh, *Mater. Horizons* **2017**, *4*, 608.

[94] A. Miller, E. Abrahams, *Phys. Rev.* **1960**, *120*, 745.

[95] D. Yu, C. Wang, B. L. Wehrenberg, P. Guyot-Sionnest, *Phys. Rev. Lett.* **2004**, *92*, 216802.

[96] S. Wang, M. Ha, M. Manno, C. Daniel Frisbie, C. Leighton, *Nat. Commun.* **2012**, *3*, 1210.

[97] R. P. Fornari, A. Troisi, *Phys. Chem. Chem. Phys.* **2014**, *16*, 9997.

[98] S. Schott, U. Chopra, V. Lemaur, A. Melnyk, Y. Olivier, R. Di Pietro, I. Romanov, R. L. Carey, X. Jiao, C. Jellett, M. Little, A. Marks, C. R. McNeill, I. McCulloch, E. R. McNellis, D. Andrienko, D. Beljonne, J. Sinova, H. Sirringhaus, *Nat. Phys.* **2019**, *15*, 814.

[99] G. A. H. Wetzelaer, L. J. A. Koster, P. W. M. Blom, *Phys. Rev. Lett.* **2011**, *107*, 1.

[100] G. Horowitz, R. Hajlaoui, P. Delannoy, *J. Phys. III* **1995**, *5*, 355.

[101] A. Luzio, F. Nübling, J. Martin, D. Fazzi, P. Selter, E. Gann, C. R. McNeill, M. Brinkmann, M. R. Hansen, N. Stingelin, M. Sommer, M. Caironi, *Nat. Commun.* **2019**, *10*, 3365.

[102] R. Di Pietro, I. Nasrallah, J. Carpenter, E. Gann, L. S. Kölln, L. Thomsen, D. Venkateshvaran, K. O'Hara, A. Sadhanala, M. Chabinyc, C. R. McNeill, A. Facchetti, H. Ade, H. Sirringhaus, D. Neher, *Adv. Funct. Mater.* **2016**, *26*, 8011.

[103] T. J. Richards, H. Sirringhaus, *J. Appl. Phys.* **2007**, *102*, 094510.

[104] T. Uemura, C. Rolin, T. H. Ke, P. Fesenko, J. Genoe, P. Heremans, J. Takeya, *Adv. Mater.* **2016**, *28*, 151.

[105] E. G. Bittle, J. I. Basham, T. N. Jackson, O. D. Jurchescu, D. J. Gundlach, *Nat. Commun.* **2016**, *7*, 10908.

[106] I. McCulloch, A. Salleo, M. Chabinyc, *Science (80-.).* **2016**, *352*, 1521.

[107] J. Smith, R. Hamilton, I. McCulloch, N. Stingelin-Stutzmann, M. Heeney, D. D. C. Bradley, T. D. Anthopoulos, *J. Mater. Chem.* **2010**, *20*, 2562.

[108] *Proc. R. Soc. London. Ser. A. Math. Phys. Sci.* **1939**, *171*, 27.

[109] J. Zaumseil, R. H. Friend, H. Sirringhaus, *Nat. Mater.* **2006**, *5*, 69.

[110] J. Zaumseil, H. Sirringhaus, *Chem. Rev.* **2007**, *107*, 1296.

[111] S. Jung, C.-H. Kim, Y. Bonnassieux, G. Horowitz, *J. Phys. D. Appl. Phys.* **2015**, *48*, 395103.

[112] J. J. Brondijk, W. S. C. Roelofs, S. G. J. Mathijssen, A. Shehu, T. Cramer, F. Biscarini, P. W. M. Blom, D. M. De Leeuw, *Phys. Rev. Lett.* **2012**, *109*, 1.

[113] C. Tanase, E. J. Meijer, P. W. M. Blom, D. M. de Leeuw, *Phys. Rev. Lett.* **2003**, *91*, 216601.

[114] Y. Jung, R. Joseph Kline, D. A. Fischer, R. J. Kline, M. Heeney, L. McCulloch, D. M. DeLongchamp, *Adv. Funct. Mater.* **2008**, *18*, 742.

[115] H. Sirringhaus, *Adv. Mater.* **2005**, *17*, 2411.

[116] S. D. Ogier, J. Veres, D. C. Cupertino, S. Mohialdin Khaffaf, S. W. Leeming, *Adv. Funct. Mater.* **2003**, *13*, 199.

[117] L.-L. Chua, J. Zaumseil, J.-F. Chang, E. C.-W. Ou, P. K.-H. Ho, H. Sirringhaus, R. H. Friend, *Nature* **2005**, *434*, 194.

[118] S. Torabi, F. Jahani, I. Van Severen, C. Kanimozhi, S. Patil, R. W. A. Havenith, R. C. Chiechi, L. Lutsen, D. J. M. Vanderzande, T. J. Cleij, J. C. Hummelen, L. J. A. Koster, *Adv. Funct. Mater.* **2015**, *25*, 150.

[119] T. Richards, M. Bird, H. Sirringhaus, *J. Chem. Phys.* **2008**, *128*, 234905.

[120] H. Hasegawa, *J. Vac. Sci. Technol. B Microelectron. Nanom. Struct.* **1986**, *4*, 1130.

[121] M. Y. Doghish, F. D. Ho, *IEEE Trans. Electron Devices* **1992**, *39*, 2771.

[122] M. A. Green, *J. Appl. Phys.* **1990**, *67*, 2944.

[123] W. Xie, C. D. Frisbie, *MRS Bull.* **2013**, *38*, 43.

[124] H. H. Choi, K. Cho, C. D. Frisbie, H. Sirringhaus, V. Podzorov, *Nat. Mater.* **2017**, *17*, 2.

[125] L. Herlogsson, Electrolyte-Gated Organic Thin-Film Transistors, **2011**.

[126] M. Weis, *J. Appl. Phys.* **2012**, *111*, 054506.

[127] C. Liu, Y. Xu, Y.-Y. Noh, *Mater. Today* **2015**, *18*, 79.

[128] J. B. Casady, R. W. Johnson, *Solid. State. Electron.* **1996**, *39*, 1409.

[129] P. G. Neudeck, R. S. Okojie, Liang-Yu Chen, *Proc. IEEE* **2002**, *90*, 1065.

[130] M. Nikolka, M. Hurhangee, A. Sadhanala, H. Chen, I. McCulloch, H. Sirringhaus, *Adv. Electron. Mater.* **2018**, *4*, 1700410.

[131] Y. Zhao, X. Zhao, M. Roders, A. Gumyusenge, A. L. Ayzner, J. Mei, *Adv. Mater.* **2017**, *29*, 1605056.

[132] J. Chen, C. K. Tee, J. Yang, C. Shaw, M. Shtein, J. Anthony, D. C. Martin, *J. Polym. Sci. Part B Polym. Phys.* **2006**, *44*, 3631.

[133] A. Gumyusenge, D. T. Tran, X. Luo, G. M. Pitch, Y. Zhao, K. A. Jenkins, T. J. Dunn, A. L. Ayzner, B. M. Savoie, J. Mei, *Science (80-.).* **2018**, *362*, 1131.

[134] C. R. Snyder, D. M. DeLongchamp, *Curr. Opin. Solid State Mater. Sci.* **2018**, *22*, 41.

[135] C. Müller, *Chem. Mater.* **2015**, *27*, 2740.

[136] G. Strobl, *The Physics of Polymers, Third Revised and Expanded Edition*, Springer-Verlag, Berlin Heidelberg, **2007**.

[137] J. Heijboer, *Int. J. Polym. Mater.* **1977**, *6*, 11.

[138] B. Schartel, J. H. Wendorff, *Polymer (Guildf).* **1995**, *36*, 899.

[139] D. Leman, M. A. Kelly, S. Ness, S. Engmann, A. Herzing, C. Snyder, H. W. Ro, R. J. Kline, D. M. DeLongchamp, L. J. Richter, *Macromolecules* **2015**, *48*, 383.

[140] S. Savagatrup, A. D. Printz, T. F. O'Connor, A. V. Zaretski, D. Rodriquez, E. J. Sawyer, K. M. Rajan, R. I. Acosta, S. E. Root, D. J. Lipomi, *Energy Environ. Sci.* **2015**, *8*, 55.

[141] W. R. Mateker, M. D. McGehee, *Adv. Mater.* **2017**, *29*, 1603940.

[142] B. McCulloch, V. Ho, M. Hoarfrost, C. Stanley, C. Do, W. T. Heller, R. A. Segalman, *Macromolecules* **2013**, *46*, 1899.

[143] C. Müller, M. Esmaeili, C. Riekel, D. W. Breiby, O. Inganäs, *Polymer (Guildf).* **2013**, *54*, 805.

[144] R. Kroon, *Synthesis & Properties of Pi-Conjugated Polymers for OPV*, **2013**.

[145] T. Wang, A. J. Pearson, A. D. F. Dunbar, P. A. Staniec, D. C. Watters, H. Yi, A. J. Ryan, R. A. L. Jones, A. Iraqi, D. G. Lidzey, *Adv. Funct. Mater.* **2012**, *22*, 1399.

[146] S. M. Aharoni, *Polym. Adv. Technol.* **1998**, *9*, 169.

[147] P. G. Royall, C. Y. Huang, S. W. J. Tang, J. Duncan, G. Van-De-Velde, M. B. Brown, *Int. J. Pharm.* **2005**, *301*, 181.

[148] R. Ou, Y. Xie, Q. Wang, S. Sui, M. P. Wolcott, *Holzforschung* **2015**, *69*, 223.

[149] A. K. Sircar, M. L. Galaska, S. Rodrigues, R. P. Chartoff, *Rubber Chem. Technol.* **1999**, *72*, 513.

[150] D. S. Jones, Y. Tian, O. Abu-Diak, G. P. Andrews, *Adv. Drug Deliv. Rev.* **2012**, *64*, 440.

[151] M. Statz, D. Venkateshvaran, X. Jiao, S. Schott, C. R. McNeill, D. Emin, H. Sirringhaus, R. Di Pietro, *Commun. Phys.* **2018**, *1*, 16.

[152] H. Chen, M. Hurhangee, M. Nikolka, W. Zhang, M. Kirkus, M. Neophytou, S. J. Cryer, D. Harkin, P. Hayoz, M. Abdi-Jalebi, C. R. McNeill, H. Sirringhaus, I. McCulloch, *Adv. Mater.* **2017**, *29*, 1702523.

[153] M. Gruber, S. H. Jung, S. Schott, D. Venkateshvaran, A. J. Kronemeijer, J. W. Andreasen, C. R. McNeill, W. W. H. Wong, M. Shahid, M. Heeney, J. K. Lee, H. Sirringhaus, *Chem. Sci.* **2015**, *6*, 6949.

[154] Z. Wang, Z. Liu, L. Ning, M. Xiao, Y. Yi, Z. Cai, A. Sadhanala, G. Zhang, W. Chen, H. Sirringhaus, D. Zhang, *Chem. Mater.* **2018**, *30*, 3090.

[155] I. Kang, H.-J. Yun, D. S. Chung, S.-K. Kwon, Y.-H. Kim, *J. Am. Chem. Soc.* **2013**, *135*, 14896.

[156] J. Mei, D. H. Kim, A. L. Ayzner, M. F. Toney, Z. Bao, *J. Am. Chem. Soc.* **2011**, *133*, 20130.

[157] Z. Liu, G. Zhang, D. Zhang, *Acc. Chem. Res.* **2018**, *51*, 1422.

[158] T. Lei, J.-H. Dou, J. Pei, *Adv. Mater.* **2012**, *24*, 6457.

[159] J. Mei, Z. Bao, *Chem. Mater.* **2014**, *26*, 604.

[160] B. Fu, J. Baltazar, A. R. Sankar, P.-H. Chu, S. Zhang, D. M. Collard, E. Reichmanis, *Adv. Funct. Mater.* **2014**, *24*, 3734.

[161] F. Urbach, *Phys. Rev.* **1953**, *92*, 1324.

[162] S. P. Senanayak, B. Yang, T. H. Thomas, N. Giesbrecht, W. Huang, E. Gann, B. Nair, K. Goedel, S. Guha, X. Moya, C. R. McNeill, P. Docampo, A. Sadhanala, R. H. Friend, H. Sirringhaus, *Sci. Adv.* **2017**, *3*, e1601935.

[163] A. J. Kronemeijer, V. Pecunia, D. Venkateshvaran, M. Nikolka, A. Sadhanala, J. Moriarty, M. Szumilo, H. Sirringhaus, *Adv. Mater.* **2014**, *26*, 728.

[164] N. Sharma, K. Prabakar, S. Ilango, S. Dash, A. K. Tyagi, *Adv. Mater. Proc.* **2017**, *2*, 342.

[165] S. De Wolf, J. Holovsky, S.-J. Moon, P. Löper, B. Niesen, M. Ledinsky, F.-J. Haug, J.-H. Yum, C. Ballif, *J. Phys. Chem. Lett.* **2014**, *5*, 1035.

[166] J. C. de Mello, H. F. Wittmann, R. H. Friend, *Adv. Mater.* **1997**, *9*, 230.

[167] E. Coutino-Gonzalez, M. B. J. Roeffaers, B. Dieu, G. De Cremer, S. Leyre, P. Hanselaer, W. Fyen, B. Sels, J. Hofkens, *J. Phys. Chem. C* **2013**, *117*, 6998.

[168] J. Epp, in *Mater. Charact. Using Nondestruct. Eval. Methods*, Elsevier, **2016**, pp. 81–124.

[169] R. K. Heenan, S. E. Rogers, D. Turner, A. E. Terry, J. Treadgold, S. M. King, *Neutron News* **2011**, *22*, 19.

[170] D. Nečas, P. Klapetek, *Open Phys.* **2012**, *10*, DOI 10.2478/s11534-011-0096-2.

[171] D. A. Warr, L. M. A. A. Perdigão, H. Pinfold, J. Blohm, D. Stringer, A. Leventis, H. Bronstein, A. Troisi, G. Costantini, *Sci. Adv.* **1800**, *4*, 1.

[172] S. Vleeshouwers, A. M. Jamieson, R. Simha, *Polym. Eng. Sci.* **1989**, *29*, 662.

[173] D. S. Jones, **1999**, *179*, 167.

[174] W. Zhang, E. D. Gomez, S. T. Milner, *Macromolecules* **2014**, *47*, 6453.

[175] B. Kuei, E. D. Gomez, *Soft Matter* **2017**, *13*, 49.

[176] R. Noriega, A. Salleo, A. J. Spakowitz, *Proc. Natl. Acad. Sci.* **2013**, *110*, 16315.

[177] C. L. Gettinger, A. J. Heeger, J. M. Drake, D. J. Pine, *J. Chem. Phys.* **1994**, *101*, 1673.

[178] G. Rossi, R. R. Chance, R. Silbey, *J. Chem. Phys.* **1989**, *90*, 7594.

[179] V. Coropceanu, J. Cornil, D. A. da Silva Filho, Y. Olivier, R. Silbey, J.-L. Brédas, *Chem. Rev.* **2007**, *107*, 926.

[180] J. Zaumseil, *Adv. Electron. Mater.* **2019**, *5*, 1800514.

[181] M. Kim, S. U. Ryu, S. A. Park, K. Choi, T. Kim, D. Chung, T. Park, *Adv. Funct. Mater.* **2020**, *30*, 1904545.

[182] A. F. Paterson, S. Singh, K. J. Fallon, T. Hodsden, Y. Han, B. C. Schroeder, H. Bronstein, M. Heeney, I. McCulloch, T. D. Anthopoulos, *Adv. Mater.* **2018**, *30*, 1801079.

[183] S. Fratini, M. Nikolka, A. Salleo, G. Schweicher, H. Sirringhaus, *Nat. Mater.* **2020**, *19*, 491.

[184] G. Fournet, *Bull. Soc. Fr. Min. Cris.* **1951**, *74*, 39.

[185] J. S. Pedersen, *Adv. Colloid Interface Sci.* **1997**, *70*, 171.

[186] T. A. Halgren, *J. Comput. Chem.* **1996**, *17*, 490.

[187] T. A. Halgren, *J. Comput. Chem.* **1996**, *17*, 520.

[188] T. A. Halgren, *J. Comput. Chem.* **1996**, *17*, 553.

[189] T. A. Halgren, R. B. Nachbar, *J. Comput. Chem.* **1996**, *17*, 587.

[190] T. A. Halgren, *J. Comput. Chem.* **1996**, *17*, 616.

[191] M. C. Gwinner, Y. Vaynzof, K. K. Banger, P. K. H. Ho, R. H. Friend, H. Sirringhaus, *Adv. Funct. Mater.* **2010**, *20*, 3457.

[192] H. N. Tsao, D. M. Cho, I. Park, M. R. Hansen, A. Mavrinskiy, D. Y. Yoon, R. Graf, W. Pisula, H. W. Spiess, K. Müllen, *J. Am. Chem. Soc.* **2011**, *133*, 2605.

[193] M. J. Lee, D. Gupta, N. Zhao, M. Heeney, I. Mcculloch, H. Sirringhaus, *Adv. Funct. Mater.* **2011**, *21*, 932.

[194] Y. Diao, B. C.-K. Tee, G. Giri, J. Xu, D. H. Kim, H. A. Becerril, R. M. Stoltenberg, T. H. Lee, G. Xue, S. C. B. Mannsfeld, Z. Bao, *Nat. Mater.* **2013**, *12*, 665.

[195] A. K. K. Kyaw, L. S. Lay, G. W. Peng, J. Changyun, Z. Jie, *Chem. Commun.* **2016**, *52*, 358.

[196] H. N. Tsao, D. Cho, J. W. Andreasen, A. Rouhanipour, D. W. Breiby, W. Pisula, K. Müllen, *Adv. Mater.* **2009**, *21*, 209.

[197] D. Khim, A. Luzio, G. E. Bonacchini, G. Pace, M. J. Lee, Y. Y. Noh, M. Caironi, *Adv. Mater.* **2018**, *30*, 1.

[198] A. B. Kaiser, *Reports Prog. Phys.* **2000**, *64*, 1.

[199] W. A. De Heer, *Science (80-.).* **1995**, *268*, 845.

[200] T. P. Hiemenz, Paul C and Lodge, *Polymer Chemistry*, CRC Press, **2007**.

[201] J. Li, Y. Zhao, H. S. Tan, Y. Guo, C. A. Di, G. Yu, Y. Liu, M. Lin, S. H. Lim, Y. Zhou, H. Su, B. S. Ong, *Sci. Rep.* **2012**, *2*, 1.

[202] Y. Liu, J. Zhao, Z. Li, C. Mu, W. Ma, H. Hu, K. Jiang, H. Lin, H. Ade, H. Yan, *Nat. Commun.* **2014**, *5*, 5293.

[203] P. J. Flory, M. Volkenstein, *Biopolymers* **1969**, *8*, 699.

[204] R. Joseph Kline, M. D. McGehee, M. F. Toney, *Nat. Mater.* **2006**, *5*, 222.

[205] S. Schott, E. Gann, L. Thomsen, S. H. Jung, J. K. Lee, C. R. McNeill, H. Sirringhaus, *Adv. Mater.* **2015**, *27*, 7356.

[206] A. Wadsworth, H. Chen, K. J. Thorley, C. Cendra, M. Nikolka, H. Bristow, M. Moser, A. Salleo, T. D. Anthopoulos, H. Sirringhaus, I. McCulloch, *J. Am. Chem. Soc.* **2020**, *142*, 652.

[207] S. E. Root, M. A. Alkhadra, D. Rodriquez, A. D. Printz, D. J. Lipomi, *Chem. Mater.* **2017**, *29*, 2646.

[208] T. H. Thomas, D. J. Harkin, A. J. Gillett, V. Lemaur, M. Nikolka, A. Sadhanala, J. M. Richter, J. Armitage, H. Chen, I. McCulloch, S. M. Menke, Y. Olivier, D. Beljonne, H. Sirringhaus, *Nat. Commun.* **2019**, *10*, 2614.

[209] A. Troisi, *Org. Electron.* **2011**, *12*, 1988.

[210] R. A. Talja, Y. H. Roos, *Thermochim. Acta* **2001**, *380*, 109.

[211] J. Xiao, Z. Chen, G. Zhang, Q.-Y. Li, Q. Yin, X.-F. Jiang, F. Huang, Y.-X. Xu, H.-L. Yip, Y. Cao, *J. Mater. Chem. C* **2018**, *6*, 4457.